Long-Term Timing of Millisecond Pulsars

Eric Michael Splaver

A Dissertation

Presented to the Faculty

of Princeton University

in Candidacy for the Degree

of Doctor of Philosophy

Recommended for Acceptance

by the Department of

Physics

November 2004

Abstract

We report on four years of data from an ongoing program of timing millisecond pulsars (MSPs) at the Arecibo radio observatory. In our monthly observations we studied six MSPs, all but one of them binary. Our work had two thrusts. First, we made high-precision measurements of the rotational, astrometric, and (where applicable) orbital parameters of the objects. Of particular interest in binary systems were relativistic post-Keplerian phenomena such as Shapiro delay and periastron advance. These terms yielded information about the system masses when interpreted within general relativity. The masses, in turn, can be used to constrain theories of stellar evolution. Additionally, the measured decay of the binary period in one MSP put limits on violations of the Strong Equivalence Principle. The other focus of our work was on identifying long-term stochastic signals in the timing data. These pointed to interesting physics in the interstellar medium (ISM) or in the pulsar itself that lie outside the equations of motion of our timing model. Along these lines, we measured fluctuations in the content of free electrons in the direction of one of the MSPs. With these, we described the power spectrum of spatial variations in the ISM. Elsewhere, we found timing noise in one MSP that hitherto had been considered one of the most precise celestial clocks.

ii

Contents

List of Figures

List of Tables

Acknowledgements

Primary thanks go to my advisor, David Nice, for launching me on the long-term timing project, for securing the NSF money that funded it, for adding new features on request to the `TEMPO` program, for answering thousands of questions, and for absolutely everything else connected with this work. Thanks to Ingrid Stairs for maintaining the Mark IV hardware and software that I used to collect data. Thanks to my other main collaborators, Andrea Lommen and Don Backer, for input and for sharing the monthly observations. Thanks to physicists who have provided useful discussions, including Fernando Camilo, Joe Taylor, Rick Jenet, Walter Brisken, Steve Thorsett, and Michael Nolta. Thanks to two past staff scientists at Arecibo who helped me use the telescope, Duncan Lorimer and Xiriaki Xilouris. Thanks to Jim Cordes, Michael Kramer, and Oliver Loehmer for sharing data on PSR J0751+1807. Thanks to all other radio astronomers who obtained the early data used in this work. Thanks to the Arecibo telescope operators for making it possible to run the telescope and process data remotely. Outside of physics, thanks to my parents, Howard and Florence Splaver, for helping me to attend graduate school. Thanks to my wife, Alison Mazer, for her everlasting patience. This thesis, and everything that follows it, is dedicated to her.

Chapter 1

A Pulsar Timing Primer

1.1   The Usefulness of a Clock in Space

When you point a radio telescope at a pulsar, the pulses you receive are quite regular.
They are almost like the ticks of a clock. But they are not absolutely steady. Close
examination reveals slight variations in the intervals between pulses. The spacing
increases at some times and decreases at others. Pulsar timing, the subject of this
thesis, is the practice of analyzing these changes. The practitioner assumes that a
pulsar is indeed a perfect clock in space. The non-uniformity of its ticks is attributed
to the pulsar's motion relative to Earth. Modeling the variations mathematically
allows the motion to be mapped out with great precision.

How is this accomplished? An ambulance illustrates the basic idea. As is well
known, if you are standing outside an ambulance, the pitch of the siren falls as the
vehicle passes. This is the famous Doppler effect. From the drop in frequency, the
speed of the ambulance can be deduced: the bigger the shift in pitch, the faster the
ambulance is moving. You can begin to understand pulsar timing by recognizing that
the siren is like a pulsar. Its vibrating tone is effectively a series of clock ticks. Your
ear, meanwhile, is like the radio telescope. From the change in the intervals between

the ticks, it is possible to measure the speed of the pulsar as it travels through space.

Of course, this simple analogy does not do justice to the extraordinary subtlety of pulsar timing, which can find out much more about a pulsar than its speed. Nor does the analogy illustrate the conceptual challenges faced in pulsar timing. What if the interstellar medium through which the pulses travel can by itself alter the intervals between them? What if the pulsar orbits another star instead of moving along a straight line? To really glimpse the power of pulsar timing, imagine that the ambulance is doing circles in the hospital parking lot. You are listening to it in your own car while accelerating along a curved highway, but it is difficult to hear because your CD player is turned up and it is raining outside. If I now inform you that from the barely audible siren sound you can tell how much the ambulance weighs, you should begin to appreciate why pulsar timing is such a fruitful branch of astrophysics.

1.2   What is a Pulsar?

In this thesis, pulsars will usually be treated as frequency standards without regard to what they are made of or how they radiate. Nevertheless, a basic understanding of their makeup is useful. A pulsar is, first of all, a neutron star. Such an object forms when a star with mass greater than about $8\,\mathrm{M_\odot}$ runs out of hydrogen, helium, oxygen, and other light elements to burn in its core. Its thermonuclear fire extinguished, the star can no longer offer up radiation pressure to support itself against its own weight, and it collapses. Its outer layers rush inward, their gravitational potential energy converted to kinetic energy, and they bounce off the dense center in a supernova explosion. The core that is left behind is a neutron star. Consisting primarily of degenerate neutrons in a highly magnetized superfluid ($B \sim 10^{12}\,\mathrm{G}$), its most striking feature is its compactness; a mass of roughly $1.4\,\mathrm{M_\odot}$ and a radius of about 10 km give it a density of $10^{14}\,\mathrm{g\,cm^{-3}}$, making it 10^{12} times denser than the core of the Sun.

Baade & Zwicky (1934) were the first to hypothesize such stars were an end product of stellar evolution. Their existence was not confirmed until Bell Burnell discovered the first pulsars (Hewish *et al.* 1968) and Gold (1969) identified them with neutron stars.

Besides being a neutron star, a pulsar has the property that it gives off a rotating beam of radio energy, like a lighthouse. The details of how the beam originates in the pulsar magnetosphere are disputed, but the basic picture is as follows. Having inherited angular momentum from its progenitor, the pulsar spins. Its axis of rotation is not perfectly aligned with its magnetic dipole moment (Goldreich and Julian 1969). Near the pulsar surface, the rotating magnetic field lines follow the closed loops of a dipole pattern. Beyond a certain radius, termed the "light cylinder," the field lines cannot co-rotate with the pulsar without exceeding the speed of light, and so they remain open. The relativistic electrons and positrons streaming along the field lines emit a tangential beam of coherent curvature radiation that sweeps through space as the pulsar rotates (Sturrock 1971). If the beam cuts across Earth, then we detect pulses with a period equal to the rotational period of the pulsar. The fastest known pulsar, PSR B1937+21[1], has a rotational period of 1.5 ms. The slowest, PSR J2144-3933, has a period of 8.5 s.

---

[1]A pulsar's name gives its celestial coordinates. The number in front of the '+' or '-' is the right ascension in hours and minutes, and the number behind it is the declination in degrees. The letter 'B' or 'J' tells whether the coordinates are based in the B1950.0 or the J2000.0 system. So, for example, the object PSR J1830$-$1135 mentioned above has, in the J2000.0 system, a right ascension of $\alpha = 18^{\mathrm{h}}30^{\mathrm{m}}$ and a declination of $\delta = -11°35'$. Whether a pulsar has a 'B' or a 'J' designation is a function of how recently it was discovered; by IAU (1976) convention, all objects named after 1 January 1984 use the J2000.0 coordinate system. For reasons of uniqueness or history, a few pulsars also go by nicknames, such as the Crab pulsar (PSR B0531+21), situated in the Crab nebula, or the Hulse-Taylor pulsar (PSR B1913+16), the first known binary pulsar, discovered by R. A. Hulse and J. H. Taylor (Hulse and Taylor 1975).

Although we treat pulsars as timepieces, they differ from clocks in a key respect: the interval between their pulses is always increasing. This is because the pulsar is giving up rotational kinetic energy in the form of radiation. Most of the energy escapes through magnetic dipole radiation emitted at the spin frequency (on the order of Hz or kHz) and absorbed by the interstellar medium (ISM). Only a small fraction of energy is lost through the observed radio beam. Additional energy also leaks out through particle radiation and gravitational radiation. A clock that loses time is normally considered defective. In fact, it is still a perfectly adequate timekeeper provided that it slows down at a predictable rate. If so, telling time is just a matter of keeping track of seconds lost or gained. Likewise, the rotational deceleration of a pulsar does not prevent it from standing in as a clock in space so long as the slowdown is smooth enough for it to be modeled accurately. This is not the case for the entire pulsar population, but it is generally true for an important subclass known as the millisecond pulsars (MSPs), which are the focus of this work.

1.3   Regular vs. Millisecond Pulsars

Figure 1.1 plots spin period, P, versus its rate of increase, $\dot{P}$, for 1183 pulsars. The clustering of points into two separate regions illustrates the difference between regular and millisecond pulsars. Constituting the majority, the regular pulsars fall into the upper right corner with $10\,\mathrm{ms} \lesssim P \lesssim 10\,\mathrm{s}$ and $10^{-17}\,\mathrm{s\,s^{-1}} \lesssim \dot{P} \lesssim 10^{-11}\,\mathrm{s\,s^{-1}}$. In the lower corner are the MSPs—so called because of their small spin periods—with $1\,\mathrm{ms} \lesssim P \lesssim 10\,\mathrm{ms}$ and $10^{-21}\,\mathrm{s\,s^{-1}} \lesssim \dot{P} \lesssim 10^{-18}\,\mathrm{s\,s^{-1}}$.

The spin characteristics of the two classes of pulsars can be traced to their different evolutions. The regular pulsars are recently formed. Because of their high magnetic fields ($10^{12}\,\mathrm{G}$), their periods decay rapidly at rates of a few tenths of a microsecond per year. After about 10 million years, a young pulsar's rotation will slow to the point
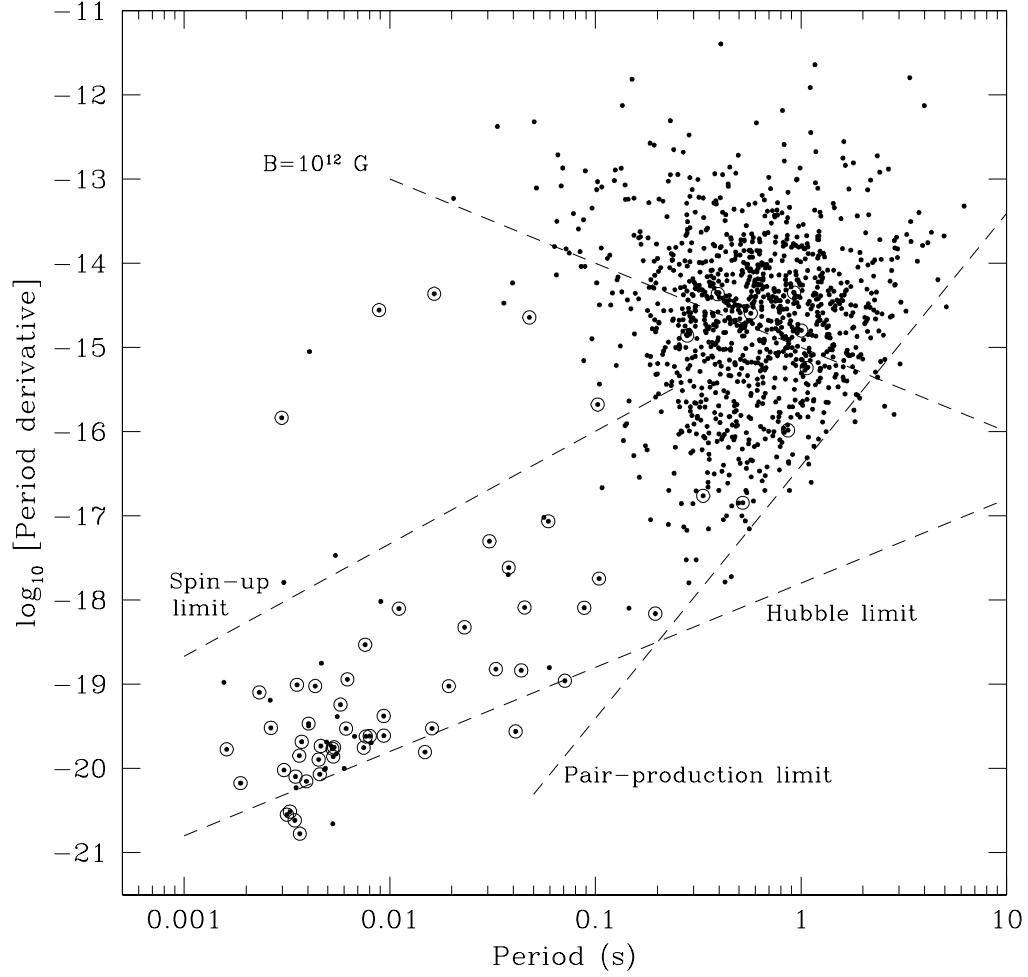
Figure 1.1: P-$\dot{P}$ diagram for 1183 pulsars. Small dots stand for isolated pulsars. Circles are binary pulsars. The spin-up limit corresponds to the maximum possible rate of accretion in a binary system. The Hubble limit gives an implied pulsar age equal to the measured age of the universe, $13.7 \pm 0.2\,\mathrm{Gyr}$ (Spergel *et al.* 2003). The pair-production limit shows the spin rate below which the rotating electromagnetic fields in the pulsar magnetosphere cease to produce enough electron-positron pairs for the star to emit a radio beam. The magnetic field represents a surface dipole magnetic field strength of $B = 10^{12}\,\mathrm{G}$.

where the electromagnetic fields in its magnetosphere are no longer strong enough to create electrons and positrons, a state shown in Figure 1.1 as the pair-production limit. Without a supply of charged particles to stream along the magnetic field lines, the pulsar will cease to emit a radio beam, and it will remain defunct unless some external torque speeds up its rotation.

Millisecond pulsars are formerly inactive pulsars that have undergone just such an angular acceleration. Also known as recycled pulsars, MSPs are thought to have been spun from low to high rates of rotation, and hence back to radio luminosity, through accretion of matter and angular momentum from a companion star that overflowed its Roche lobe in the course of its evolution (Phinney and Kulkarni 1994). During the spin-up phase, the systems are believed to be X-ray binaries (Alpar *et al.* 1982). The formation scenario explains why most MSPs are found in binary systems, as Figure 1.1 indicates. The few isolated MSPs have evidently lost their companions. This can happen if the pulsar wind evaporates a white dwarf secondary, as is occurring in the PSR B1957+20 system (Fruchter *et al.* 1990); if a supernova explosion in the secondary disrupts the orbit; or, in a globular cluster, if gravitational interaction with a passing star ejects the secondary. MSPs are considerably older than young pulsars, with ages in the range 1-14 Gyr, as suggested by timing measurements and confirmed by the cooling ages of white dwarf companions (Schoenberner, Driebe, and Blocker 2000). The surface magnetic field strengths of MSPs are also 2-4 orders of magnitude weaker than those of regular pulsars, most likely as a result of accretion (Camilo, Thorsett, and Kulkarni 1994).

As celestial clocks, regular pulsars are inferior to MSPs. One reason is that young pulsars exhibit unpredictable rotational irregularities. The behavior can take the form of "glitches", or unpredictable drops in pulse period. The discontinuities are apparently caused by sudden changes in coupling between the pulsar crust and its superfluid

interior. The Vela pulsar, for example, undergoes glitches as large as 3.1×10^{-6} of its 89-ms period every few years (Dodson, McCulloch, and Lewis 2002). Rotational instability in young pulsars can also appear as "timing noise", or deviations over months or years from the steady spin-down behavior expected from simple electromagnetic torques. The activity is found to be correlated with period derivative, a parameter highest in young pulsars. It has been characterized as a random walk in pulse phase, period, or period derivative (Cordes and Downs 1985; Groth 1975). There is no single accepted theory for timing noise. Most authors explain it in terms of processes internal to the star including starquakes; random pinning and unpinning of superfluid vortex lines to the crust; heat pulses caused by friction between the crust and the liquid; and luminosity-related torque fluctuations (Cordes and Greenstein 1981). In comparison to young pulsars, MSPs display extremely smooth rotation. This is presumably because their interiors have had a chance to settle and because their weaker magnetic moments ensure a slow and orderly consumption of their huge stores of rotational kinetic energy.

Besides timing stability, another reason why MSPs make better clocks than regular pulsars is that their more rapidly alternating signals provide inherently better timing for a given signal strength (see eq. 3.1). As will be seen in later chapters, the combination of steady rotation and short period permits the orbits and proper motions of MSPs to be modeled with great precision. To illustrate, a decade of regular timing of an object completing 10^{10} turns per year and with arrival times measurable to within 10^{-4} of a turn yields a timing model with precision better than one part in 10^{15}. Even so, MSPs are not immune to timing imperfections. While none has been seen to glitch, low-level timing noise has been found in at least two, including PSR J1713+0747, the topic of Chapter 3, and PSR B1937+21 (Kaspi, Taylor, and Ryba 1994). The amplitude of the noise is orders of magnitude smaller than that of

young pulsars. Yet as in young pulsars it appears to obey a correlation with period derivative, suggesting that the same causes may lie behind the phenomenon in both types of stars.

1.4 Pulse Arrival Times

The business of pulsar timing consists of collecting the times at which pulses arrive at Earth and fitting them to a model of the pulsar's motion. This section summarizes techniques of acquiring a pulse time of arrival (TOA). It is instructive to display an actual TOA in the format used by pulsar astronomers:

```
3 1713+07 1410.000 51587.4760425144582 0.05
```

A pulse arrival is a relativistic event, and so location must be quoted along with time. Accordingly, the first number is code for where the data point was taken (in this case the radio observatory in Arecibo, Puerto Rico). The second column specifies the pulsar, PSR J1713+0747. The third number gives the observing frequency in the telescope frame in MHz. The fourth number is the arrival time measured with respect to the observatory's atomic clock. Quoted in modified Julian days (MJD), it is equivalent to 11h 25m 30.0732492s at Greenwich, England on 13 February 2000. The last column is the TOA uncertainty in μs.

1.4.1 Pulsar Signals Are Weak

The distances to pulsars, from tens to thousands of parsecs, make their signals extremely weak. In radio astronomy, flux density is measured in Janskys (Jy), where $1\,\mathrm{Jy} = 10^{-26}\,\mathrm{W\,m^{-2}\,Hz^{-1}}$. Pulsar flux densities range from $0.001\,\mathrm{Jy}$ to $10\,\mathrm{Jy}$. By comparison, the Princeton campus FM radio station, WPRB, broadcasts with $30\,\mathrm{kW}$ of power over a bandwidth of $0.15\,\mathrm{MHz}$. At a distance of 25 miles from the broadcast-

ing tower, it has a flux density of about 10^{15} Jy. Overcoming the faintness of pulsar signals requires long integration times on sensitive radio telescopes. Ideally, the telescopes are geographically isolated from manmade radio sources. At the focus of a telescope, the radio-frequency (RF) voltages produced by the incoming signal need to be amplified by low-noise receivers and mixed down to intermediate-frequency (IF) voltages before undergoing further processing. Signals are collected separately in two linear or circular polarizations. The orthogonal voltage streams must eventually be self- and cross-multiplied to produce detected signals.

1.4.2   Interstellar Dispersion

Another obstacle in measuring TOAs is the dispersion of the pulses as they travel through the ISM. The ISM consists mainly of neutral gas, but ionizing background radiation produces free electrons with a number density of roughly $n_e \sim 0.03\,\mathrm{cm}^{-3}$ in the Galactic spiral arms (Cordes and Lazio 2002). Electromagnetic waves propagate through this refracting plasma with a group velocity different from the speed of light,

$$v_g = c\left(1 - \frac{f_p^2}{f^2}\right)^{1/2},$$

(1.1)

where f is the wave frequency and $f_p \equiv (n_e e^2/\pi m_e)^{1/2}$ is the plasma frequency, with e and m_e the charge and mass of the electron. The frequency dependence of v_g means that if two monochromatic signals of frequencies f_1 and f_2 are emitted simultaneously by a pulsar and travel a distance d to Earth, they will arrive at separate times. Because the plasma frequency, $f_p \approx 2\,\mathrm{kHz}$, is small compared to the MHz or GHz frequencies at which radio telescopes operate, the delay between arrival times can be expanded to first order in f_p^2/f^2,

$$t_1 - t_2 = \frac{e^2}{2\pi m_e c}\left(\frac{1}{f_1^2} - \frac{1}{f_2^2}\right)\mathrm{DM},$$

(1.2)

where the column density of free electrons along the line of sight to the pulsar has been defined as the dispersion measure (DM):

$$\text{DM} \equiv \int_0^d n_e \, dz. \tag{1.3}$$

The leading factor of $e^2/2\pi m_e c$ is close to $1/2.41 \times 10^{-4}$ if DM is in $\text{pc}\,\text{cm}^{-3}$, time is in seconds, and frequency is in MHz. In our work, we follow the recommendation of Manchester & Taylor (1977) and *define* the factor to be $1/2.41000 \times 10^{-4}$. This is to forestall changes to DM values if the physical constants are updated. As a result of dispersion, different frequency components of a time-varying pulsar signal will propagate at different speeds. A pulse detected across a narrow bandwidth of Δf will smear out in time by

$$\Delta t = -\frac{e^2}{\pi m_e c} \text{DM} \frac{\Delta f}{f^3}, \tag{1.4}$$

which makes it hard to measure arrival times with accuracy. Indeed, at high DM the smearing width Δt may exceed the pulse period, making the signal impossible to detect at all unless dispersion is somehow circumvented. How is this done? From the $1/f^3$ dependence of equation 1.4 it would seem that a way around dispersion would be to observe at high frequencies. Unfortunately, pulsars have steep spectra that confine observations to low frequencies ($f \lesssim 2\,\text{GHz}$). And so dispersion must be tackled with signal-processing. Two techniques are in common use: incoherent and coherent dedispersion.

1.4.3   Incoherent Dedispersion

In incoherent dedispersion, a filterbank or a digital spectrometer divides the intermediate frequency (IF) bandpass into a large number of narrow channels. The channels are detected individually (e.g. their voltages are squared) and time-shifted relative to one another according to equation 1.2 to counteract dispersion. The method has the

advantages of being easy to implement in hardware and of accomodating the large bandpasses needed to gather strong signals. But incoherent dedispersion is less than ideal for high-precision work. Although dispersion disappears between the channels, it remains within them. Moreover, the obvious remedy of shrinking the width of channels in fact leads to a greater number of them and so compromises time resolution, which for a total bandwidth B goes as N/B, where N is the total number of channels. Because of hard-to-remove residual smearing, incoherent dedispersion has in recent years begun to be replaced by coherent dedispersion.

1.4.4   Coherent Dedispersion

Coherent dedispersion rests on the idea that the ISM acts on the pulsar signal as a filter with transfer function $H(f) = e^{-ik(f)z}$, where z is the distance to the pulsar and where

$$k(f) = \frac{2\pi}{c} f \left(1 - \frac{f_p^2}{f^2}\right)^{1/2}.$$ (1.5)

A pulsar-observing system operates at some central frequency f_0. If $f = f_0 + f_1$, where $|f_1| \leq B/2 \ll f_0$, then the wavenumber has the Taylor expansion

$$k(f_0 + f_1) = \frac{2\pi}{c}(f_0 + f_1)\left[1 - \frac{f_p^2}{2(f_0 + f_1)^2}\right].$$ (1.6)

With this, Hankins & Rickett (1975) show that the transfer function (also called the "chirp" function) can be approximated as

$$H(f_0 + f_1) = \exp\left[2\pi i \frac{e^2}{2\pi m_e c} \mathrm{DM} \frac{f_1^2}{f_0^2} \frac{1}{(f_0 + f_1)}\right].$$ (1.7)

Coherent dedispersion undoes the effect of the ISM by convolving the signal voltages with the inverse of equation 1.7. The convolution can be applied using a filter built in hardware or simulated in software. In either case, the IF signal is split into two identical parts and mixed to baseband (that is to say, a bandpass ranging from 0 to

$B/2$) by multiplying one part by $\cos 2\pi f_0 t$ and the other by $\sin 2\pi f_0 t$, creating the real and complex inputs for the filter. By the Nyquist criterion, each part must be sampled at a rate of at least B. In a key difference from incoherent dedispersion, the signal is not detected until after dedispersion is applied. Covering the entire bandpass, coherent dedispersion achieves a time resolution of $1/B$, an improvement over incoherent dedispersion.

1.4.5   Pulse Profiles

Once the pulsar signal has been dedispersed and detected, the next step in measuring a TOA is to fold the signal at the topocentric pulse period. This puts the data in the form of a pulse profile, a sampled waveform of the pulse intensity over its period. Successive individual pulses manifest a wide variety of shapes and strengths, but experience has shown that many thousands of pulses can be averaged to build a unique and consistent profile that forms a kind of fingerprint of the pulsar at a given observing frequency. Figure 1.2a shows the average total-intensity profile of PSR B1855+09 at 1410 MHz from a 190-second integration, a duration that for this pulsar (with $P = 5.6$ ms) spans almost 34,000 pulses. Pulses profiles show significant features on timescales as short as $5\,\mu$s. The high time resolution needed to capture such fine detail is achieved by integrating long enough to build up a strong signal-to-noise ratio (SNR) and by sampling the profile with a large number of bins, typically between 1024 and 4096. As the SNR obeys the usual $T^{1/2}$ scaling with integration time, extremely long integrations can be folded to produce very clean profiles. Figure 1.2b shows such a template or "standard" profile of PSR B1855+09 at 1410 MHz, constructed from several hours of observation. (For an investigation of how the precision of TOAs scales with integration time, see § 2.3.2.)
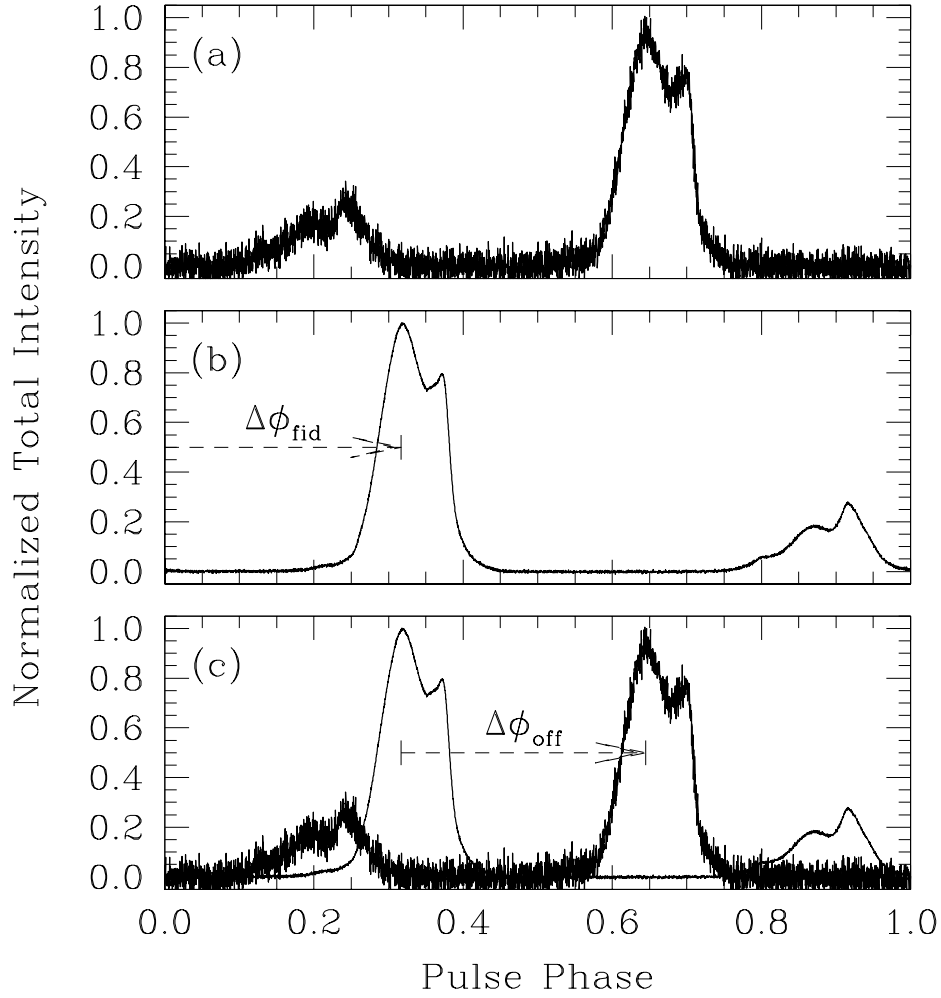
Figure 1.2: Pulse profiles of PSR B1855+09 at 1410 MHz. Panel (a) is an integrated profile from 190 s of data. Panel (b) is the low-noise standard profile of the pulsar, made from several hours of data. Also shown is the phase distance to a fiducial point in the profile, in this case the peak. Panel (c) illustrates the phase offset between the standard and integrated profiles. All three profiles contain 4096 phase bins.

1.4.6   Measuring TOAs Through Profile Comparison

The basis of measuring TOAs is a comparison of an integrated profile made from a few minutes of data with a standard profile. The procedure is as follows. The observatory clock records the instant when the first sample of the data stream is recieved. The instant is designated the start time of the integration, t_{start}. For pulsars with high spin-down rates or quick binary orbits, the observed period changes enough over a single integration that the profile made from it would blur if the period was held constant. To mitigate this problem, the start time is projected forward by Δt_{mid} to the approximate midpoint of the integration. This is done by adding to it an integer number of instantaneously correct pulse periods, a step that requires an accurate timing ephemeris acquired through prior observations. Next is added the time to some "fiducial point" in the standard profile, usually the peak. The term is $\Delta t_{\mathrm{fid}} = \Delta\phi_{\mathrm{fid}}\, P_{\mathrm{inst}}$, where the phase of the fiducial point, $\Delta\phi_{\mathrm{fid}}$, is illustrated in Figure 1.2b, and where P_{inst} is the predicted instantaneous period. (At Princeton, templates are constructed in such a way that the profile peak always falls in the first bin, guaranteeing that $\Delta\phi_{\mathrm{fid}} \equiv 0$.) Finally, the time offset between the integrated and standard profiles, $\Delta t_{\mathrm{off}} = \Delta\phi_{\mathrm{off}}\, P_{\mathrm{inst}}$, is calculated; $\Delta\phi_{\mathrm{off}}$ is shown in Figure 1.2c. A TOA is defined to be the sum

$$t = t_{\mathrm{start}} + \Delta t_{\mathrm{mid}} + \Delta t_{\mathrm{fid}} + \Delta t_{\mathrm{off}}. \tag{1.8}$$

With the goal of maximizing precision, much attention has been paid to the best way of measuring Δt_{off}. The simplest way of computing offsets—counting the whole number of bins between corresponding profile peaks—affords an uncertainty no smaller than half of a bin. More sophisticated techniques attain better precision by interpolating between bins (for a review, see Ryba 1991). The Princeton pulsar group achieves uncertainties of less than a hundredth of a bin by cross-correlating the profiles in the Fourier domain (Taylor 1992).

It is often convenient to reduce arrival times from a single observing session—an hour on the telescope typically produces nearly 20 TOAs—to a single data point. Appendix A outlines the procedure we use for averaging TOAs.

1.4.7   Clock Corrections

Millisecond pulsars can be more stable than the observatory atomic clocks that time them. To prevent drifts in the clocks from masquerading as pulsar behavior, TOAs must be referenced to a more reliable timescale. The first step is to correct them to Coordinated Universal Time (UTC). Different observatories have their own methods of making this adjustment. At Arecibo, for example, offsets between the local maser and UTC are monitored via broadcasts of the Global Positioning System (GPS) satellites. UTC is defined to stay within $0.9\,\mathrm{s}$ of UT1, a timescale based on Earth's rotation, through the addition of semi-annual leap seconds to International Atomic Time (TAI), a weighted average of some 200 atomic clocks maintained by Bureau International des Poids et Mesures (BIPM). (For a review of the various timescales, see Seidelmann, Guinot, & Doggett 1992). In a further correction, we use retroactive updates of TAI published by BIPM to correct TOAs from UTC to the geocentric timescale of Terrestrial Time (TT[BIPM]), considered the most accurate time standard available.

1.5   Timing Analysis

This section reviews the timing model used to fit TOAs to a pulsar's astrometric, spin, and (where applicable) orbital behavior. The model is essentially a transformation from the telescope reference frame to the rest frame of the pulsar. It explains variations in pulse spacings observed at Earth in terms of the various delays experi-

enced by the pulses on their trip from the pulsar. The barest model incorporates the pulsar's celestial coordinates, its DM, and its spin parameters. These are enough to account for the three largest trends in the data: light travel-time across the solar system, dispersive delay in the ISM, and the spin-down mechanism. Smaller-amplitude effects, if discernible, necessitate additional parameters. These might include the pulsar's proper motion and time derivatives of the DM. A binary pulsar needs a set of Keplerian and possibly also post-Keplerian terms to handle delays caused by orbital motion.

1.5.1   Solar System Delays

Arrival times are measured in the telescope reference frame. Yet a telescope, sitting on a spinning planet that revolves around the Sun, is obviously not in the co-moving pulsar frame. To carry out the transformation from the telescope frame to the pulsar frame it is convenient first to translate the TOAs to the solar system barycenter (SSB). With respect to nearby pulsars, at least, the SSB has roughly zero net acceleration, making it good approximation to the frame in which the pulses were emitted (or for binary pulsars, the barycenter of the pulsar system). With respect to distant pulsars, on the other hand, the SSB experiences differential Galactic accelerations that prevent it from being exactly an inertial frame. The accelerations do not invalidate the SSB-centered timing model, but they do perturb some of the derived timing parameters from their intrinsic values (for discussion, see § 3.4.4).

If t and t_b are TOAs in the topocentric and SSB frames, respectively, then the transformation between them is given by

$$t_b - t = \frac{\mathbf{r} \cdot \hat{\mathbf{n}}}{c} + \frac{(\mathbf{r} \cdot \hat{\mathbf{n}})^2 - |\mathbf{r}|^2}{2cd} - \frac{D}{f_b^2} + \Delta_{E\odot} - \Delta_{S\odot}, \qquad (1.9)$$

where $\mathbf{r}$ is the vector from the SSB to the telescope phase center, $\hat{\mathbf{n}}d$ is the displacement vector from the SSB to the pulsar, and c is the speed of light. Going from left

to right, the terms on the right hand side have the following interpretations. The first two terms account for the arrival-time difference between the stationary SSB and the Earth moving in its 500-second wide orbit. The first of these terms, the annually varying "Roemer delay", $(\mathbf{r} \cdot \hat{\mathbf{n}})/c$, approximates the pulsar signal as an infinite plane wave. The second term corrects for the fact that the pulses are actually spherical waves emanating from a finite distance d, and is important only for nearby pulsars. In the third term, f_b is the observing frequency in the SSB frame. It is the frequency at which the pulsar signal crossed the ISM, and it differs from the observing frequency in the telescope frame, f, due to Earth's orbital motion. Subtracting D/f_b^2, where $D \equiv \mathrm{DM}\, e^2/2\pi m_e c$, shifts the TOA to infinite observing frequency, facilitating comparison with arrival times measured at other bands. (The pulsar-to-SSB light travel time, d/c, could also be also be subtracted from right hand side of eqn. 1.9 so that t_b gives the actual time that the pulse was emitted. But it is omitted because the fitting procedure ignores constant terms.) Last are two relativistic terms. The "Einstein delay", $\Delta_{E\odot}$, combines the effects of time dilation from Earth's motion and gravitational redshift from bodies in the solar system. The "Shapiro delay", $\Delta_{S\odot}$, accounts for extra propagation time accumulated as the pulse traverses the gravitational potential well of the Sun. It has a maximum value of about $120\,\mu$s for pulses grazing the solar limb and becomes negligible at small pulsar-Sun-Earth angles.

The transformation in equation 1.9 implicitly contains a total of six free parameters: the right ascension and declination of the pulsar, α and δ; the components of its proper motion, $\mu_\alpha = \dot{\alpha}\cos\delta$ and $\mu_\delta = \dot{\delta}$; the DM; and parallax, $\pi = 1/d$. Solar system ephemerides must be interpolated to evaluate $\mathbf{r}$. In this thesis, we rely exclusively on the JPL DE200 ephemeris (Standish 1990). We use data from the International Earth Rotation Service, tabulated in UT1, to make retroactive adjustements for irregularities in Earth's rotation.

1.5.2   The Solar Electron Density

The charged solar wind disperses the pulsar signal, causing still another delay. Compensating for it requires a model of the free electron density in the solar system. Issautier *et al.* (2001) find that the density scales with radial distance from the Sun as $1/r^2$ over a wide range of heliocentric latitudes. Their result is based on data taken in 2000 (at solar maximum) by the Ulysses probe on one of its circumpolar transits around the Sun. Accordingly, we model the density as

$$n_e^{\text{solar}}(r) = \frac{n_0}{r^2}, \tag{1.10}$$

with r in astronomical units (A.U.) and n_0 in cm^{-3}. At each observation, the component of DM due to the solar wind is found by integrating equation 1.10 along the path to the pulsar. The biggest delay occurs when Earth and the pulsar are on opposite sides of the Sun. It can be shown that for a wave propagating at frequency f in MHz, the maximum delay is (relative to a wave at infinite frequency)

$$\begin{aligned}
\Delta t_{\text{max}} &\simeq \frac{e^2}{2\pi m_e c} \frac{n_0 \beta}{|\sin \beta|} \frac{1}{f^2} (1 \text{ A.U.}) \\
&\simeq (2.0 \times 10^{-2}) \frac{n_0 \beta}{|\sin \beta|} \frac{1}{f^2} \text{ s}, \tag{1.11}
\end{aligned}$$

where β is the pulsar's ecliptic latitude. The results of Issautier *et al.* (2001) imply that $n_0 \sim 10 \text{ cm}^{-3}$, and we use this as the default value in our work. Since the solar delay is too small to be noticeable for most the MSPs in this thesis, the precise value of n_0 is usually unimportant. But for a source that has either extremely precise timing or a small impact parameter with the Sun, the delay is detectable, and it has the potential to bias our measurement of the pulsar's astrometric parameters. In that case, we fit for n_0 as a free parameter. The $1/r^2$ model is admittedly an oversimplification. It accounts for the biggest effect of the solar wind, namely, the delay from the annually varying line of sight to the pulsar. But it neglects the
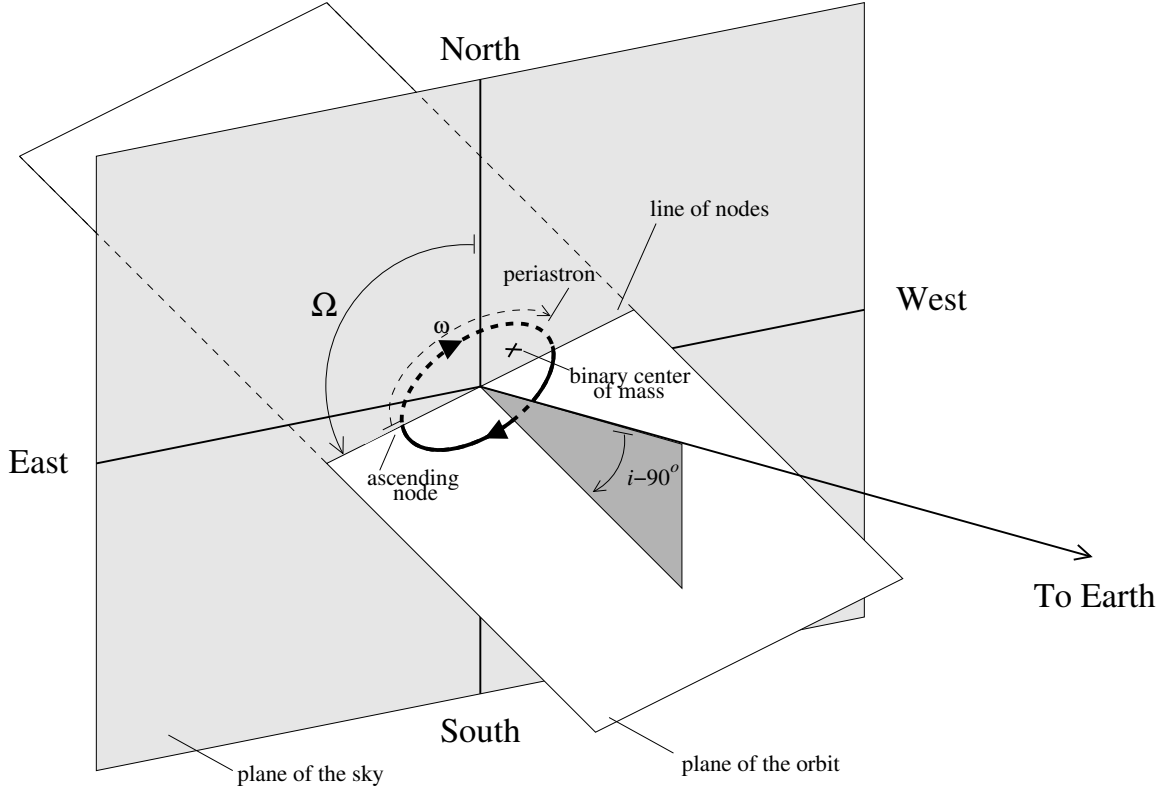
Figure 1.3: Orbital geometry: ω is the angle of periastron, i is the orbital inclination, and Ω is the longitude of the ascending node.

difference between the high-density wind along the ecliptic and the low-density wind at high latitudes. Nor does it allow for time variations in n_0 that must result from the approximately 11-year cycle of sunspot activity.

1.5.3   Orbital Delays

For an isolated pulsar, equation 1.9 completes the transformation to the pulsar frame. The proper time of pulse emission is then $T = t_b$. But for a binary pulsar, a further

transformation is need to translate t_b from the barycenter of the pulsar system to the frame of the pulsar itself. This requires a model of orbital motion. At a minimum, five Keplerian parameters are needed to characterize the orbit: the eccentricity, e; the binary period, P_b; the longitude of periastron, ω; the epoch of periastron, T_0; and the semimajor axis projected onto the plane of the sky, $x \equiv (a_1 \sin i)/c$, where a_1 is the semi-major axis and i is the orbital inclination angle (an edge-on orbit has $i = 90°$). Figure 1.3 illustrates the orbital geometry. Under Kepler's third law, i combines with the pulsar mass, m_1, and the companion mass, m_2, to form the "mass function":

$$f_1(m_1, m_2, i) \equiv \frac{(m_2 \sin i)^3}{(m_1 + m_2)^2} = x^3 \left(\frac{2\pi}{P_b}\right)^2 \left(\frac{1}{T_\odot}\right), \tag{1.12}$$

where $T_\odot \equiv GM_\odot/c^3 = 4.925490947\,\mu s$ is the mass of the Sun in temporal units, G is Newton's gravitational constant, and m_1 and m_2 are in solar masses.

The model requires additional, post-Keplerian (PK) parameters if the orbit is rapid or eccentric enough, or oriented suitably with respect to the line of sight, to bring relativistic effects into play. Taylor & Weisberg (1989) review formalisms for computing these higher-order delays. Nowadays, the most comprehensive orbital model is that of Damour & Deruelle (1986) (herafter DD), who solved the relativistic two-body problem to order v_{orb}/c. They made only general assumptions about strong-field gravity, keeping their description independent of any one theory; intepreting the model within the context of a specific theory, such as general relativity (GR), is done by assigning particular relations among the parameters.

The orbital transformation from t_b to T is

$$T - t_b = t_0 - \Delta_R - \Delta_E - \Delta_S - \Delta_A, \tag{1.13}$$

where t_0 is a reference epoch in the SSB timescale. The terms Δ_R, Δ_E, and Δ_S are analogous to the Roemer, Einstein, and Shapiro delays in the solar system, while Δ_A is an aberration delay caused by the pulsar's rotation. In the DD model, the delays

are:

$$
\Delta_R = x \sin\omega[\cos u - e(1 + \delta_r)] +
$$
$$
x[1 - e^2(1 + \delta_\theta)^2]^{1/2} \cos\omega \sin u, \tag{1.14}
$$

$$
\Delta_E = \gamma \sin u, \tag{1.15}
$$

$$
\Delta_S = -2r \ln\{1 - e\cos u - s[\sin\omega(\cos u - e) +
$$
$$
(1 - e^2)^{1/2} \cos\omega \sin u]\}, \tag{1.16}
$$

$$
\Delta_A = A\{\sin[\omega + A_e(u)] + e\sin\omega\} +
$$
$$
B\{\cos[\omega + A_e(u)] + e\cos\omega\}. \tag{1.17}
$$

The eccentric anomaly, u, and the true anomaly, $A_e(u)$, both range from 0 to 2π and are defined as

$$
u - e\sin u = 2\pi \left[\left(\frac{T - T_0}{P_b} \right) - \frac{\dot{P}_b}{2} \left(\frac{T - T_0}{P_b} \right)^2 \right], \tag{1.18}
$$

$$
A_e(u) = 2\arctan \left[\left(\frac{1 + e}{1 - e} \right)^{1/2} \tan\frac{u}{2} \right]. \tag{1.19}
$$

Equations 1.14-1.19 contain a total of 11 free PK parameters: the rate of change of binary period, $\dot{P}_b$; the "range" and "shape" of Shapiro delay, r and s; the combined effect of time dilation and gravitational redshift, γ; the orbital shape corrections, δ_r and δ_θ; the aberration parameters, A and B; the rate of change of periastron, $\dot{\omega}$, defined implicitly through

$$
\omega = \omega_0 + \frac{\dot{\omega} P_b}{2\pi} A_e(u); \tag{1.20}
$$

and the time derivatives of the projected semimajor axis and the eccentricity, $\dot{x}$ and $\dot{e}$, obtained through

$$
x = x_0 + \dot{x}(T - T_0), \tag{1.21}
$$

$$
e = e_0 + \dot{e}(T - T_0). \tag{1.22}
$$

General Relativity

Interpreted specifically within GR, the PK parameters of the DD model have the formulas:

$$\dot{\omega} = 3n^{5/3}(1-e^2)^{-1}M^{2/3}T_\odot^{2/3}, \tag{1.23}$$

$$\gamma = n^{-1/3}em_2(m_1+2m_2)M^{-4/3}T_\odot^{2/3}, \tag{1.24}$$

$$\dot{P_b} = -\frac{192\pi}{5}n^{5/3}f_em_1m_2M^{-1/3}T_\odot^{5/3}, \tag{1.25}$$

$$r = m_2T_\odot, \tag{1.26}$$

$$s \equiv \sin i = xn^{2/3}m_2^{-1}M^{2/3}T_\odot^{-1/3}, \tag{1.27}$$

$$\delta_r = n^{2/3}(3m_1^2+6m_1m_2+2m_2^2)M^{-4/3}T_\odot^{2/3}, \tag{1.28}$$

$$\delta_\theta = n^{2/3}\left(\frac{7}{2}m_1^2+6m_1m_2+2m_2^2\right)M^{-4/3}T_\odot^{2/3}, \tag{1.29}$$

$$A = \frac{P}{2\pi}x^{-1}n^{-1/3}(1-e^2)^{-1/2}m_2^2M^{-4/3}T_\odot^{2/3}, \tag{1.30}$$

$$B = 0, \tag{1.31}$$

where

$$f_e = \left(1+\frac{73}{24}e^2+\frac{37}{96}e^4\right)(1-e^2)^{-7/2}, \tag{1.32}$$

$$n = \frac{2\pi}{P_b}, \tag{1.33}$$

$$M = m_1+m_2 \tag{1.34}$$

(Taylor and Weisberg 1989; Arzoumanian 1995). If GR is assumed to be the correct theory of gravity, then measuring any one PK parameter (together with the mass function in eq. 1.12) constrains m_1 and m_2. Measuring two PK parameters is sufficient to determine both masses. And measuring three or more PK parameters overdetermines the masses, permitting tests of GR. Briefly, this involves plotting the parameter curves prescribed by GR in the m_1-m_2 plane and verifying that they all intersect at the same point (for example, see Stairs *et al.* 2002).

1.5.4 Spin-Down Model

The pulsar spin-down mechanism is modeled through a Taylor expansion of the pulse phase in proper time:

$$\phi(T) = \phi_0 + \nu T + \frac{1}{2!}\dot{\nu}T^2 + \frac{1}{3!}\ddot{\nu}T^3 + \cdots, \tag{1.35}$$

where ϕ is in cycles, ϕ_0 is the phase at $T = 0$, and $\nu = 1/P$ is the spin frequency. If the spin-down trend is attributed entirely to dipole radiation from a pulsar whose magnetic moment is orthogonal to its spin axis, then measurements of ν and $\dot{\nu}$ produce an estimate of the surface magnetic field strength:

$$B = \left(\frac{-3I\dot{\nu}c^3}{8\pi^2 R^6 \nu^3}\right)^{1/2} \approx 3.3 \times 10^{19}(P\dot{P})^{1/2}\,\mathrm{G}, \tag{1.36}$$

where a neutron star mass of $m_1 = 1.4\,\mathrm{M_\odot}$ and a radius of $R = 10^6\,\mathrm{cm}$ have been assumed, yielding a moment of inertia of $I = (2/5)m_1 R^2 \approx 10^{45}\,\mathrm{g\,cm^2}$.

The spin frequency is usually taken to obey

$$\dot{\nu} \propto \nu^n. \tag{1.37}$$

In that case, all higher derivatives can be written in terms of ν, $\dot{\nu}$, and n. They are expected to become negligibly small as their order grows, with $\dot{\nu}/\nu \approx \ddot{\nu}/\dot{\nu}$, and so on. In a few young pulsars, the "braking index" that classical electrodynamics predicts for a rotating magnetic dipole, $n = 3$, can be compared with experiment via $n = (\nu\ddot{\nu})/\dot{\nu}^2$. In MSPs, braking torques are expected to be too small to produce a measurable $\ddot{\nu}$, but it and higher derivatives are sometimes included in the parameter fit as a way of cleansing the data of unexplained stochastic trends.

Integrating equation 1.37 leads to an estimate of the pulsar age:

$$\tau = \frac{-1}{n-1}\frac{\nu}{\dot{\nu}}\left[1 - \left(\frac{\nu}{\nu_0}\right)^{n-1}\right]. \tag{1.38}$$

For young pulsars, it can be safely assumed that $\nu \ll \nu_0$, in which case taking $n = 3$ yields the useful approximation

$$\tau = -\frac{\nu}{2\dot{\nu}}.$$ (1.39)

For MSPs, it is more likely that $\nu \approx \nu_0$, since angular deceleration proceeds slowly following the spin-up. In that case, the approximation in equation 1.39 is illegitimate and can produce unrealistically large ages estimates, sometimes giving numbers that are larger than the age of the universe.

1.5.5   The TEMPO Software Package

To fit for parameters in the transformation from topocentric time t to proper time T, we, like most of the pulsar-timing community, make use of the TEMPO software package. Developed in the 1970s by J. H. Taylor and R. N. Manchester and updated continually since then to handle ever-subtler effects, the program performs an iterative least-squares fit to the data, starting with an initial set of timing parameters and modifying them to minimize the goodness-of-fit statistic

$$\chi^2 = \sum_{i=1}^{N} \left(\frac{\phi[T_i(t_i)] - n_i}{\sigma_i/P_i} \right)^2,$$ (1.40)

where $\phi[T_i(t_i)]$ is the pulse phase at proper time T_i (derived from arrival time t_i), N is the total number of TOAs, n_i is the integer closest to the computed value of $\phi[T_i(t_i)]$, σ_i is the measurement uncertainty in t_i, and P_i is the pulse period at T_i. For the fitting procedure to work, each TOA, t_i, must be assigned to a unique pulse number, n_i. Getting a timing solution to be "phase connected" like this entails considerable trial-and-error when a pulsar is discovered. Once it is accomplished, however, the numbering of pulses usually ceases to be an issue for well-studied pulsars. In relying on the absolute phase of the clock signal rather than its frequency, the fitting procedure in equation 1.40 is actually somewhat different from the analogy of the Doppler-shifted siren at the beginning of the chapter. But it is also a good deal more precise.

The output of the `TEMPO` consists of the best-fit parameters, their covariance matrix, and a set of residuals, each the difference between the predicted and the observed arrival time. As will be amply demonstrated in later chapters, plots of residuals are the stock-in-trade of pulsar timing. A perfect fit leaves behind residuals with the character of Gaussian noise. Deficiencies in a fit show up in the residuals as non-Gaussian trends whose shapes provide clues to the phenomena left unmodeled.

There are two subtleties involved in combining sets of TOAs taken with different telescopes, observing frequencies, or data-taking systems. First, `TEMPO` fits for arbitrary time offsets between the data sets. These are necessary to account both for alignment discrepancies between standard profiles and for unequal signal delays through the various hardware. Second, in high-precision timing it often happens that, for ν degrees of freedom, the goodness-of-fit statistic, χ^2/ν, is significantly greater than unity. Most likely, this is because the TOA uncertainties, calculated as byproducts of profile cross-correlation, do not capture all sources of systematic error. To compensate, we add a fixed amount of error in quadrature to the statistical uncertainties of TOAs in each data set. The amounts are chosen so that $\chi^2/\nu \simeq 1$ for each data set in the final fit.

Chapter 2

The Long-Term Timing Project

Now that pulsar timing has been described, it becomes possible to explain the work done in this thesis. Briefly, we looked at a half dozen MSPs over a period of more than four years. The observations were carried out monthly (and sometimes more frequently) at the Arecibo observatory. The data-taking sessions gathered high-precision TOAs that, when added to measurements taken earlier, form data sets spanning between six and seventeen years. In the chapters that follow, we perform timing analyses on these long-term data sets. Our main goals are to improve the precision of known parameters and to detect previously unmeasured ones. We focus on those parameters that constrain the star masses in binary systems.

2.1   History of Long-Term Timing at Arecibo

The radio dish at Arecibo is stationary. The telescope is pointed by means of receivers on a movable platform above the dish. The suspended platform can rotate through the full azimuthal circle, and it can traverse zenith angles between $0°$ and $19.7°$[1]. Situated at a latitude of $18°21'$ north, the telescope has a declination range (in J2000

---

[1]Telescope specifications are listed at http://www.naic.edu/∼astro/guide/node2.html.

coordinates) of $-1°20' < \delta < +38°02'$. This is fairly restrictive. Not only does the telescope cover a solid angle of just 1.30π steradians, so that it misses 68% of the sky and hence many observable pulsars, but also a pulsar that does come within its beam will be in view for at most 2.7 hrs per day, which is considerably less time than the horizon-to-horizon tracking provided by steerable dishes. Yet the disadvantage of short integration times is made up for by the collecting area of the 305 m (1000 ft) dish. In fact, the sensitivity of the telescope at observing frequencies of ~ 1 GHz makes Arecibo the best facility in the world for timing MSPs.

Regular observations of fast-rotating pulsars at Arecibo began in 1974 following the discovery of the double-neutron-star binary PSR B1913+16 (Taylor & Weisberg 1989 and references therein). In 1982, the first detection of an MSP, PSR B1937+21 (Backer *et al.* 1982), led to a program of biweekly observations that eventually encompassed other sources, including PSR 1957+20 (Arzoumanian, Fruchter, and Taylor 1994) and PSR B1855+09 (Kaspi, Taylor, and Ryba 1994). The project came to a temporary halt in 1994 when the telescope shut down for renovations. Among the improvements were new Gregorian receivers, which allowed wider bandwidths and greater frequency agility, and a 15 m (50 ft) groundscreen around the dish, which improved system temperature at high zenith angles.

We began taking data for this thesis when the telescope reopened in 1998. Once a month, between 1998 and 2001, we observed roughly a dozen MSPs in a continuous session lasting 22 hours. The sources were chosen to accommodate the research preferences of the four participating universities: Princeton, Berkeley, Caltech, and Penn State. Midway through 2001, Princeton and Berkeley alone assumed responsibility for the project, and the roster of MSPs shrank by about half, concentrating now on multi-frequency observations of the best sources. The latest TOAs in this work were taken at the end of 2002. But the observations continue, with the Arecibo

Table 2.1: Pulsars Studied

Name	P (ms)	Number of TOAs	Data Span (yr)
J0621+1002	28.9	780	6.29
J0751+1807	3.48	2522^a	7.94
J1713+0747	4.57	252	10.1
B1855+09	5.36	411	17.0
J2033+1734	5.95	151	7.45
J2322+2057	4.81	102	10.8

[a]TOAs from all pulsars except PSR J0751+1807 are averaged from larger data sets following the procedure in Appendix A.

current proposal active through 2004. It is hoped that the long-term timing project will be extended beyond then, using newer-generation backends based on the software dedispersion technology of Princeton's Mark IV system.

Table 2.1 lists the MSPs studied in this thesis. Also included are their pulse periods, the total number of TOAs in each data set (a figure encompassing both data taken for this thesis and data taken by others, at Arecibo and elsewhere, that we use in our work), and the number of years spanned by each data set. In the last column, the rms postfit residual indicates the precision of our parameter fits. Of the six MSPs we studied, five orbit other stars. Table 2.2 summarizes their binary characteristics. We were able to measure one or more PK parameters, and hence get a handle on i, m_1, and m_2, for all the binaries save PSR J2033+1734.

Table 2.2: Summary of Orbital Elements

Name	P_b (d)	e	x (lt-s)	i (deg)	m_1 (M$_\odot$)	m_2 (M$_\odot$)	PK Parameters Measured
J0621+1002	8.32	0.0025	12.0	30	1.70	0.97	$\dot{\omega}$
J0751+1807	0.263	0.0000033	0.397	74	2.34	0.20	r, s, $\dot{P_b}$
J1713+0747	67.8	0.000075	32.3	68	1.85	0.36	r, s, $\dot{x}^a$
B1855+09	12.3	0.000022	9.23	87	1.58	0.27	r, s
J2033+1734	56.3	0.00013	20.2	—	—	0.22^b	—

^{a}Measured $\dot{x}$ is a geometrical rather than relativistic effect.

^{b}Not measured. Based on assumed values of $i = 60°$ and $m_1 = 1.35\,\mathrm{M}_\odot$.

2.2   Scientific Motivation

2.2.1   Improving Parameter Estimates

As stated earlier, our main scientific goal is to study the orbital characteristics of binary MSPs. Other aspects of the pulsars—such as their positions and proper motions—are also of interest. But we concentrate on PK orbital elements and what they imply for the system masses. In this regard, the motivation behind monthly timing observations is that they improve our parameter estimates.

The uncertainties of the fitted parameters shrink as the number of data points grows, but not all PK parameters benefit to the same extent from lengthening the timespan T of the observations. For systems where the parameters are detectable, it can be shown that the statistical errors of $\dot{P_b}$, $\dot{\omega}$, and the pair r and s scale as $T^{-5/2}$, $T^{-3/2}$, and $T^{-1/2}$, respectively. These are rough dependencies. They assume uniform sampling throughout the timespan. They neglect covariances among the timing parameters. They also ignore special properties (like an edge-on orbital inclination) that enhance the measurability of certain parameters in some systems. An analysis of parameter detectability that takes these factors into account can be performed by

simulating arrival times with measurement errors similar to those of existing TOAs (Damour and Taylor 1992; Taylor 1992). With a decade of fake data, it is possible to estimate the extent to which long-term timing will improve the fractional parameter uncertainties of a given MSP. The results are broadly consistent with the scaling rules listed above.

2.2.2   A Pulsar Timing Array

Besides honing our parameter estimates, the other motivation for long-term timing is that it can uncover physics outside the timing model. In our data, for example, we find DM variations in PSR J0621+1002 and timing noise in PSR J1713+0747. Both effects are random processes unaccounted for by the deterministic equations of motion.

Of all such phenomena, the most sought after—the Holy Grail of long-term timing, it might be said—is the gravity wave background (GWB), a hypothesized low-level noise in the spacetime metric. To date, the GWB has not been detected, although pulsar timing residuals have been used to put an upper limit on its energy density, assuming it exists. We do not deal with the GWB in our data analysis. In a division of labor, that job falls to our collaborators, while we at Princeton dwell on orbital modeling. Nevertheless, the quest for the GWB is such an important driver of the the long-term timing program that it merits some discussion.

Sazhin (1978) and Detweiler (1979) were the first to point out that a passing gravity wave would, in perturbing the position of Earth, cause the observed spin frequency of a pulsar to vary. To illustrate this, we follow Detweiler (1979) by placing Earth at the origin of a coordinate system and locating the pulsar in terms of the directional cosines α, β, and γ. A gravity wave propagating through the solar system

along the z direction gives the metric the form

$$ds^2 = -dt^2 + (1 + A_+)dx^2 + (1 - A_+)dy^2 + dz^2 + 2A_\times dx\,dy, \qquad (2.1)$$

where the amplitudes of the wave polarizations, A_+ and $A_\times$, are assumed to be much smaller than unity. Because of this metric distortion the observed spin frequency will be redshifted away from the frequency it would have in the absence of a gravity wave, ν_0, by a fractional amount

$$\frac{\delta\nu(t)}{\nu_0} = \frac{(\alpha^2 - \beta^2)A_+(t) + 2\alpha\beta A_\times(t)}{2(1 + \gamma)}. \qquad (2.2)$$

This redshift produces a signal in the postfit timing residuals,

$$R(t) = \int_0^t dt \frac{\delta\nu(t)}{\nu_0}, \qquad (2.3)$$

which is potentially detectable for a strong enough gravity wave, precise enough TOAs, or both. Equation 2.1 describes gravity waves hitting Earth. Hellings & Downs (1983) point out that the residuals will also bear traces of gravity waves that hit the pulsar at the time the pulses were sent. In principle, the two signals can be disentangled by observing multiple pulsars. In that case, gravity-wave disturbances that occurred at Earth will be correlated among the different pulse streams while those that took place at the individual sources will be independent.

Detweiler (1979) showed further that the GWB will contribute to the timing residuals some amount of root-mean-square (rms) noise, σ_g, in excess of the expected statistical scatter. The noise corresponds to a GWB energy density of

$$\rho_g = \frac{1}{G} \frac{243\pi^3}{208} f^4 \sigma_g^2. \qquad (2.4)$$

(It is assumed here that the GWB is a random process with a flat energy spectrum over a bandwidth f centered at frequency f.) An upper limit to the energy density is obtained by ascribing the total rms scatter of the residuals, σ_total, to the GWB.

The limit can be expressed as a fraction of the closure density of the universe, $\rho_c = 3H_0^2/8\pi G$, via

$$\frac{\rho_g}{\rho_c} \leq \frac{81\pi^4}{26H_0^2}f^4\sigma_{\text{total}}, \tag{2.5}$$

where H_0 is the Hubble constant. Related to ρ_g is Ω_g, the energy density of gravitational waves per logarithmic frequency interval, normalized by the closure density:

$$\Omega_g(f) \equiv f\frac{\rho_g}{\rho_c} \tag{2.6}$$

(Blandford, Narayan, and Romani 1984; Scarrott, Rolph, and Tadhunter 1990). If the GWB dominates the pulsar timing residuals, then their power spectrum will be given by

$$\begin{aligned} P_g(f) &= \frac{H_0^2}{8\pi^4}\Omega_g f^{-5} \\ &= 1.34 \times 10^4 \Omega_g h^2 f^{-5} \mu s^2 \text{yr}, \end{aligned} \tag{2.7}$$

where f is in yr^{-1} and the Hubble constant is expressed as $H_0 = 100h\,\text{km}\,\text{s}^{-1}\,\text{Mpc}^{-1}$, with h a numerical constant. Using data from PSR B1855+09, Kaspi *et al.* (1994) derived the limit $\Omega_g h^2 < 6 \times 10^{-8}$ (95% confidence) at frequencies of $f \approx 1/7\,\text{yr}^{-1}$ ($4.5 \times 10^{-9}\,\text{Hz}$). Re-analyzing the same data with different statistics, Thorsett & Dewey (1996) found $\Omega_g h^2 < 1.0 \times 10^{-8}$ (95% confidence).

In the model above, the Earth-pulsar line of sight is analogous to an arm of the Laser Interferometric Gravitational-Wave Observatory (LIGO) (Abramovici *et al.* 1992). In LIGO, a laser beam bounces between mirrored test masses at the ends of two orthogonal tunnels 4 km (2.5 mi) in length. The apparatus is designed so that a gravity wave traveling perpendicular to the arms will alter the tunnel lengths, shifting the laser frequencies in them by $\Delta\nu/\nu = \pm A_+$ and producing detectable interference.

Despite the similarity between LIGO and a detector in which Earth and a pulsar are the test masses, there are important differences between the two experiments. For example, LIGO and the Earth-pulsar detector respond to waves of vastly different

frequency and amplitude. LIGO is sensitive to frequency $f \sim 100\,\mathrm{Hz}$ and dimensionless amplitude $A \sim 10^{-22}$. Waveforms detectable in this range should come from coalescing binaries, asymmetric supernovas, and pulsars. An Earth-pulsar detector, meanwhile, is optimally sensitive to frequencies down to $f \sim 1/T$, where T is the timespan of the TOA set, and to dimensionless strains of $A \sim \sigma_t/T$, where σ_t is the average measurement uncertainty of a TOA. Taking $T = 10\,\mathrm{yr}$ and $\sigma_t = 1\,\mu\mathrm{s}$ as typical numbers for an MSP, the quantities become $f \sim 10^{-9}\,\mathrm{Hz}$ and $A \sim 10^{-15}$. Where such long-wavelength gravitational radiation might come from is unclear. It might originate in bulk movements of matter that took place recently (i.e. in the last few billion years), such as in long-period massive black hole binaries at galactic centers (Lommen and Backer 2001). Or it could be a relic of the primordial universe, like the CMB. In a review of the physics of the stochastic GWB, Allen (1997) cites three possible early-universe sources: cosmic strings, quantum mechanical zero-point fluctuations amplified by inflation, and bubbles of low energy density produced by first-order phase transitions in the early universe.

Another difference between LIGO and an Earth-pulsar detector is in the factors that limit their performance. For LIGO, the biggest constraints on frequency range are thermal, seismic, and photoelectron shot noise. For an Earth-pulsar detector, meanwhile, sensitivity will be reduced by fitting for the star's timing parameters, which unavoidably removes a portion of the GWB's power from the postfit residuals (Blandford, Narayan, and Romani 1984). Sensitivity will also be diminished by any unmodeled phenomena that might masquerade in the residuals as the GWB. For this reason, several authors have suggested that an Earth-pulsar detector could be improved by observing an array of MSPs instead of a single one (Hellings and Downs 1983; Romani 1989; Foster and Backer 1990). This would permit the main sources of systematic noise to be disentangled, for each would give rise to a different angular

pattern when the residuals were correlated from MSPs spaced apart on the sky. For example, errors in terrestrial reference clocks would produce a monopole signature, since they are independent of the position of the pulsars. Inaccuracies in the solar system ephemeris, which lead to an incorrect location for Earth in the timing model, would generate a dipole signature. The buffeting of Earth by gravity waves would show up in the array as a quadrupole signature.

2.3 Data-Taking Hardware at Arecibo

2.3.1 The Princeton Mark IV System

The data in this thesis come from a variety of observing systems, but the majority of TOAs—and the ones acquired specifically for this thesis—come from the Princeton Mark IV baseband recorder. Stairs *et al.* (2000) have described the system in detail. Here we give a brief summary. Later chapters will describe the other data-taking devices used in our analysis.

On the hardware side, Mark IV accepts intermediate-frequency (IF) voltage signals of bandwidth B (either 5 or 10 MHz) that have been centered at 30 MHz and regulated in strength by adjustable attenuators. The signals are mixed to baseband in quadrature with local oscillators (LOs) at 30 MHz to produce, for each of two orthogonal polarizations, a real and imaginary signal with passband 0 to $B/2$. The four resulting signals are low-pass filtered and then digitized with four bits (for $B = 5$ MHz) or two bits (for $B = 10$ MHz). The signals are time-stamped with a 10-s tick from the observatory master clock. Finally, the data stream, flowing at a rate of $10\,\mathrm{MB\,s^{-1}}$, is routed through a workstation for storage on either a pair of Digital Linear Tapes (DLTs) or a disk array.

The data are analyzed after the observation. Mark IV performs coherent dedis-

persion (§ 1.4.4) in software. To convolve the signal with the inverse "chirp" function, Mark IV uses a 1.25-Gflop parallel processor optimized for fast Fourier transforms (FFTs). Optional techniques for excising narrow-band and broad-band radio frequency interference (RFI) are also applied at this stage. The dedispersed data stream consists of four cross-products: $|L|^2$, $|R|^2$, Re(L*R), and Im(L*R), where L and R are the voltage streams from the left and right polarization channels, respectively. When used for pulsar timing, Mark IV folds the cross products modulo the anticipated pulse period over 10-s intervals, and the resulting accumulated profiles are then summed to produce total-intensity profiles: $I = |L|^2 + |R|^2$. A number of these 10-s profiles— typically 19—are averaged (using their signal-to-noise ratios as weights) to produce the integrated profiles from which TOAs are measured (§ 1.4.5). An important step before summing the profiles is calibrating the relative strengths of the two polarizations. This is done at the end of each scan using a 1-min noise pulse fed through the signal path. The noise pulse, in turn, is calibrated against a catalogued astronomical source.

2.3.2   A Test of Timing Precision

If the timing data are free of systematic errors, then the root-mean-square (RMS) postfit timing residual should shrink with integration time as $t_{\mathrm{int}}^{-1/2}$. To see whether this is fulfilled for Mark IV, we observed two MSPs, PSRs B937+21 and J1713+0747, for 30 minutes across a 10 MHz bandpass at a frequency of 1410 MHz. (For a detailed description of the test, see Stairs *et al.* 2000.) Briefly, TOAs were computed for integration times ranging from 1 to 640 s and fitted to a timing model. The RMS residual was computed for each integration time. Figure 2.1 shows the results. The residuals of PSR J1713+0747 scale as expected with a slope of $-1/2$. The fall-off at large integration times is evidently an artifact of calculating RMS with a small
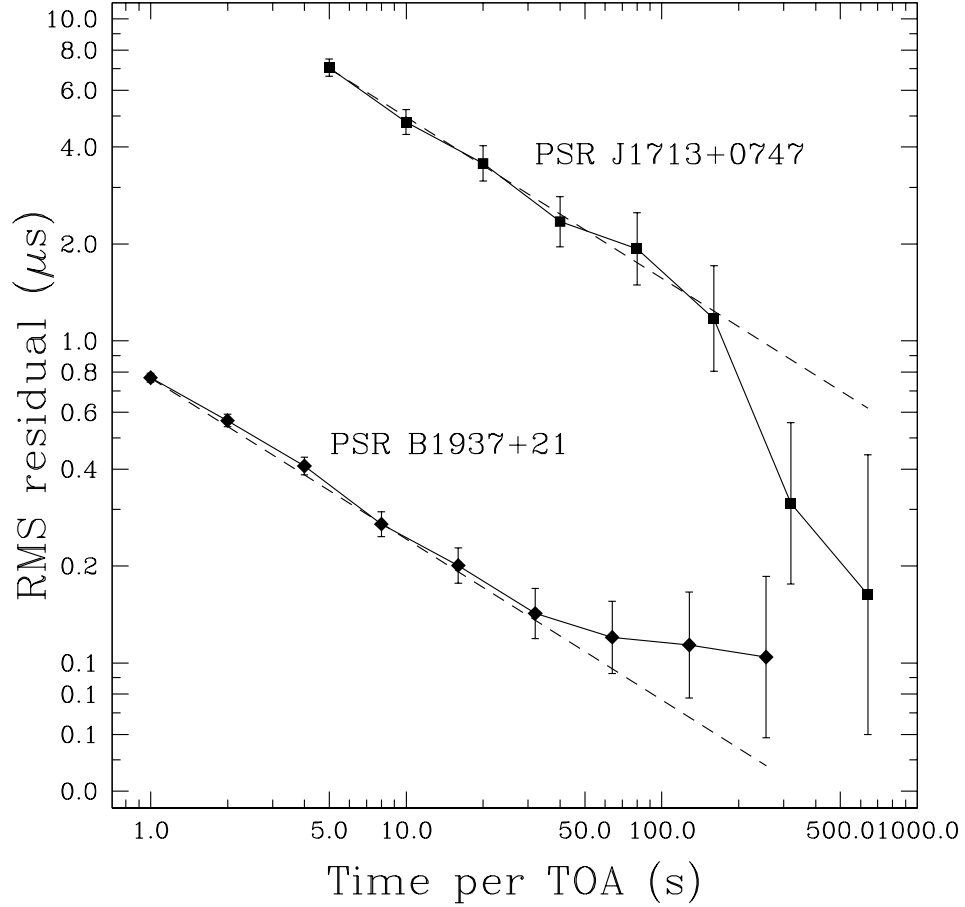
Figure 2.1: Test of timing precision for Mark IV. The points are the RMS timing residuals of PSRs B1937+21 and J1713+0747 as a function of integration time. The dashed lines indicate slopes of $-1/2$, corresponding to the expected scaling laws.

number of points. For PSR B1937+21, the scaling law is obeyed down to an RMS residual of about 100 ns, at which point a flattening out of the slope indicates the presence of systematic effects that set a floor on timing precision. These are most likely from the ISM or the pulsar itself and not from the instrument.

Chapter 3

PSR J1713+0747: An Almost Perfect Clock

3.1 Introduction

Some pulsars are prized for the unpredictability of their timing, like the ones that glitch or have erratic orbital periods. MSPs, on the other hand, are valued because their behavior offers few surprises. Their pulses are so regular that a simple deterministic model is capable of tracking every arrival time over a decade or longer with residual errors smaller than a microsecond. Most MSPs make good clocks. But a few stand out as truly exceptional timers thanks to a strong signal and an inherent stability that rivals that of the best terrestrial clocks. These objects have a range of esoteric uses, such as placing limits on secular changes in Newton's gravitational constant and testing man-made frequency standards (Kaspi, Taylor, and Ryba 1994; Matsakis and Foster 1996). In this chapter, we report on one member of this exclusive group, PSR J1713+0747, a pulsar with a 4.57-ms spin period in a 67.8-day orbit around a low-mass white dwarf.
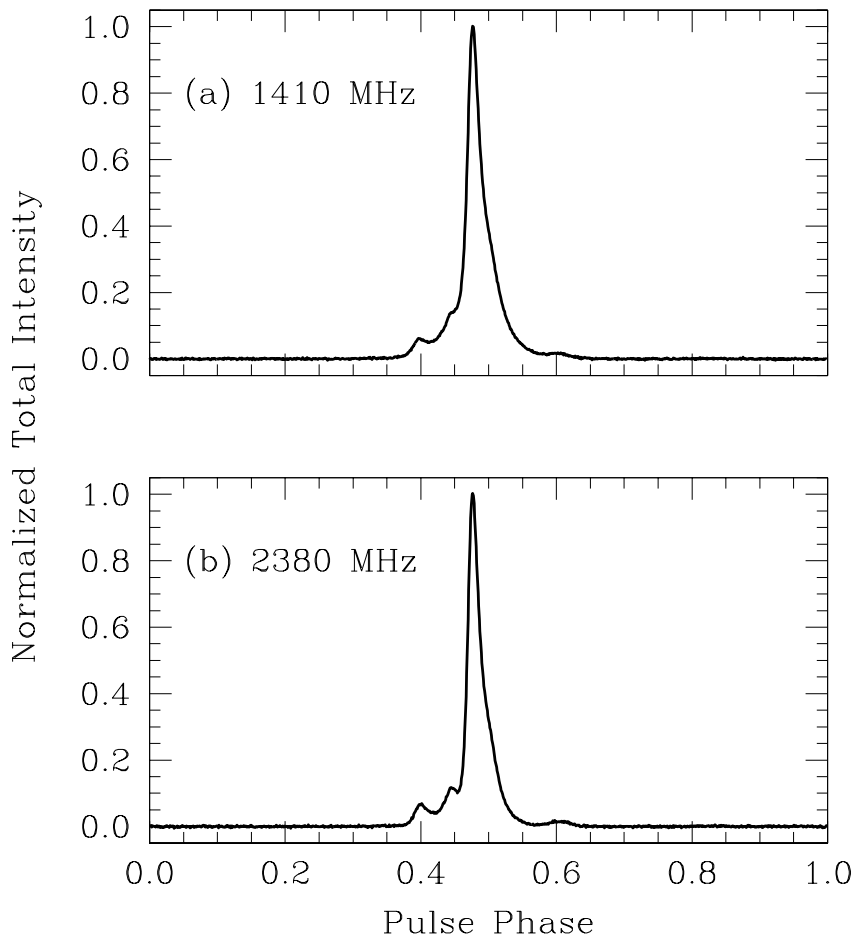
Figure 3.1: Pulse profiles of PSR J1713+0747 at (a) 1410 MHz and (b) 2380 MHz.

Discovered at Arecibo by Foster, Wolszczan, & Camilo (1993) during a pulsar search at high Galactic latitudes, PSR J1713+0747 was quickly recognized as a first-rate celestial clock. For one thing, it is a bright source, with flux densities at 1510 MHz and 2695 MHz of $S_{1510} = 8 \pm 2\,\mathrm{mJy}$ (Kramer *et al.* 1998) and $S_{2695} = 2.9 \pm 0.9\,\mathrm{mJy}$ (Kramer *et al.* 1999a), respectively. Consequently, it can be observed at higher bands where interstellar propagation effects are less likely to distort the pulses. On top of that, the pulse profile has a narrow peak that lends itself to accurate arrival-time measurement. Figure 3.1 shows the standard profiles of PSR J1713+0747 at both

1410 MHz and 2380 MHz. For a Gaussian profile (a good approximation here), the measurement uncertainty of a TOA is expected to be

$$\sigma_{\text{rms}} \simeq \left(\frac{\sigma_w}{P}\right)^{1/2} \frac{\sigma_w}{<S>} \left[\frac{T_k}{G(B\tau)^{1/2}}\right] \qquad (3.1)$$

(Backer 1989). The terms outside the brackets depend on the pulsar signal alone. They are σ_w, the half-width of the peak; P, the pulse period; and $<S>$, the continuum flux density of the source. The terms inside the brackets are specific to the receiving equipment. They are T_k, the system temperature; G, the telescope gain; B, the bandwidth, and τ, the integration time. The point here is that, telescope considerations aside, a sharp pulse profile and a strong signal earn better timing precision. This proves true for PSR J1713+0747. In hour-long Arecibo scans at 1410 MHz, its TOA uncertainties match the prediction of equation 3.1, $\sigma_{\text{rms}} \simeq 0.3 \, \mu$s. The sub-microsecond measurement error permits hard-to-detect timing effects to be detected, a virtue that was first demonstrated when Camilo, Foster, & Wolszczan (1994) were able to estimate the distance to pulsar and the mass of the secondary after a mere 22 months of data taking.

In this chapter, we add 51 more months of new and more precise TOAs to that original data set. In our updated analysis, we derive tighter measurements of the pulsar's position, proper motion, and PK orbital parameters. In particular, we obtain much more precise estimates of m_1 and m_2. We also detect a hitherto unseen secular variation in the projected semimajor axis, $\dot{x}$. This is a geometrical effect that stems from a gradual shift in the line of sight to the system, and not from any actual change in the orbital dimension. Intriguingly, the TOAs exhibit low-level systematic trends indicative of unmodeled physical effects. The apparently random signal does not compromise the orbital analysis, since its timescale far exceeds the binary period. Yet it does raise doubts about the suitability of the pulsar for high-precision metrology. Similar timing noise in PSR B1937+21 has inspired a wealth of possible explanations.

Table 3.1: Summary of Arecibo Observations of PSR J1713+0747

System	Dates	Frequency (MHz)	Bandwidth (MHz)	Number of TOAs	Typical Integration (min)	RMS Residual[a] (μs)
Mark III	1992.6–1993.0	1400	32×1.25	9	47	0.73^b
	1992.3–1994.1	1400	32×1.25	59	47	0.47^c
ABPP	1998.1–2002.1	1410	56	74	60	0.21
	1999.7–2002.1	2380	112	26	30	0.35
Mark IV	1998.6–2002.4	1410	10	55	58	0.23
	1999.8–2002.4	2380	10	29	29	0.31

[a]Values incorporate the effect of averaging TOAs from shorter integration times.
[b]Filter bank used a 78-μs time constant.
[c]Filter bank used a 20-μs time constant.

These include rotational instability; drifts in the manmade clocks used to time the MSP; the GWB (Kaspi, Taylor, and Ryba 1994); and an orbiting planet (Lommen and Backer 2001). The discovery of timing noise in PSR J1713+0747 comes as a disappointment, for we had hoped that the pulsar would be the ideal timer that PSR B1937+21 is not. But if the phenomenon attracts equally fruitful examination, it will be adequate compensation for the loss of a perfect clock.

3.2   Observations

Table 3.1 summarizes the observations. All the data in this chapter come from Arecibo. The 252 TOAs were taken on 166 days between 26 April 1992 and 20 May 2002. A shutdown of the telescope for an upgrade caused the gap between 1994 and 1998.

Prior to the upgrade, 68 TOAs were collected at roughly biweekly intervals. These points have already been studied by Camilo, Foster, & Wolszczan (1994). They

acquired the data with the Princeton Mark III observing system (Stinebring *et al.* 1992). The incoherent-dedispersion unit employed a $2 \times 32 \times 1.25$ MHz filterbank, with 32 spectral channels for each sense of polarization. The square-law detected outputs of each channel were smoothed with a time constant of $20 \, \mu$s or $78 \, \mu$s before being time-shifted, folded, and summed to build integrated total-intensity profiles of 256 bins.

The new, post-upgrade data consist of 184 TOAs obtained on 98 different days at approximately monthly intervals. A typical day's run devoted an hour to observing at 1410 MHz and a half hour to 2380 MHz. Two separate backends, Princeton's Mark IV system and the Arecibo-Berkeley Pulsar Processor (ABPP), acquired the data. The ABPP is a multi-channel instrument that applies coherent dedispersion to each channel. The total bandwidth of the ABPP depends on both the DM of the source and the observing frequency. For PSR J1713+0747, with DM $= 16.0 \, \text{pc} \, \text{cm}^{-3}$, the bandwidth is 56 MHz at 1410 MHz and 112 MHz at 2380 MHz. The ABPP took 180-second scans to make profiles with 1998 bins at 1410 MHz and 1944 bins at 2380 MHz. Mark IV took 190-second scans to produce total-intensity profiles of 1024 bins at both observing frequencies. It should be pointed out that even though the ABPP and Mark IV operated simultaneously on 35 days, their TOAs are statistically independent on account of the the overwhelming bandwidth difference between the machines. To put it another way, while the ABPP sampled Mark IV's bandpass, it covered so much additional bandpass that the arrival times it measured were effectively different events in frequency space from the ones measured by Mark IV. This is confirmed empirically by a lack of correlation between the timing residuals of the two instruments over a day's observation.

Table 3.2: Astrometric and spin parameters of PSR J1713+0747[a].

Right ascension, α (J2000).............................	$17^{\mathrm{h}}13^{\mathrm{m}}49\overset{\mathrm{s}}{.}528285(1)$
Declination, δ (J2000)	$+07°47'37\overset{''}{.}53973(7)$
Proper motion in R.A., $\mu_\alpha = \dot\alpha\cos\delta$ (mas yr^{-1})........	4.664(6)
Proper motion in Dec., $\mu_\delta = \dot\delta$ (mas yr^{-1})..............	$-3.90(1)$
Parallax, π (mas).....................................	0.73(9)
Distance, d (kpc).....................................	*1.4(2)*
Composite proper motion, μ (mas yr^{-1})................	*6.082(9)*
Galactic longitude, l (deg).............................	*28.7506*
Galactic latitude, b (deg)	*25.2229*
Position angle of μ in equatorial coordinates, ϕ (deg)...	*129.93(9)*
Position angle of μ in Galactic coordinates, ϕ (deg)....	*193.30(9)*
Pulse period, P (ms)	4.57013652403835(3)
Period derivative (observed), $\dot{P}_{\mathrm{obs}}$ (10^{-21})	8.5314(5)
Period derivative (intrinsic), $\dot{P}_{\mathrm{int}}$ (10^{-21})	*8.05(9)*
Frequency, ν (Hz)	218.811843965738(2)
First derivative of ν, $\dot\nu$ ($10^{-16}\,\mathrm{s}^{-2}$).....................	$-4.0847(2)$
Second derivative of ν, $\ddot\nu$ ($10^{-27}\,\mathrm{s}^{-3}$)	$-3.3(1)$
Third derivative of ν, $\dddot\nu$ ($10^{-35}\,\mathrm{s}^{-4}$)	$-4.6(7)$
Epoch (MJD [TDB])...................................	50576.0
Dispersion measure, DM (pc cm^{-3})	15.9966(2)[b]
First derivative of DM, dDM$/dt$ (pc cm^{-3} yr^{-1})	$-0.00016(5)$
Characteristic age, τ (yr).............................	*9.0(1)* $\times 10^9$
Surface magnetic field strength, B_0 (G)................	*2.00(11)* $\times 10^8$

[a]Figures in parentheses are uncertainties in the last digit quoted, and italicized
numbers represent quantities derived from fitted parameters.

[b]The quoted uncertainty is a formal estimate from the parameter fit and probably
understates the true uncertainty.

Table 3.3: Orbital parameters of PSR J1713+0747.[a]

Orbital period, P_b (days)	67.8251298713(7)
Projected semi-major axis, x (lt-s)	32.3424194(5)
First derivative of x, $\dot{x}$ (10^{-15})	6.3(4)
Eccentricity, e	0.000074942(2)
Epoch of periastron, T_0 (MJD [TDB])	50641.0773(9)
Longitude of periastron, ω (deg)	176.199(5)
Longitude of ascending node, Ω (deg)	*172(7)*
Sine of orbital inclination angle, $\sin i$	0.94(1)
Companion mass, m_2 ($M_\odot$)	$0.36^{+0.06}_{-0.05}$
Pulsar mass, m_1 ($M_\odot$)	*$1.85^{+0.41}_{-0.37}$*
Total mass, M ($M_\odot$)	*$2.21^{+0.41}_{-0.37}$*
Mass function, f_1 ($M_\odot$)	*0.0078962152(3)*
Rate of change of periastron, $\dot{\omega}$ ($10^{-4}\,\mathrm{deg\,yr^{-1}}$) . . .	5.2 ± 5.4[b]
Orbital period derivative, $\dot{P}_b$ (10^{-12})	-1.6 ± 1.1[b]
Eccentricity derivative, $\dot{e}$ ($10^{-18}\,\mathrm{s^{-1}}$)	1 ± 20[b]

[a]Figures in parentheses are uncertainties in the last digit quoted, and italicized numbers represent quantities derived from fitted parameters.

[b]These parameters were set equal to zero when fitting the others. The listed values were obtained by allowing these extra terms to vary one at a time.

3.3 Timing Model

Table 3.2 lists the astrometric and spin parameters. Because of alignment offsets between the template profiles (a different standard profile was employed for each backend and at each observing frequency), the computed value of DM most likely differs from the actual value, and therefore the formal uncertainty quoted for it is probably too small. The estimate of $d\mathrm{DM}/dt$, however, is unaffected by alignment bias. The fit included spin frequency, ν, and its first time derivative, $\dot{\nu}$. Unusually for an MSP, the second and third time derivatives were also needed fully to whiten the postfit residuals—a symptom of timing noise. Figure 3.2 illustrates the slowly varying trend by comparing postfit residuals without and with the extra derivatives.

Without them, the residuals show obvious wandering at the level of a few μs. For modeling the orbit, the DD model was used. Table 3.3 lists the binary parameters. Besides the five standard Keplerian parameters, $\{P_b, x, e, \omega, T_0\}$, three PK parameters, $\{r, s, \dot{x}\}$, were also needed to characterize the orbit. The fit for parallax is sensitive to how the solar system electron density is parameterized. Fitting for n_0 as a free parameter in equation 1.10, we find $n_0 = 11 \pm 5 \, \text{cm}^{-3}$. Before we boosted the statistical uncertainties of each TOA set in Table 3.1 (§ 1.5.5), the goodness-of-fit statistic of the original fit was high, $\chi^2/\nu = 11.9$, where $\nu = 228$ is the number of degrees of freedom. One possible cause is that the uncertainties of pre-averaging Mark IV points do not account for tiny artifacts in the data that result from quantizing the incoming signal with only two digital bits.

The tabulated parameters of PSR J1713+0747 constitute a substantial increase in precision over those published by Camilo, Foster, & Wolszczan (1994). Our results agree with theirs with the following exceptions. Those authors did not detect timing noise and so did not fit for derivatives of ν higher than the first. Nor did they obtain specific numbers for the sine of the orbital inclination angle or for the companion mass. Instead, they derived the limits $\sin i < 0.96$, consistent with our value, and $m_2 > 1.3 \, \text{M}_\odot$, significantly higher than our measurement.

3.4   Pulsar Astrometry and Spin-Down Behavior

3.4.1   Distance to the Pulsar

Pulsar distance measurements have numerous uses. Combined with the DM, distance can be used to infer the mean density of free electrons along the line of sight to a pulsar. In this way, the Galactic electron density can be mapped. Distance can be joined with the proper motion to calculate the spatial velocity of a pulsar. The distri-
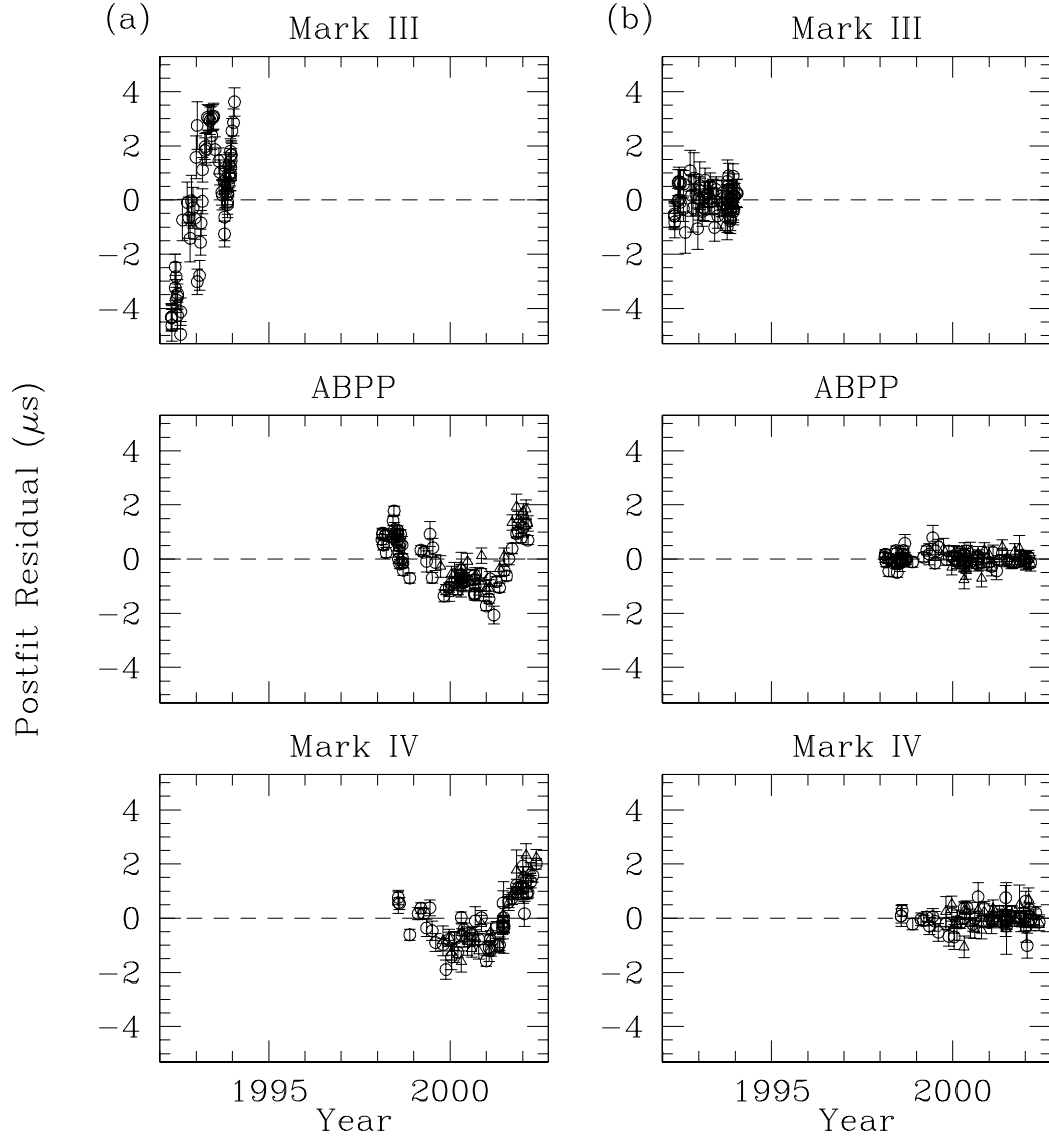
Figure 3.2: Postfit residuals of PSR J1713+0747 with and without timing noise. In (a), the noise is revealed by holding the second and third time derivatives of spin frequency at zero. In (b), the noise is removed by fixing the derivatives at their best-fit values in Table 3.3. The points are broken down by data-acquisition system. Error bars represent uncertainties on the TOAs. Circles and triangles indicate observing frequencies of 1410 and 2380 MHz, respectively.

bution of these across the pulsar population helps to uncover the degree of symmetry in supernova explosions. Finally, for a far-away pulsar, distance leads to more accurate determinations of $\dot{\nu}$ and $\dot{P}_b$, the measured values of which are substantially biased away from their true values by distance-dependent Doppler accelerations. A better number for $\dot{\nu}$ improves estimates of the age and surface magnetic field strength of a pulsar. A better number for $\dot{P}_b$ permits a more trustworthy assessment of the influence of gravitational radiation on a highly relativistic orbit.

The most direct way to measure a pulsar's distance is through parallax, the apparent back-and-forth movement of the object on the sky caused by Earth's annual motion around the Sun. If Earth's orbit is approximated as a circle, then parallax introduces a yearly delay into the timing data with amplitude

$$\Delta t_\pi = \frac{r^2 \cos^2 \beta}{2cd}, \tag{3.2}$$

where d is the pulsar distance, r is the Earth-sun distance, and β is the pulsar's ecliptic latitude. When detectable, parallax gives access to d. Unfortunately, the great distance to most pulsars renders parallax undetectable in all but a few MSPs with high timing precision. To date, the measurement has been achieved only for five pulsars. They are PSR J1713+0747 (Camilo, Foster, and Wolszczan 1994; this work), PSR J0437-4715 (van Straten *et al.* 2001), PSR J1744-1134 (Toscano *et al.* 1999a), PSR B1937+21, and PSR B1855+09 (Kaspi, Taylor, and Ryba 1994).

Figure 3.3 illustrates the parallax-induced delay in PSR J1713+0747's arrival times. We measure annual parallax to be

$$\pi = 0.73 \pm 0.06 \, \text{mas}, \tag{3.3}$$

leading to the distance estimate

$$d = \frac{1}{\pi} = 1.4 \pm 0.2 \, \text{kpc}. \tag{3.4}$$
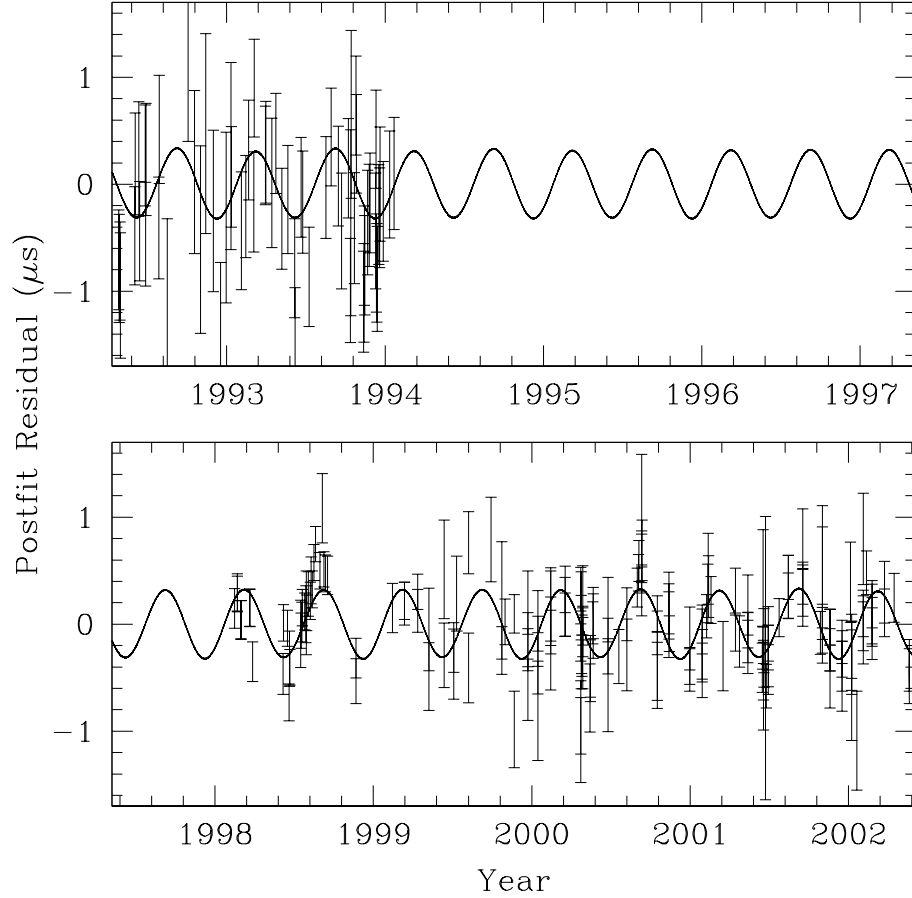
Figure 3.3: Heliocentric parallax in the timing residuals of PSR J1713+0747. Vertical lines represent individual TOAs and their uncertainties. The plot was created by removing parallax from the fit and fixing the rest of the timing parameters at their best-fit values. The solid curve is the best-fit solution of the parallax delay.

In principle, heliocentric parallax can also be measured through interferometry. The technique involves measuring a sequence of pulsar positions and charting the star's movement against the sky; proper motion appears as a linear rate of coordinate change while parallax is superimposed as an annual wobble. Successful results have come, for example, from Brisken *et al.* (2002), who used the Very Long Baseline Array (VLBA) to determine parallaxes with accuracies better than 400 μas, yielding

distance estimates with fractional uncertainties as small as 2%. The technique has not yet been applied to PSR J1713+0747.

It is worth mentioning that a second form of parallax arises from a combination of heliocentric parallax and a pulsar's orbital motion. It is potentially detectable as an apparent periodicity in the pulsar's projected semimajor axis,

$$x^{\mathrm{obs}}(t) = x^{\mathrm{int}} \left[1 + \frac{\cot i}{d} \mathbf{r}(t) \cdot \hat{\mathbf{\Omega}}' \right], \tag{3.5}$$

where i is the orbital inclination angle, $\mathbf{r}(t)$ is the position of the Earth with respect to the SSB, $\hat{\mathbf{\Omega}}'$ is a unit vector in the orbital plane that is perpendicular to the line of nodes, and $x^{\mathrm{obs}}(t)$ and x^{int} refer to the observed and the intrinsic values of the projected semimajor axis, respectively (van Straten *et al.* 2001; Kopeikin 1995). If detected and combined with independent estimates of i and $\hat{\mathbf{\Omega}}'$, this so-called annual-orbital parallax supplies another constraint on the distance. So far, the effect has been seen only in PSR J0437-4715 (van Straten *et al.* 2001), the closest and brightest MSP known, with a distance of $d = 0.139 \pm 0.003\,\mathrm{kpc}$. For PSR J1713+0747, the peak-to-peak amplitude of annual-orbital parallax is expected to be $\sim 1.5\,\mathrm{ns}$—too small to detect at current levels of observational precision [1].

3.4.2 Comparison With Dispersion-Measure Distance

As parallax measurements are seldom available, the most common method of estimating a pulsar's distance is to combine the DM with the average electron density in the direction of the star, $\langle n_e \rangle$:

$$d = \frac{\int_0^d n_e(z)\,dz}{\langle n_e \rangle} = \frac{\mathrm{DM}}{\langle n_e \rangle}. \tag{3.6}$$

---

[1]An analogous effect is the annual-orbital perturbation of the longitude of periastron, ω (Kopeikin 1995). Analysis since the completion of this thesis suggests that it is marginally detectable in PSR J1713+0747.

To find d in this way requires an estimate of $\langle n_e \rangle$. A model of electron density in wide use among pulsar astronomers is that of Taylor and Cordes (1993) (hereafter TC93). Drawing on optical and radio observations of HII regions, scattering measurements of Galactic and extra-Galactic radio sources, and independent estimates of pulsar distances and DMs, the TC93 model accommodates the spiral arms of the Galaxy as well as its general axisymmetric structure. For PSR J1713+0747, with DM $=$ $16.0 \, \mathrm{pc \, cm^{-3}}$, the model gives a distance of $d = 0.89 \, \mathrm{kpc}$, with lower and upper limits of $0.81 \, \mathrm{kpc}$ and $1.01 \, \mathrm{kpc}$. Errors in distances derived from the model are estimated to be $\sim 25\%$. Recently, Cordes and Lazio (2002) revised the TC93 model, building upon more plentiful data and improved statistical techniques. Their so-called NE2001 model yields a distance of $d = 0.90 \, \mathrm{kpc}$ for PSR J1713+0747, essentially the same as the TC93 result. For both the TC93 and the NE2001 schemes, the distance derived from DM is about 40% smaller than the one obtained from parallax.

Of the two methods of determining distance, parallax is more reliable than DM since it depends on straightforward geometry rather than a multi-parameter model of the Galactic distribution of free electrons. It is reasonable, then, to accept the parallax distance as the true distance to the pulsar. In that case, the mean free-electron density along the line of sight can be obtained from equation 3.6 by substituting the parallax distance for d. For PSR J1713+0747, this gives $\langle n_e \rangle = 0.011 \pm 0.001 \, \mathrm{cm^{-3}}$. According to this, the line-of-sight density assumed by the TC93 and the NE2001 models, $\langle n_e \rangle = 0.018 \, \mathrm{cm^{-3}}$, is too high by about 60%.

How to account for the discrepancy between the actual electron density and the one given by the models? The ISM has an essentially random character, and therefore some variance is to be expected in any quantitative description of it. Even so, systematic flaws in the models may also contribute to the discrepancy. For example, PSR J1713+0747 has a moderately high distance from the Galactic plane,

$z = d \sin b = 0.58 \pm 0.05 \,\mathrm{kpc}$, where $b = 24°\!.7$ is the star's Galactic latitude. It is possible that the TC93 and the NE2001 models are inadequately calibrated at high scale heights due to a relative paucity of independent distance measurements away from the Galactic plane. Interestingly, the TC93 model had been expected to un-derestimate, not overestimate, electron density in the direction of PSR 1713+0747. Cordes and Lazio (2002), for example, find that for pulsars at high Galactic latitudes the TC93 model generally returns densities that are too low, the opposite of what we find. Moreover, Toscano *et al.* (1999) claim that the TC93 model underestimates density not just for PSR J1713+0747 but also for several other pulsars in quadrant I of the Galaxy (the region $0° < l < 90°$, where l is Galactic longitude) and that have a Galactocentric distance projected into the plane of $\rho = d \cos b \sim 1 \,\mathrm{kpc}$. That these assumptions prove incorrect for PSR J1713+0747 implies that our improved estimate of $\langle n_e \rangle$ will be useful in constraining future models of free-electron density.

3.4.3   Proper Motion and Velocity

An MSP permits highly accurate measurements of its angular coordinates. Their rates of change—the proper motion—describe the star's linear movement on the sky, and can be measured with considerable accuracy. The third component of velocity, in the direction parallel to the line of sight, is needed for a complete characterization of a pulsar's motion. Unfortunately, it is inaccessible except in rare cases where spectral features of a pulsar's companion star can be fit for Doppler shift (for example, see Callanan, Garnavich, & Koester 1998). With optical magnitudes of $m_B > 27.2$, $m_V = 26.0 \pm 0.2$, and $m_I = 24.1 \pm 0.1$ (Lundgren, Foster, and Camilo 1996), the companion to PSR J1713+0747 is too faint for spectral observations. Thus, the description of the pulsar's space motion must remain two-dimensional.

Table 3.2 lists the components of PSR J1713+0747's proper motion, μ_α and μ_δ.

The magnitude of proper motion is

$$\mu = (\mu_\alpha^2 + \mu_\delta^2)^{1/2} = 6.082 \pm 0.009 \, \mathrm{mas \, yr}^{-1}. \tag{3.7}$$

Motion is also described in terms of the position angle, or the angle on the celestial sphere between the proper motion vector and the unit vector pointing toward the north pole. Under the convention that a positive angle runs north through east, the position angle of PSR J1713+0747 is

$$\phi = 193\overset{\circ}{.}30 \pm 0\overset{\circ}{.}09 \tag{3.8}$$

in Galactic coordinates, and

$$\phi = 129\overset{\circ}{.}93 \pm 0\overset{\circ}{.}09 \tag{3.9}$$

in equatorial coordinates.

Pulsars are among the faster stellar bodies in the Galaxy. Estimates for their mean birth velocity range over $250 - 300 \, \mathrm{km \, s}^{-1}$ (Hansen and Phinney 1997) and as high as $450 \, \mathrm{km \, s}^{-1}$ (Lyne and Lorimer 1994). These figures at least a factor of ten higher than the velocities of the progenitor stars. The high speeds are thought to result from the momentum "kick" given to pulsars in asymmetric supernova explosions (Shklovskii 1970). An isolated pulsar gains still more speed if the explosion disrupted the binary system to which it originally belonged (Gott, Gunn, and Ostriker 1970).

With a mean transverse velocity of $85 \pm 13 \, \mathrm{km \, s}^{-1}$, MSPs appear to be slower than unrecycled pulsars (Cordes and Chernoff 1997; Toscano *et al.* 1999b; Nice and Taylor 1995). One explanation: the impulses of the supernovas that create MSPs must necessarily be small enough to keep them bound to companion stars, otherwise they would never be spun up (Dewey and Cordes 1987). Moreover, the impulses are shared between the MSPs and their companions, so that MSPs receive less acceleration than do isolated pulsars. Hence, MSPs emerge from supernovas with sub-average

velocities. Another possibility is that unrecycled pulsars originate in type II super-novas (involving core collapse of a main sequence star) while MSPs may also form in type I supernovas (involving collapse of a white dwarf under accreted mass from a secondary). In terms of birth velocity, the difference is that type I supernovas expel less mass than type II supernovas, giving MSPs less of a momentum boost than regular pulsars (Tauris and Bailes 1996). Yet a third explanation for the observed lower speeds of MSPs is that pulsar searches may undercount distant MSPs—the very ones expected to have large transverse velocities—because the dispersive smearing brought on by their short pulse periods makes them harder to discover than unrecycled pulsars.

The transverse velocity of PSR J1713+0747,

$$V = \mu d = 40 \pm 3 \, \text{km}\,\text{s}^{-1}, \tag{3.10}$$

is roughly half the statistical mean of MSPs. Without the three-dimensional orientation of the velocity, it is hard to say why the pulsar should be moving somewhat slowly. Camilo, Foster, & Wolszcan (1994) interpret the Galactic position angle (eqn. 3.8) to mean that the system is returning to the plane. This is not necessarily true. With a sufficiently high radial velocity, the object could actually be moving away from the plane. Assuming it is true, however, the sluggish transverse velocity could imply that the pulsar has lately reached the apogee of one of its oscillations through the plane.

3.4.4   Kinematic Corrections to Spin Period Derivative

Because of Doppler accelerations, the observed spin-down rate of a pulsar, $\dot{P}_{\text{obs}}$, is biased away from its intrinsic value, $\dot{P}_{\text{int}}$. Damour & Taylor (1991) analyzed the effect for the orbital period derivative of PSR B1913+16, and their work applies equally well to spin period derivative. Following those authors, we write the first-order Doppler shift in spin period as

$$P_{\text{obs}} = P_{\text{int}} \left(1 + \frac{\mathbf{v} \cdot \hat{\mathbf{n}}}{c} \right), \tag{3.11}$$

in which $\mathbf{v}$ is the space velocity of the pulsar relative to the SSB and $\hat{\mathbf{n}}$ is the unit vector along the line of sight to the pulsar. For large space velocities, not only will the observed spin period differ from its intrinsic value by an amount potentially larger than the measurement uncertainty, but so might the orbital parameters. Without all three components of $\mathbf{v}$, however, intrinsic values are impossible to determine. Damour & Deruelle (1986) show that using observed rather than intrinsic parameters in the timing model is equivalent to rescaling units of time and mass by the Doppler factor.

Although Doppler shifts cannot be deduced from the timing parameters, Doppler accelerations can be. Taking the time derivative of equation 3.11 and separating transverse and line-of-sight terms gives an expression for the bias in the spin period derivative,

$$\left(\frac{\dot{P}}{P}\right)^{\text{bias}} \equiv \left(\frac{\dot{P}}{P}\right)^{\text{obs}} - \left(\frac{\dot{P}}{P}\right)^{\text{int}} = \frac{\mathbf{a} \cdot \hat{\mathbf{n}}}{c} + \frac{\mu^2 d}{c}, \tag{3.12}$$

in which $\mathbf{a}$ is the pulsar's acceleration. Also known as the Shklovkskii effect (Shklovskii 1970), the transverse term, $(\mu^2 d)/c$, describes the apparent change in period derivative from proper motion. The line-of-sight term, $(\mathbf{a} \cdot \hat{\mathbf{n}})/c$, can be subdivided into contributions from gravitational acceleration perpendicular to the Galactic plane and differential rotation within the plane. The bias may then be expressed as

$$\left(\frac{\dot{P}}{P}\right)^{\text{bias}} = -\frac{a_z \sin b}{c} - \frac{v_0^2 \cos b}{cR_0}\left[\cos l + \frac{\beta}{\sin^2 l + \beta^2}\right] + \mu^2 \frac{d}{c}, \tag{3.13}$$

where a_z is the vertical component of Galactic acceleration, R_0 is the Sun's distance from the Galactic center, v_0 is the Sun's circular speed around the Galactic center, b and l are the pulsar's Galactic latitude and longitude, and $\beta \equiv d/R_0 - \cos l$. We take $R_0 = 7.7 \pm 0.7\,\text{kpc}$ (Reid 1989), $v_0 = 222 \pm 20\,\text{km}\,\text{s}^{-1}$ (Kerr and Lynden-Bell 1986), and $d = 1.4 \pm 0.2\,\text{kpc}$ (eqn. 3.4). Calculating a_z requires a model of Galactic gravitational potential. Using that of Kuijken and Gilmore (1989), we write

$$\frac{a_z}{c} = 1.08 \times 10^{-19}\,\text{s}^{-1}\left[\frac{1.25z}{\sqrt{z^2 + (0.18)^2}} + 0.58\,z\right], \tag{3.14}$$

for which we take $z = d \sin b$ to be the Galactic scale height in kpc.

Multiplying the individual terms in equation 3.12 by the observed spin period, we obtain

$$(\dot{P})^{\text{int}} = (\dot{P})^{\text{obs}} - (\dot{P})^{\text{Shk}} - (\dot{P})^{\text{rot}} - (\dot{P})^{\text{vert}} = (8.05 \pm 0.09) \times 10^{-21}, \qquad (3.15)$$

in which $(\dot{P})^{\text{Shk}} = (0.58 \pm 0.05) \times 10^{-21}$ is the Shklovskii bias, with error dominated by uncertainty in d; $(\dot{P})^{\text{rot}} = (0.23 \pm 0.05) \times 10^{-21}$ is bias due to differential Galactic rotation, with error due mainly to uncertainties in R_0 and v_0; and $(\dot{P})^{\text{vert}} = (-0.33 \pm 0.05) \times 10^{-21}$ is bias from vertical acceleration, with error primarily from uncertainty in the surface mass density of the Galactic plane (a number implicit in eqn. 3.14). This result shows the observed spin period derivative to be about 6% higher than the actual value.

3.4.5   Pulsar Age and Surface Magnetic Field Strength

The age of PSR J1713+0747 can be estimated as

$$\tau = \frac{P}{2\dot{P}_{\text{int}}} = (9.0 \pm 0.1)\,\text{Gyr.} \qquad (3.16)$$

As explained in § 1.5.4, this probably exaggerates the age. Indeed, Hansen & Phinney (1998) obtain a lower estimate by identifying the cooling age of the white dwarf, $6.3\,\text{Gyr} < \tau < 6.8\,\text{Gyr}$, with the pulsar age. They assume that the MSP finished spinning up at the same time that the companion shrank within its Roche lobe and began losing heat. They obtain the white dwarf's age by combining a cooling model with optical measurements by Lundgren, Foster, and Camilo (1996).

From equation 1.36, the magnetic field strength of the pulsar is

$$B_0 = (2.00 \pm 0.011) \times 10^8\,\text{G}, \qquad (3.17)$$

a value typical for MSPs.

3.5   Orbital Motion and Mass Measurements

PSR J1713+0747 permits measurement not only of the five standard Keplerian parameters but also of two PK effects, Shapiro delay and the apparent rate of change of projected semimajor axis. By interpreting Shapiro delay within GR, we obtain the pulsar and companion masses, information crucial in evaluating theories of binary evolution.

3.5.1   Keplerian Mass Function

The Keplerian mass function of PSR J1713+0747 is

$$f_1(m_1, m_2, i) \equiv \frac{(m_2 \sin i)^3}{(m_1 + m_2)^2} \quad = \quad x^3 \left(\frac{2\pi}{P_b}\right)^2 \left(\frac{1}{T_\odot}\right)$$
$$= \quad 0.0078962152 \pm 0.000000003 \, \mathrm{M_\odot}. \quad (3.18)$$

Since it must be true that $\sin i \leq 1$, the expression can be rewritten to give an upper limit on m_1 in terms of m_2,

$$m_1 \leq m_2^{3/2} f_1^{-1/2} - m_2. \quad (3.19)$$

The limit is displayed as the striped region in Figure 3.6.

3.5.2   Shapiro Delay

In the orbital Shapiro delay, a pulse is retarded as it propagates through the gravitational potential well of the secondary. For a circular orbit, the formula for the time lag in GR is

$$\Delta t_s = -2\, m_2\, T_\odot \ln[1 - \sin i \sin(\phi - \phi_0)], \quad (3.20)$$

which is a re-expression of equation 1.16 in the limit $e \to 0$ and with the identities $r = T_\odot m_2$ and $s = \sin i$. The angle ϕ is the orbital phase in radians, and ϕ_0 is the
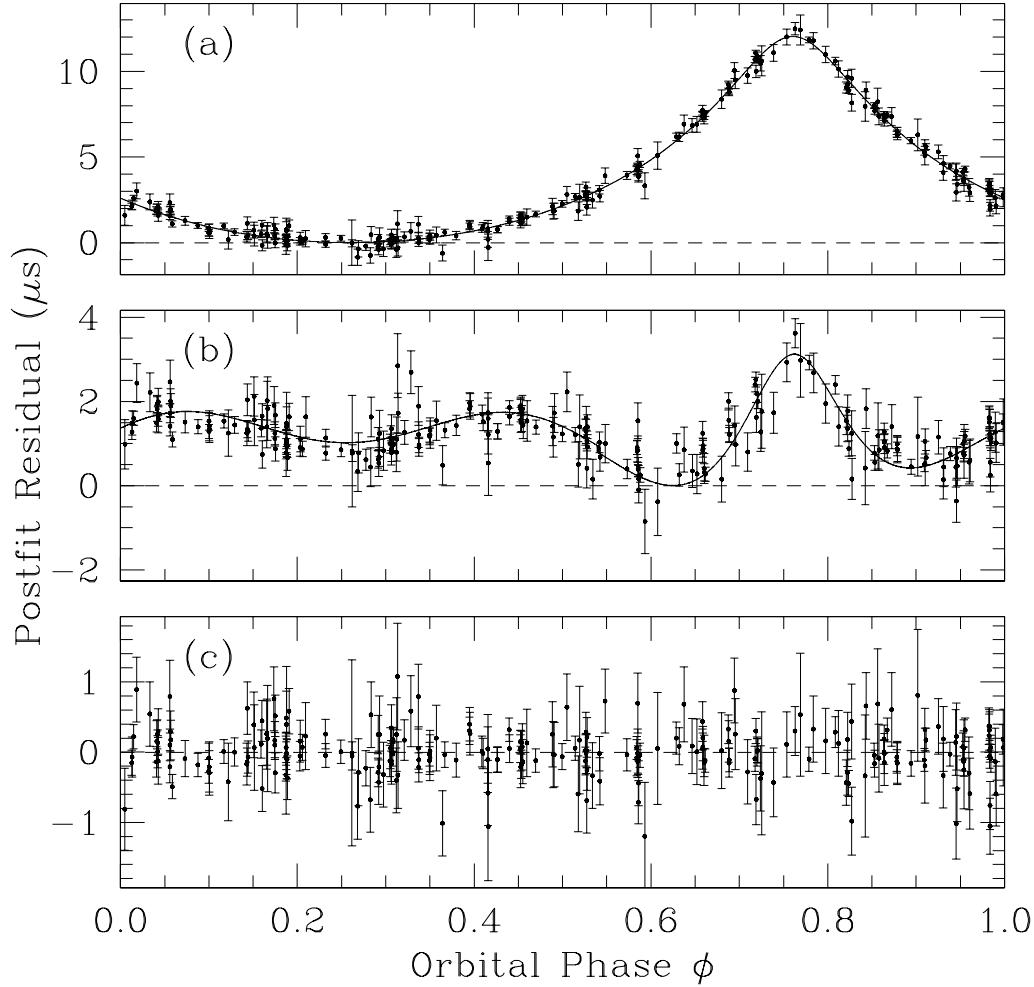
Figure 3.4: Shapiro delay in the timing residuals of PSR J1713+0747 plotted as a function of orbital period. In (a), the Shapiro terms are held at zero while the rest of the parameters are fixed at their best-fit values from Tables 3.2 and 3.3. The solid curve shows the delay predicted by GR (eqn. 3.20), given the best-fit values of m_2 and $\sin i$. In (b), the Shapiro terms are again held at zero but now the other parameters are permitted to vary. The solid curve represents the signal that remains in the residuals after attempting to fit the timing data to only a basic Keplerian model of the orbit plus $\dot{x}$. The complicated, non-zero pattern confirms that simple sinusoidal motion does not adequately describe the delay induced by orbital motion; further terms are needed. In (c), Shapiro delay is removed from the residuals by holding all terms at their best-fit values. The residuals in this panel are the same as those in Fig. 3.2b.

phase of the ascending node. For small inclination angles, the variation of Δt_s over an orbit is nearly sinusoidal, making it is indistinguishable from a minor increase in the projected orbital size, x. But for edge-on orbits ($i \approx 90°$) the variation becomes strongly peaked at $\phi - \phi_0 \approx \pi/2$, when the pulsar is behind the companion. This breaks the covariance with the Keplerian parameters and allows the Shapiro delay, and hence m_2 and $\sin i$, to be measured.

Figure 3.4 illustrates Shapiro delay in the prefit timing residuals. It also shows the improvement to the fit after the effect has been subtracted from the data. The parameters m_2 and $\sin i$ are difficult to ascertain even though the amplitude of the delay is significantly larger than the TOA uncertainties. This is because the terms are small as coefficients in equation 3.20 and because they are strongly covariant both with one another and with the other orbital parameters. As a result, contours of constant χ^2 are not elliptical, and the convenient assumption of symmetric uncertainties in linearized least-squares fitting does not automatically hold for m_2 and $\sin i$. To calculate confidence limits for the two parameters, we constructed the joint probability distribution function (PDF) of m_2 and $\cos i$ following the statistical procedure in Appendix B (as explained there, it is preferable to work with $\cos i$ rather than $\sin i$). Briefly, we performed parameter fits over a grid of m_2 and $\cos i$ values. At each grid point, we held the Shapiro terms fixed at the amounts predicted by GR while permitting all other parameters to vary. An analysis of χ^2 across the grid lets us map out the joint PDF.

Figure 3.5 displays the joint PDF of m_2 and $|\cos i|$. The absolute value brackets around $\cos i$ are necessary because the timing model cannot distinguish between a clockwise and a counterclockwise pulsar orbit—the orbital formulas, in other words, are degenerate between i and $180° - i$. The somewhat non-elliptical contours in Figure 3.5 confirm that the joint PDF is not strictly Gaussian near the best-fit solution.
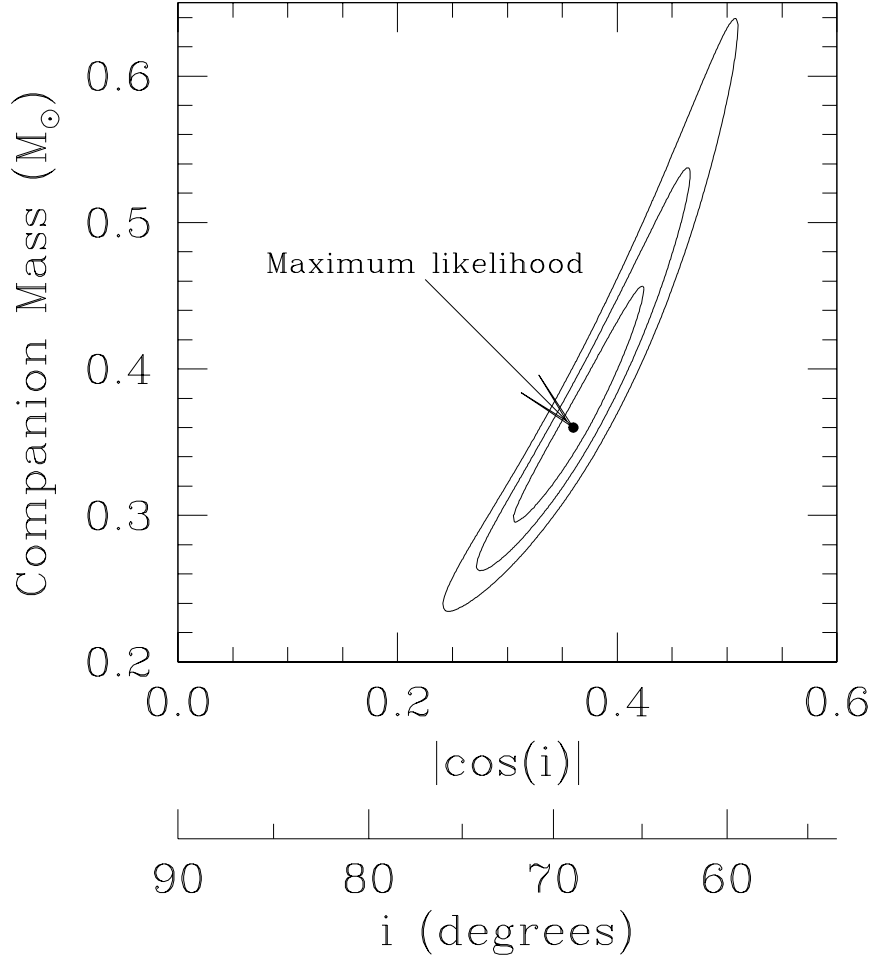
Figure 3.5: Joint PDF of m_2 and $|\cos i|$ for the PSR J1713+0747 system. The dot is the point of maximum likelihood. Contours around it represent confidence levels of 68%, 95%, and 99%.

Figure 3.6 shows the joint PDF of m_1 and m_2, obtained through a change of variables from $\cos i$ to m_1. It reveals that the timing data constrain the companion mass much more tightly than the pulsar mass. This fact is also apparent in the PDFs of the individual masses in Figures 3.7a-b. They yield the maximum-likelihood estimates

$$m_1 \;\; = \;\; 1.85^{+0.41}_{-0.37}\,\mathrm{M_\odot} \;\; (68\% \;\; \text{confidence})$$
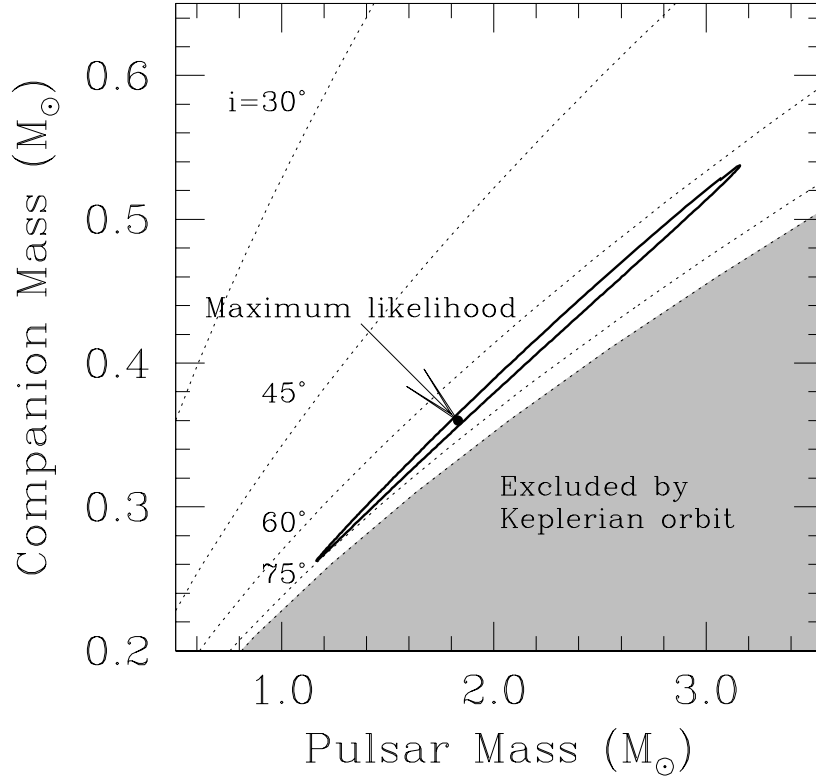
Figure 3.6: The $m_1 - m_2$ plane for the PSR J1713+0747 system. Acceptable values of the two masses lie outside the shaded region, which is off-limits by the requirement that $i \leq 90°$ (eq. 3.19). The narrow elliptical contour represents a confidence level of 95%. The dot within it is the maximum-likelihood point. Dashed lines show constant values of orbital inclination angle i.

$$= 1.85^{+0.97}_{-0.62} \, \mathrm{M_\odot} \ (95\% \ \text{confidence}) \qquad (3.21)$$

for the pulsar mass and

$$m_2 = 0.36^{+0.06}_{-0.05} \, \mathrm{M_\odot} \ (68\% \ \text{confidence})$$
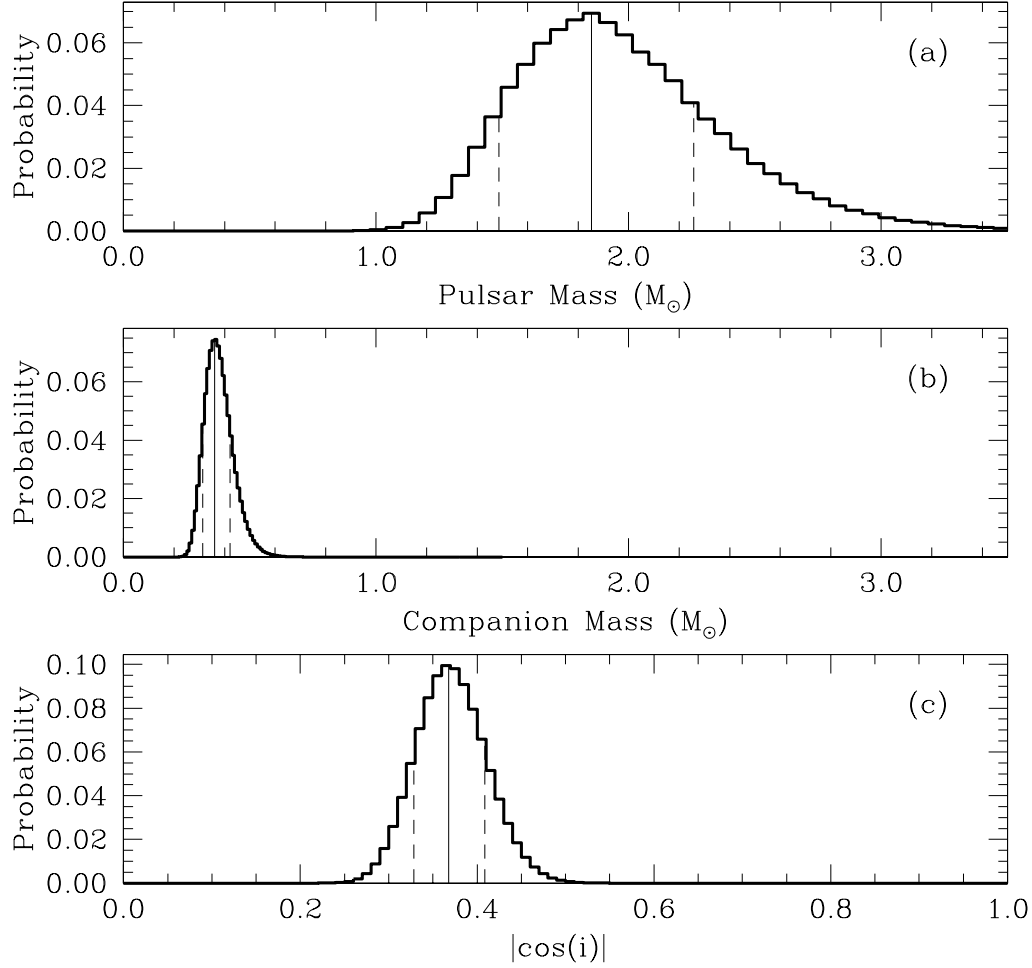
Figure 3.7: PDFs of (a) m_1, (b) m_2, and (c) $\cos i$ for the PSR J1713+0747 system. Solid vertical lines mark the maximum likelihood values. Dashed vertical lines delimit 68% confidence regions. They represent the shortest widths along the horizontal axes that both enclose the peaks and contain 68% of the area under the curves.

$$= 0.36^{+0.13}_{-0.09} \, M_\odot \; (95\% \text{ confidence}) \qquad (3.22)$$

for the companion mass. A similar analysis obtains the PDF of $|\cos i|$ in Figure 3.7c and the estimate

$$|\cos i| = 0.367^{+0.041}_{-0.039} \; (68\% \text{ confidence})$$

$$= \ 0.367^{+0.084}_{-0.075} \ (95\% \text{ confidence}). \tag{3.23}$$

3.5.3 $P_b - m_2$ Relation

Of the roughly 60 known binary pulsars, the majority are similar to PSR J1713+0747 in having wide $(1\,\text{d} < P_b < 1000\,\text{d})$ and nearly circular $(e < 0.025)$ orbits and low-mass $(m_2 < 0.45\,\text{M}_\odot)$ He white dwarf companions. The evolution of these systems is fairly well established (Phinney and Kulkarni 1994). The scenario begins with a red giant having mass $m_g \simeq 1\,\text{M}_\odot$ in orbit around a neutron star. At some point the giant overflows its Roche lobe, either because of its own nuclear evolution or because gravitational radiation or magnetic braking has shrunk the orbit. The giant enters a phase of stable mass transfer to the neutron star. During this period, angular momentum carried by the material spins up the pulsar to millisecond periods, and tidal torques circularize the orbit. Eventually, the envelope of the giant is exhausted. Mass transfer ceases, and the degenerate core of the giant remains as a white dwarf secondary.

For white dwarf-pulsar binaries formed in this way, there exists a mathematical formula connecting the orbital period to the companion mass (see Rappaport *et al.* 1995 and references therein). The relation is sometimes used to deduce the mass of the white dwarf in pulsar binaries where it cannot be obtained through timing (Thorsett and Chakrabarty 1999). In the case of PSR J1713+0747 and other systems for which timing does give the companion mass, the known values of P_b and m_2 provide a check on the relation.

Following Rappaport *et al.* (1995), the $P_b - m_2$ relation is derived as follows. Toward the end of mass transfer, the mass of the giant determines the Roche lobe radius, R_L, through

$$R_L \approx 0.46\, a \left(1 + \frac{m_1}{m_g}\right)^{1/3}, \tag{3.24}$$

where a is the orbital separation in solar radii. If the giant completely fills the Roche lobe, then $R_L \approx R_g$, where R_g is the radius of the giant. Moreover, when the envelope disappears at the end of mass transfer, $m_g \approx m_2$, where m_2 is the present-day white dwarf mass. These approximations combine with Kepler's third law to give

$$P_b \approx 20\,G^{-1/2}R_g^{3/2}m_2^{-1/2}. \tag{3.25}$$

The radius R_g depends on the mass of the core (which we take to be m_2), the chemical composition of the giant, and the convective mixing length of its atmosphere. By modeling stellar evolution for core masses in the range $0.15\,\mathrm{M_\odot} < m_2 < 1.15\,\mathrm{M_\odot}$, Rappaport *et al.* (1995) find the giant radius (in solar radii) to be well characterized by

$$R_g = R_0\frac{m_2^{9/2}}{(1+4m_2^4)} + 0.5, \tag{3.26}$$

in which R_0 is an adjustable parameter dependent on the chemical makeup of the giant:

$$R_0 = \begin{cases} 5500\,\mathrm{R_\odot} & \text{Pop. I} \\ 4950\,\mathrm{R_\odot} & \text{Pop. I+II} \\ 3300\,\mathrm{R_\odot} & \text{Pop. II.} \end{cases} \tag{3.27}$$

The median value (Pop. I+II) of R_0 gave Rappaport *et al.* (1995) the best fit across the set of different stellar masses and compositions considered. with it, equation 3.26 was found to be correct for all input data within a factor of 1.8. Inserting the formula for R_g into equation 3.25 yields the $P_b - m_2$ relation:

$$P_b = 0.374\left[\frac{R_0 m_2^{9/2}}{(1+4m_2^4)} + 0.5\right]^{3/2} m_2^{-1/2}, \tag{3.28}$$

with P_b in days and m_2 in solar masses. Upper and lower limits on P_b are obtained by multiplying and dividing the right hand side by a factor of 2.4, which represents the spread of 1.8 in R_g raised to a power of 3/2 (for Kepler's third law). For the PSR J1713+0747 system, with $P_b = 67.8\,\mathrm{d}$, the relation yields masses ranging from

$m_2 = 0.29\,\mathrm{M_\odot}$ for a Population I donor to $m_2 = 0.33\,\mathrm{M_\odot}$ for a Population II donor, with a median value (Pop. I+II) of $m_2 = 0.30\,\mathrm{M_\odot}$.

Podsiadlowski, Rappaport, & Pfahl (2002), performing more detailed calculations, find that the right hand side of equation 3.28 ought to be rescaled by a factor of ~ 0.65. The revised median mass of PSR J1713+0747's secondary is then $m_2 = 0.32\,\mathrm{M_\odot}$

Tauris & Savonije (1999) calculate stellar evolution using slightly different physics in their simulation code and derive an alternative $P_b - m_2$ relation:

$$m_2 = \left(\frac{P_b}{b}\right)^{1/a} + c, \tag{3.29}$$

where a, b, and c depend on the chemical composition of the secondary,

$$(a, b, c) = \begin{cases} 4.50 & 1.2 \times 10^5 & 0.120 & \text{Pop. I} \\ 4.75 & 1.1 \times 10^5 & 0.115 & \text{Pop. I+II} \\ 5.00 & 1.0 \times 10^5 & 0.110 & \text{Pop. II.} \end{cases} \tag{3.30}$$

The uncertainty in this model is a factor of ~ 1.4 around the median value. The formula is valid for binaries with He white dwarfs in the range $0.18\,\mathrm{M_\odot} \lesssim m_2 \lesssim 0.45\,\mathrm{M_\odot}$. For PSR J1713+0747's companion, it gives $m_2 = 0.31\,\mathrm{M_\odot}$ for a Population I donor, $m_2 = 0.34\,\mathrm{M_\odot}$ for a Population II donor, and a median value (Pop. I+II) of $m_2 = 0.33\,\mathrm{M_\odot}$.

Figure 3.8 compares the different versions of the $P_b - m_2$ relation with data for PSR J1713+0747 and two other MSPs whose He white dwarf companion masses have been measured through timing, PSR B1855+09, with $P_b = 12.3\,\mathrm{d}$ and $m_2 = 0.27 \pm 0.01\,\mathrm{M_\odot}$ (eqn. 6.2), and PSR J0437-4715, with $P_b = 5.7\,\mathrm{d}$ and $m_2 = 0.236 \pm 0.001\,\mathrm{M_\odot}$ (van Straten *et al.* 2001). According to the figure, the model of Tauris & Savonije (1999) (eqn. 3.29) corresponds best with the empirical results, and it does so with the smallest uncertainty range. The model of Rappaport *et al.* (1995) (eq. 3.28) returns orbital periods somewhat too high for a given secondary mass. The rescaling of that model recommended by Podsiadlowski *et al.* (2002) is a clear improvement.
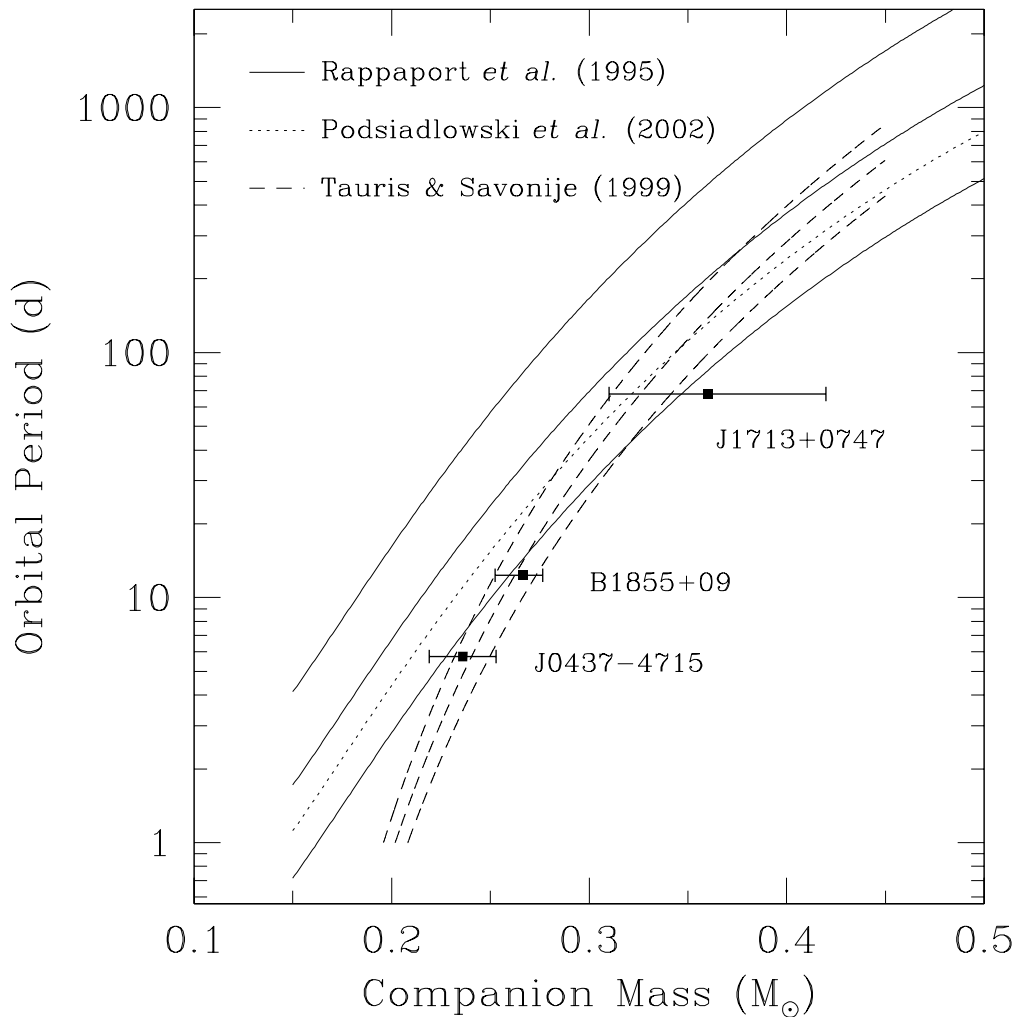
Figure 3.8: $P_b - m_2$ relations and companion masses of three MSPs. Each model is marked by a triplet of curves: the center one shows the median (Pop. I+II) relation and the two outside ones represent uncertainty limits. For the Podsiadlowski *et al.* (2002) model, the uncertainties correspond to the boundaries of the lower "lane" of the Rappaport *et al.* (1995) distribution.

3.5.4 Evidence for Accretion onto the Pulsar

The general formation mechanism for low-mass binary pulsars described in § 3.5.3 does not specify how much mass is accreted onto the neutron star. It is known that a neutron star must accept at least $\sim 0.1 \, \mathrm{M_\odot}$ from its giant-phase companion in order to attain millisecond periods (Taam and van den Heuvel 1986). But whether additional mass from the giant's envelope reaches the pulsar is an open question. Some authors (e.g., van den Heuvel & Bitzaraki 1995) posit that the transfer of as much as $\sim 0.7 \, \mathrm{M_\odot}$ is needed to reduce magnetic fields to the weak strengths observed in MSPs. On the other hand, Thorsett & Chakrabarty (1999) find the measured masses of pulsars orbiting both white dwarfs and other neutron stars to be consistent with a narrow Gaussian distribution, $m_1 = 1.35 \pm 0.04 \, \mathrm{M_\odot}$. Since pulsars in double neutron star binaries are not expected to accrete much mass, the small spread suggests that the same is true of low-mass binary pulsars. Within its error bars, our measurement of PSR J1713+0747's mass (eq. 3.21) is just slightly higher then that population mean found by Thorsett & Chakrabarty (1999), and so it provides only weak evidence of accretion.

3.5.5 Interpretation of $\dot{x}$

The rate of change of the projected semimajor axis of PSR J1713+0747 is measured to be

$$\dot{x} = \frac{d}{dt}\left(\frac{a_1 \sin i}{c}\right) = (6.3 \pm 0.4) \times 10^{-15}. \tag{3.31}$$

In principle, nonzero $\dot{x}$ could result from variation in the orbital size, a_1, or in the inclination angle, i, or both. However, change in a_1 can be ruled out as too small to cause the observed effect. GR, for example, predicts that the orbit of two point

masses must shrink due to emission of gravitational radiation at a rate

$$\dot{a}_1 = -\frac{64}{5}T_\odot^3\frac{m_1 m_2^5}{(m_1+m_2)^3}\frac{1}{a_1^3}\frac{1}{(1-e^2)^{7/2}}\left(1+\frac{73}{24}e^2+\frac{37}{96}e^4\right) \qquad (3.32)$$

(Peters 1964), where a_1 is in light-seconds. For the PSR J1713+0747 system, this amounts to $\dot{a}_1 = -3.8 \times 10^{-23}$, a full eight orders of magnitude below the observed value of $\dot{x}$. More generally, for any astrophysical process that could conceivably change the size of the orbit (such as mass transfer between the stars), $|\dot{a}_1/a_1|$ will be of the same order of magnitude as $|\dot{P}_b/P_b|$. Interpreting the observed value of $\dot{P}_b$ plus its uncertainty as an upper limit, $|\dot{P}_b| < 2.7 \times 10^{-12}$, we find that $|\dot{P}_b/P_b| < 1.4 \times 10^{-11}\,\mathrm{yr}^{-1}$, which is two orders of magnitude smaller than the observed $|\dot{x}/x| = 6.1 \times 10^{-9}\,\mathrm{yr}^{-1}$. We conclude that variation in orbital dimension is not behind the observed value of $\dot{x}$.

The nonzero $\dot{x}$ must therefore result from variation in i. Several authors have discussed how a_1 can remain fixed and yet x change because of relative motion between the binary and the observer (Kopeikin 1996; Nice, Splaver, and Stairs 2001). Following Nice *et al.* (2001), we write the effect as

$$\dot{x} = -1.54 \times 10^{-16}\,x\mu\cot i\sin\left(\phi - \Omega\right) \qquad (3.33)$$

(this equation restores a minus sign missing from eqn. 3 in Nice *et al.* 2001), where the numerical constant makes $\dot{x}$ dimensionless if μ is in $\mathrm{mas\,yr}^{-1}$ and x is in lt-s. Both ϕ, the position angle of proper motion (eqn. 3.9), and Ω, the position angle of the ascending node, are in equatorial coordinates, and both are defined so that a positive angle runs north through east[2] (see Fig. 1.3 for an illustration of orbital geometry). If equation 3.33 is taken as the source of measured $\dot{x}$ for PSR J1713+0747, then the expression can be solved for Ω. Because of ambiguities associated with both i and

---

[2]This convention differs from that of Kopeikin (1996), who takes a positive angle to go north through west.

the inverse sine function, the solution is actually fourfold degenerate:

$$\Omega = \begin{cases} 95° \pm 3° \quad \text{or} \quad 340° \pm 3° \quad \text{if } \cos i < 0 \\ 160° \pm 3° \quad \text{or} \quad 277° \pm 3° \quad \text{if } \cos i > 0. \end{cases} \tag{3.34}$$

Related to $\dot{x}$ is a potentially measureable rate of change in the longitude of periastron. Again, the effect is an apparent one, resulting from proper motion of the binary and not from relativistic orbital precession (Kopeikin 1996). The formula is

$$\dot{\omega} = -2.78 \times 10^{-7} \mu \csc i \cos(\phi - \Omega) \, \text{deg yr}^{-1}. \tag{3.35}$$

In PSR J1713+0747, the effect should be $|\dot{\omega}| \sim 1.5 \times 10^{-6} \, \text{deg yr}^{-1}$. On the one hand, this is two orders of magnitude smaller than the upper limit currently measured, $\dot{\omega} < 5 \times 10^{-4} \, \text{deg yr}^{-1}$. On the other hand, it is three orders of magnitude larger than the predicted rate of apsidal motion due to GR, $\dot{\omega}_{\text{GR}} \sim 2.4 \times 10^{-9} \, \text{deg yr}^{-1}$.

3.6   Timing Noise

Figure 3.2 shows that the pulse arrival times of PSR J1713+0747 are contaminated by an unmodeled signal that significantly exceeds measurement errors. While such low-frequency noise is not uncommon in unrecycled pulsars, it has been seen in only one other MSP, PSR B1937+21 (Kaspi, Taylor, and Ryba 1994), and for this reason it merits close study. In this section, we begin analysis of the phenomenon by ruling out two possible causes of the noise, DM variations and secular changes in the pulse profile. We also give a statistical characterization of the signal that allows comparison with similar phenomena in other pulsars. Future work by Lommen *et al.* (2003) will examine other potential causes of the timing noise, including the hypothesized GWB.
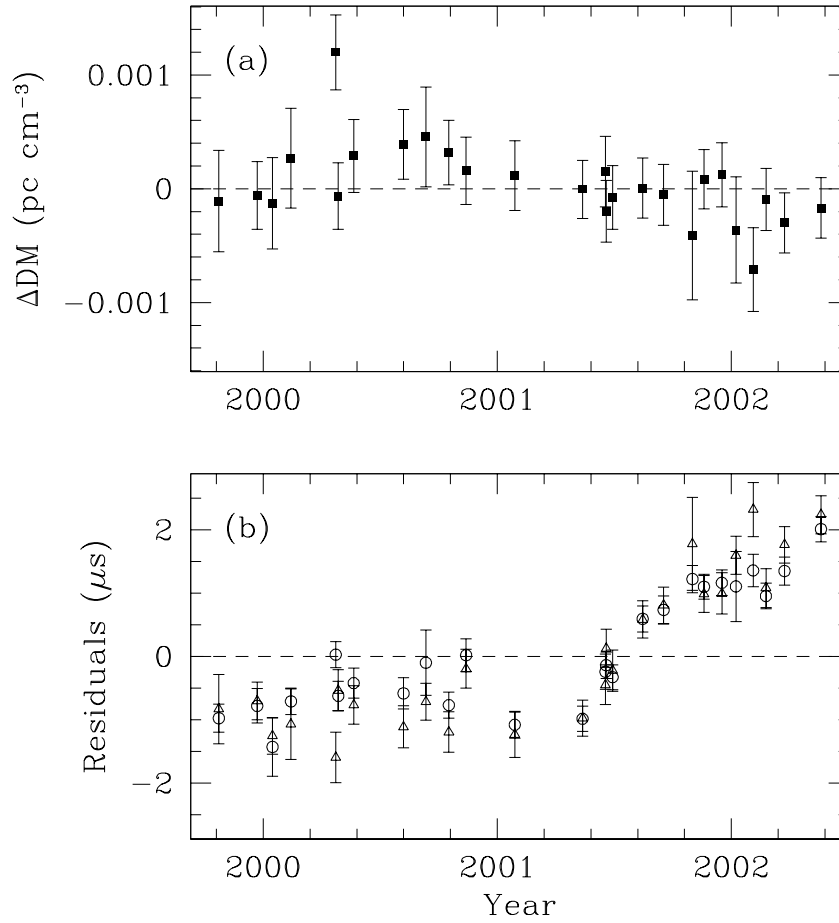
Figure 3.9: DM variations of PSR J1713+0747. In (a), values of $\Delta DM = DM - 15.9966$ are plotted as a function of time. The sequence is consistent with no long-term change in DM. Panel (b) shows the postfit timing residuals from which the points in (a) were computed. Circles and triangles signify TOAs taken at 1410 MHz, and 2380 MHz, respectively. The upward trend is part of the timing noise featured in Fig. 3.2.

3.6.1   DM Variations Not the Culprit

The DM of a pulsar can fluctuate if the column density of free electrons along the line of sight changes over time. If this happens, a timing solution that erroneously treats the DM as constant will then fail to account for shifts in dispersive delay, and

the postfit residuals will exhibit drifts. Such trends are witnessed, for example, in the residuals of the MSPs PSR J0621+1002 (§ 4.3.1) and PSR B1937+21 (Kaspi, Taylor, & Ryba 1994).

To see whether such trends might be causing the timing noise in PSR J1713+0747, we plot DM variations as a function of time in Figure 3.9. The points were calculated from Mark IV timing data on days when the pulsar was observed at both 1410 MHz and 2380 MHz. On each day, the deviation of the DM from its best-fit value in Table 3.2 was computed through

$$\Delta\mathrm{DM} = (2.410 \times 10^{-4}\,\mathrm{pc\,cm}^{-3})(r_2 - r_1)\left(\frac{1}{f_2^2} - \frac{1}{f_1^2}\right)^{-1}, \qquad (3.36)$$

where r_1 and r_2 are postfit residuals in μs for TOAs obtained at solar system barycentric frequencies f_1 and f_2 in MHz. The figure reveals that the DM does not change in any significant way. The points are consistent with a stationary DM. Certainly, they contain no clear pattern corresponding to the timing noise in the residuals from which they were computed, shown in Figure 3.9b. Hence, we conclude that DM variations are not a factor in the timing noise.

In theory, other interstellar propagation effects can add noise to TOAs. For example, changes in the refractive angle at which pulses arrive at Earth can produce stochastic delays in arrival times in two ways: by shifting the apparent location of the pulsar on the sky ("image wander") and by altering the path-length traversed by the pulses (Foster and Cordes 1990). The first type of delay has an f^{-2} dependence while the second scales as f^{-4}. These mechanisms, and all others that depend on frequency, can be ruled out as sources of timing noise for the same reason that DM variations are excluded: the arrival times show no significant lag between different observing frequencies.
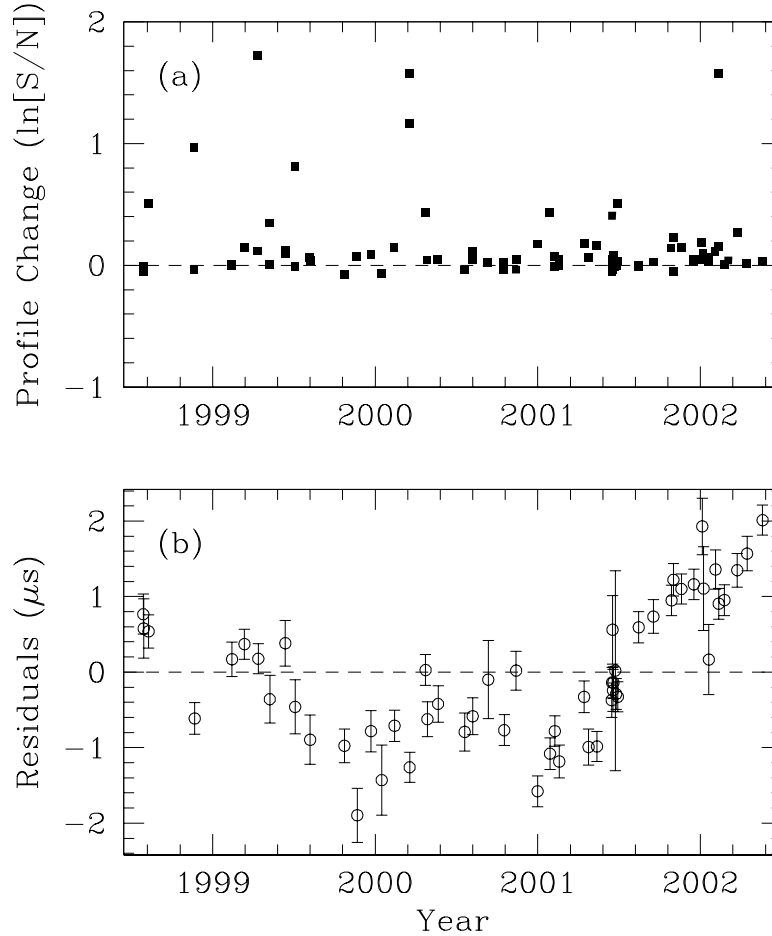
Figure 3.10: Profile variations of PSR J1713+0747. Panel (a) plots a statistic measuring change in the integrated pulse profile versus time. The statistic quantifies variation in daily profile with respect to a reference profile from a single epoch (10 February 2002). Values near zero indicate similarity between the integrated profile and the reference profile (and hence no change). Values away from zero imply discrepancy. The plot confirms that the integrated profile is essentially changeless over timescales of ~ 1 year. In particular, the points show no correlation with the drifts in the postfit timing residuals, shown in panel (b). The trends in the residuals are part of the timing noise featured in Fig. 3.2.

3.6.2 Profile Changes Not the Culprit

An assumption underlying pulsar timing is that the integrated pulse profiles are stationary. In computing TOAs, this is what permits comparison of integrated profiles from different epochs. If the integrated profiles were not in fact fixed, then unaccounted-for shape changes would produce systematic errors in the measured arrival times. In this section, we verify that an unstable profile is not a factor in the timing noise of PSR J1713+0747.

The timescale of the trends in Figure 3.2a—by which we mean the period between zero crossings—is roughly a year. We emphasize that it is not known whether there even exists a profile-altering mechanism that acts on this timescale. In other pulsars, the few recorded instances of long-term profile changes (i.e. occurring over more than ~ 1 minute) have timescales that are orders of magnitude longer or shorter than a year. Longer than a year, geodetic precession alters the profile of PSR B1913+16 by reorienting the pulsar spin axis at a rate of $1°2 \, \mathrm{yr}^{-1}$ (Weisberg and Taylor 2002). The same relativistic effect in PSR J1713+0747 is expected to proceed at the undetectably slow rate of $3°1 \times 10^{-5} \, \mathrm{yr}^{-1}$. Shorter than a year, the apparently emission-related stochastic profile changes seen in the MSPs PSR B1821-24 (Backer and Sallmen 1997) and PSR J1022+2001 (Kramer *et al.* 1999b) take place over over $\sim 1 \, \mathrm{hr}$. No profile changes have been observed on timescales intermediate to these. Nevertheless, it is worthwhile to hunt for them in PSR J1713+0747 because the hypothesis of profile stability is less well tested for MSPs than it is for unrecycled pulsars.

We searched for profile changes using the following procedure. First, we constructed a separate integrated profile from each scan (typically 29 minutes long) taken at $1410 \, \mathrm{MHz}$ by the Mark IV observing system. One particularly strong profile (from 10 February 2002) was selected as a reference against which the other profiles were compared. To carry out the comparison, we made use of the fact that the other

profiles can be viewed as versions of the reference profile that have been transformed by a DC bias, a multiplicative scale factor, a time shift, and background noise. Mathematically, the other profiles, $p_i(t)$, are related to the reference profile, $r(t)$, through the transformation

$$p_i(t) = a_i + b_i r(t - \tau_i) + n_i(t), \tag{3.37}$$

where a_i, b_i, and τ_i are constants, $n_i(t)$ represents additive noise, and $0 \leq t \leq P$, with P the pulse period. Following Taylor (1992), we obtained the three constants through least-squares fitting in the Fourier domain. With them, we formed a resized and time-shifted version of each profile,

$$\tilde{p}_i(t) = \frac{[p_i(t + \tau_i) - a_i]}{b_i}, \tag{3.38}$$

that is the closest possible match to the reference profile. If PSR J1713+0747 experienced no changes in its integrated profile, then the difference between each rescaled profile and the reference profile, $d_i(t) = \tilde{p}_i(t) - r(t)$, would be pure noise. But if the integrated profile did vary over time, then some of the transformed profiles should be dissimilar to the reference profile. In those cases, $d_i(t)$ would contain features distinguishable from noise. As a statistic to measure profile change, we calculated the signal-to-noise ratio of each difference profile, taking "signal" and "noise" to be the rms values of those segments of the profile where the pulse is normally "on" and "off", respectively.

Figure 3.10a plots the natural logarithm of the signal-to-noise ratio as a function of time. A value near zero implies similarity between an integrated profile and the reference profile. A value away from zero indicates discrepancy. The plot reveals that the profile is essentially changeless over timescales of ~ 1 year. While the occasional large value hints that the profile may change over a timescales on the order of the spacing between data points, ~ 30 days, the lack of coherence among these points, together with the preponderance of points near zero, confirm that the integrated profile

is essentially stable over the long-term. There is no correlation between the points and the trends in the postfit residuals of TOAs made from the same raw data as the profiles, shown in Figure 3.10b. It follows that the timing noise in PSR J1713+0474 is not the fault of profile changes.

3.6.3   Statistical Description of Timing Noise

In unrecycled pulsars, the amplitude of timing noise is found to be weakly correlated with the time derivative of spin period, which in turn is a proxy for age, since younger pulsars tend to have larger values of $\dot{P}$ (Cordes and Downs 1985). Although the exact cause of timing noise in regular pulsars is unknown, it is generally understood to come from rotational instability that most likely arises from structural activity within the newly formed neutron stars.

In a timing analysis of slow pulsars, Arzoumanian *et al.* (1993) developed a statistic to rate the magnitude of timing noise. They defined it as

$$\Delta(t) \equiv \log_{10}\left(\frac{1}{6\nu}|\ddot{\nu}|t^3\right),$$ (3.39)

where t, the length of the data set over which the parameters ν and $\ddot{\nu}$ are fit, is taken by convention to be 10^8 s, in which case the statistic is called "Δ_8". The idea is that because $\ddot{\nu}$ is undetectably small for most pulsars under the traditional spin-down mechanism, any measured non-zero value indicates physical effects outside the timing model. Arzoumanian *et al.* (1993) found the relation

$$\Delta_8 = 6.6 + 0.6 \log \dot{P}$$ (3.40)

to describe the magnitude of timing noise of most pulsars. For PSR J1713+0747, the value of the stability parameter defined in equation 3.39, $\Delta_8 = -5.6$, accords well with the value derived from the empirical relation in equation 3.40, $\Delta_8 = -5.5$. Kaspi, Taylor, & Ryba (1994) reported similar agreement for PSR B1937+21. The

fact that two MSPs obey a relation calibrated for ordinary pulsars hints strongly that timing noise is caused by rotational irregularity in both fast- and slow-spinning pulsars alike.

A more comprehensive picture of timing noise comes from analyzing it with a statistical technique similar to that used by the high-precision timekeeping community to gauge atomic-clock stability. The regularity of an atomic clock is studied by fitting out a constant frequency bias from the sequence of ticks and conducting a spectral analysis on any drifts remaining in the signal. In the presence of red noise, the standard technique for measuring a power spectrum, Fourier analysis, is ineffective because of spectral leakage between frequency bins. It is customary to use instead the Allan variance, a time-domain statistic that looks at second differences of frequency drift. By itself, the Allan variance is inappropriate for pulsar timing residuals because the spin-down model already fits out a frequency drift, $\dot{\nu}$. But Taylor (1991) generalized the Allan variance into a new statistic, σ_z, that focuses on third differences in frequency drift, or equivalently in the pulsar timing model, $\dddot{\nu}$. Matsakis, Taylor, & Eubanks (1997) give the following procedure for computing this statistic.

1. Fit the TOAs to a timing model that goes no higher in frequency derivative than $\dot{\nu}$.

2. Order the postfit residuals chronologically by TOA.

3. Divide the residuals into intervals of length τ, and over each interval perform a least-squares fit to a third-order polynomial,

$$R(t) = c_0 + c_1(t - t_0) + c_2(t - t_0)^2 + c_3(t - t_0)^3, \qquad (3.41)$$

where t is the TOA and t_0 is a reference epoch chosen from within the interval. The first three polynomial coefficients contain no new information because the timing model, running through $\dot{\nu}$, has already fit out terms of this order. But

the cubic coefficient measures the magnitude of events in the residuals on the timescale τ.

4. Average the squares of the cubic coefficients over all available non-overlapping intervals of length τ, using the formal errors in the c_3's as weights. The unitless statistic

$$\sigma_z(\tau) \equiv \frac{\tau^2}{2\sqrt{5}} \left\langle c_3^2 \right\rangle^{1/2} \tag{3.42}$$

then provides an estimate of spectral power in the residuals at a frequency of $f \sim 1/\tau$.

Assuming that the initial value of τ was the span of the entire data set, steps $3 - 4$ are to be repeated over intervals of $\tau/2$, $\tau/2^2$, $\tau/2^3$, and so forth, until the intervals contain too few residuals to fit a third-order polynomial. Significantly for the residuals of PSR J1713+0747, which contain a gap of roughly four years (see Fig. 3.2), intervals of duration τ in which the time difference between latest and earliest TOA is less than $\tau/\sqrt{2}$ are to be ignored in step 3. This is to ensure that non-uniform sampling does not skew the statistic.

Figure 3.11 shows σ_z calculated for PSR J1713+0747. The error bars, which give 68% confidence limits, were computed from a prescription given by Matsakis, Taylor, & Eubanks (1997). The initial downward trend, with slope of roughly $-3/2$, indicates that the residuals have the character of uncorrelated measurement error over timescales up to about a year. At higher values of τ, the upward trend in the last three points signals the presence of a low-frequency noise source. Again, this behavior is similar to that of PSR B1937+21 (see Fig. 9 in Kaspi *et al.* 1994). As with that pulsar, PSR J1713+0747's timing noise makes it inferior to the best atomic clocks as a long-term frequency standard (see Fig. 2 in Matsakis *et al.* 1997 for a comparison of σ_z calculated from PSR B1937+21, PSR B1855+09, and three high-quality terrestrial timescales).
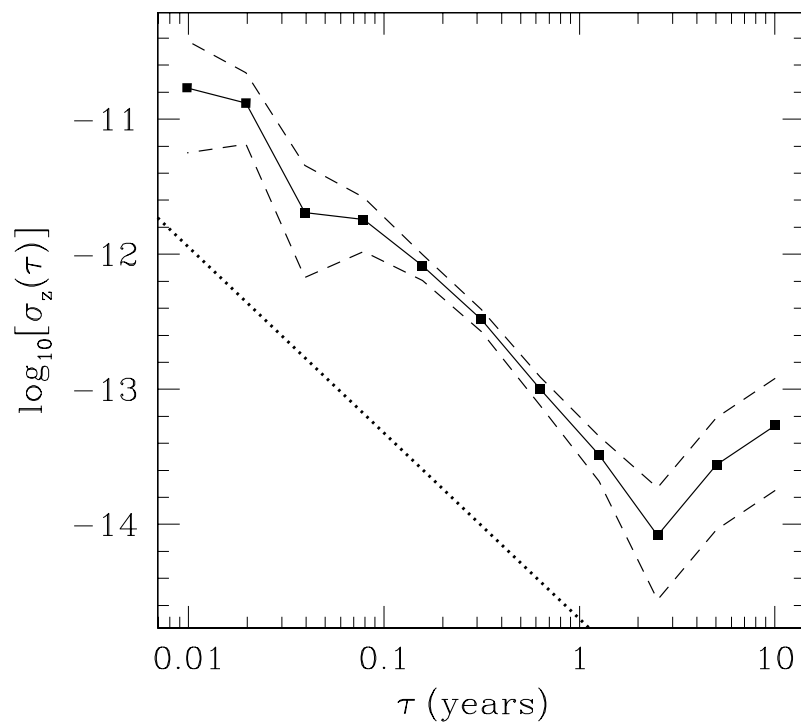
Figure 3.11: Fractional timing stability, $\sigma_z(\tau)$, of PSR J1713+0747, shown in square points. Dashed lines above and below the solid line enclose 68% confidence limits. For comparison, the dotted line has slope of $-3/2$, the expected result for timing residuals dominated by uncorrelated measurement error. The turn-up in the square points at $\tau \gtrsim 1\,\mathrm{yr}$ reveals that some low-frequency noise source is present in the timing data.

Chapter 4

PSR J0621+1002: Probing System Masses Through Relativistic Apsidal Motion[1]

4.1 Introduction

Recent pulsar searches have uncovered a new class of binary pulsars. While most MSPs are in nearly circular orbits with low-mass He white dwarfs, comprising the class of so-called low-mass binary pulsars (LMBPs), the new category of systems, the intermediate-mass binary pulsars (IMBPs), have heavier companions with masses above $0.45\,M_\odot$. Since helium flash occurs at a core mass of $0.45\,M_\odot$, the stars must be CO or ONeMg white dwarfs. About eight IMBPs are currently known. Observationally, they are distinguished by high Keplerian mass functions ($f_1 > 0.015\,M_\odot$); by moderately spun-up pulse periods ($10\,\mathrm{ms} < P < 200\,\mathrm{ms}$); and by orbital eccentricities that are small ($e < 10^{-2}$) but nevertheless somewhat higher than those of LMBPs

---

[1]The results in this chapter appeared in *The Astrophysical Journal* (Splaver *et al.* 2002).

(Camilo *et al.* 1996; Camilo *et al.* 2001; Edwards and Bailes 2001b).

This chapter reports on timing measurements of PSR J0621+1002, an IMBP with a 28.8-ms spin period in an 8.3-day orbit. The main goal of our observations was to determine the pulsar and companion masses through measurement of PK orbital parameters, particularly the rate of apsidal motion. Detecting apsidal motion in white dwarf-pulsar binaries is challenging because their often extremely small eccentricities—values of 10^{-5} are typical—make measurement of the angle of periastron, and hence of periastron advance, difficult. A comparatively high eccentricity—still only $e = 0.0025$—made the detection feasible for PSR J0621+1002.

Mass measurements in white dwarf-pulsar systems can be used to constrain theories of binary evolution. The LMBPs and the IMBPs share roughly similar histories. They both originate when a giant star transfers mass onto a neutron star companion, resulting in a spun-up MSP and a white dwarf. The histories of LMBPs and IMBPs differ, however, in the details of mass exchange. For LMBPs, it is a stable process that occurs when the giant swells past its Roche lobe (Phinney and Kulkarni 1994). For IMBPs, it is thought to be an unstable transfer that operates via common envelope evolution (van den Heuvel 1994) or super-Eddington accretion (Taam, King, & Ritter 2000). Other pulsar binaries, such as double neutron star systems, evolve in still other ways. One way to test scenarios of binary evolution is by comparing the masses of neutron stars in different classes of binary systems to infer differences in amounts of mass transferred (see Thorsett & Chakrabarty 1999 for a review of pulsar mass measurements).

The first year of timing observations of PSR J0621+1002 was discussed in Camilo et al. (1996), which reported the pulsar's Keplerian orbital elements, position, and spin period. With five additional years of timing data, we have measured the apsidal motion, spin-down rate, and proper motion of the pulsar, and we have derived signif-

Table 4.1: Summary of Observations of PSR J0621+1002

Observatory	Dates	Frequency (MHz)	Bandwidth (MHz)	Number of TOAs	Typical Integration (min)	RMS Residual[a] (μs)
Arecibo	1997.9–2001.5	430	5	103	29	2.6
	1999.4–2001.5	1410	10	24	29	3.2
Green Bank	1995.2–1999.0	370	40	48	50	17
	1995.2–1999.5	575	40	49	40	13
	1995.2–1999.5	800	40	39	40	19
Jodrell Bank	1996.2–1997.7	410	8	12	30	21
	1995.7–1999.8	606	8	298	30	12
	1995.7–1997.8	1410	32	78	30	24
	1997.8–1999.3	1380	96	79	30	16
	1999.7–2001.2	1396	64	50	30	19

[a]Values from Arecibo and Green Bank incorporate the effect of averaging TOAs.

icant constraints on Shapiro delay. We have also found sharp variations in the DM, which we use to analyze turbulence in the ISM in the direction of PSR J0621+1002.

4.2   Observations

Radio telescopes at Arecibo, Green Bank, and Jodrell Bank recorded TOAs from PSR J0621+1002 on 529 separate days between 1995 March 18 and 2001 July 1. Table 4.1 summarizes the observations. The data comprise (1) three nine-day campaigns at Arecibo in 1999 May, 2000 May, and 2001 June, each covering a full pulsar orbit at two radio frequencies; (2) a handful of additional Arecibo measurements taken monthly between 1997 and 2001; (3) irregularly spaced observations at Jodrell Bank on 387 days between 1995 and 2001, with an average of five days between epochs; (4) twenty Green Bank sessions spaced roughly two months apart, each performed over four consecutive days at two frequencies; and (5) four campaigns at Green Bank

covering the full orbit, two each in 1995 and 1998.

At the 305-m telescope in Arecibo, Puerto Rico, the Princeton Mark IV data-acquisition system collected three or four 29-minute data sets each day at 430 and 1410 MHz. Total-intensity pulse profiles of 1024 bins were built from integrations of 190 seconds.

The 140 Foot (43-m) telescope at Green Bank, West Virginia observed the pulsar for 30–60 minutes a day at 370, 575 or 800 MHz. The "Spectral Processor," a digital Fourier transform spectrometer, divided the signals into 512 spectral channels across a 40-MHz passband in each of two polarizations. The spectra were folded synchronously at the pulse period over an integration time of 300 seconds, producing pulse profiles with 128 phase bins each.

The 76-m Lovell telescope at Jodrell Bank, England carried out a typical observation of 30 minutes at 410, 606 or 1400 MHz. The signal was dedispersed on-line in each of two polarizations using filterbank spectrometers with bandwidths of 64×0.125 MHz for the 400 and 600 MHz data and 32×1, 32×3, and 64×1 MHz for the 1400 MHz data. The detected signals were folded synchronously to make a pulse profile.

In all cases, the conventional techniques described in § 1.4.5 were used to measure pulse arrival times. In a further step, sets of TOAs from Arecibo and Green Bank were averaged over intervals of 29 minutes (sometimes longer at Green Bank) following the procedure in Appendix A. The observation lengths spanned by the TOAs, both average and not, are listed under "Typical Integration" in Table 4.1.

4.3   Timing Model

Table 4.2 lists the best-fit timing parameters. The five standard Keplerian elements as well as one PK parameter, the rate of periastron advance, were necessary to describe the orbit. Also included in the model were spin period and its time derivative,

Table 4.2: Timing parameters of PSR 0621+1002[a].

Right ascension, α (J2000)	$06^{\mathrm{h}}21^{\mathrm{m}}22^{\mathrm{s}}\!.11108(3)$
Declination, δ (J2000)	$+10°02'38''\!.741(2)$
Proper motion in R.A., $\mu_\alpha = \dot\alpha \cos\delta$ (mas yr^{-1})...	3.5(3)
Proper motion in Dec., $\mu_\delta = \dot\delta$ (mas yr^{-1})	$-0.3(9)$
Pulse period, P (ms)	28.853860730049(1)
Period derivative, $\dot{P}_{\mathrm{obs}}$ (10^{-20})	4.732(2)
Frequency, ν (Hz)	34.657407178742(1)
First derivative of ν, $\dot\nu$ ($10^{-17}\,\mathrm{s}^{-2}$)	$-5.684(2)$
Epoch (MJD [TDB])	50944.0
Orbital period, P_b (days)	8.3186813(4)
Projected semi-major axis, x (lt-s)................	12.0320744(4)
Eccentricity, e	0.00245744(5)
Epoch of periastron, T_0 (MJD [TDB])	50944.75683(4)
Longitude of periastron, ω (deg).................	188.816(2)
Periastron rate of change, $\dot\omega$ (deg yr^{-1})	0.0116(8)
Dispersion measure[b], DM (pc cm^{-3})	36.6010(6)

<div align="center">Measured Upper Limits</div>

Parallax (mas)	< 2.7
Pulse period second derivative, $\ddot{P}$ (s^{-1})	$< 4 \times 10^{-30}$
Orbital period rate of change, $\dot{P}_b$	$< 5 \times 10^{-12}$
Orbital axis rate of change, $\dot{x}$	$< 1.5 \times 10^{-14}$

<div align="center">Derived Parameters</div>

Mass function, f_1 (M$_\odot$)...........................	0.027026841(4)
Total mass, M (M$_\odot$)	2.81 ± 0.30
Pulsar mass, m_1 (M$_\odot$)...........................	$1.70^{+0.32}_{-0.29}$
Companion mass, m_2 (M$_\odot$).......................	$0.97^{+0.27}_{-0.15}$
Characteristic age (yr)	1.1×10^{10}
Surface magnetic field strength (Gauss)...........	1.2×10^9
Composite proper motion, μ (mas yr^{-1})	3.5(3)

[a]Figures in parentheses are uncertainties in the last digit quoted.

[b]The DM varies. The value here is the constant term in an 18-term polynomial expansion.

position, proper motion, and a time-varying DM (§4.3.1). Before we boosted the statistical uncertainties of the TOAs (§ 1.5.5), the goodness-of-fit statistic of the original fit was high, $\chi^2/\nu = 3.4$, where $\nu = 740$ is the number of degrees of freedom. Included in the Table 4.2 are upper limits on parameters that were not detected. The limits were found by allowing the extra parameters to vary one at a time in the fit. In addition to the items in the table, we carried out an extensive search for Shapiro delay (§4.4.4).

4.3.1   Dispersion Measure Variations

For many pulsars, the DM can accurately be characterized as a single number that holds steady over years of observation. This is not true for PSR J0621+1002. Figure 4.1a shows the residual pulse arrival times after removing a model with a fixed DM. Temporal variations in the DM are visible as secular trends in the residuals. As expected for an effect that scales as $1/f^2$, the lowest observing frequencies in the figure have the largest residuals. We find the integrated pulse profile of PSR J0621+1002 to be stable across the duration of the observations, so that no part of the trends in Figure 4.1a results from intrinsic changes in the pulsar emission pattern.

We incorporated DM variations into the timing model using an 18-term polynomial spanning the entire data set,

$$\mathrm{DM}(t) = \mathrm{DM}_0 + \sum_{i=1}^{17} \mathrm{DM}_i (t - t_0)^i, \tag{4.1}$$

where t_0 is the epoch of the parameter fit and the constant term DM_0 is the value quoted for DM in Table 4.2. The polynomial coefficients were simultaneously fit with all other parameters in the global timing solution. The DM_0 term was derived, in effect, from the 575 and 800 MHz data sets from Green Bank, which were collected with the same data acquisition system and timed using the same standard template. The higher-order terms depended on all the data sets.
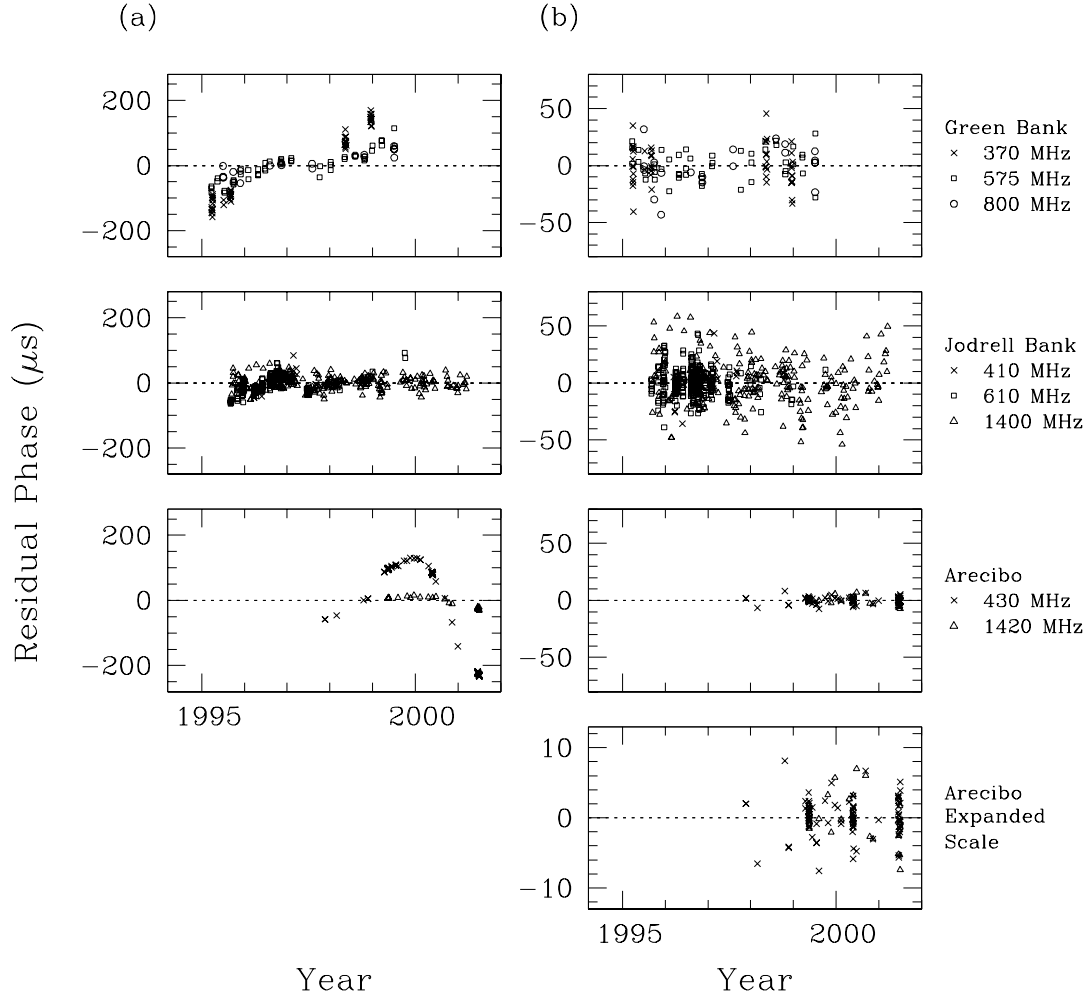
Figure 4.1: Postfit timing residuals of PSR J0621+1002 with and without DM variations. In (a) the DM is held constant, while in (b) the DM is modeled as an 18-term polynomial. Note the difference in the vertical scales of the two plots and, in particular, the scale of the Arecibo panel, emphasizing the high precision of TOAs from that observatory.

Figure 4.1b shows residual arrival times after subtracting the polynomial DM. Now the residuals are consistent with Gaussian noise except perhaps for an upward rise in the Jodrell Bank points in early 2001, a period over which all TOAs belong to a single frequency (1400 MHz), so that the DM at those epochs is poorly constrained. These same TOAs have some of the largest uncertainties in the data set, however, and so the unmodeled trend in them has a negligible effect on the overall parameter fit.

4.3.2   Pulsar Astrometry and Spin-down Behavior

The TC93 model of interstellar free-electron density puts the pulsar distance at $d = 1.9$ kpc, while the NE2001 model gives $d = 1.35$ kpc (see § 3.4.2). The spread of distance estimates, combined with the total proper motion, $\mu = 3.5$ mas yr^{-1}, gives a relative Sun-pulsar transverse velocity in the range $V = \mu d = 23 - 32$ km/s. The pulsar is at a small distance from the Galactic plane, $z = |d \sin b| \lesssim 0.07$ kpc, where $b = -2°0$ is the pulsar's Galactic latitude.

Camilo et al. (2001) have noted that IMBPs tend to have a Galactic scaleheights smaller than those of LMBPs by a factor of 2–4, and that this could be due to their possessing space velocities V smaller than those of LMBPs by a factor $\lesssim 2$. The low space velocity of PSR J0621+1002 supports this notion. With this result there are now four IMBPs with measured proper motions, for which the space velocities are all approximately 40 ± 10 km s^{-1} (Toscano *et al.* 1999b; Kramer *et al.* 1999b). These velocities compare to $V \approx 100$ km s^{-1} for a larger population of MSPs composed largely of LMBPs and isolated pulsars (Nice and Taylor 1995; Cordes and Chernoff 1997; Lyne *et al.* 1998; Toscano *et al.* 1999b). A partial explanation for this discrepancy resides in the different evolutionary histories of the two binary classes: LMBP progenitors are $1 + 1.3$ M$_\odot$ binaries, while IMBPs may evolve from $4 + 1.3$ M$_\odot$

systems. For identical center-of-mass impulses following the supernova explosion, the pulsars in the latter systems will acquire smaller space velocities.

The observed time derivative of the spin period, $\dot{P}_{\mathrm{obs}}$, is slightly biased away from its intrinsic value, $\dot{P}_{\mathrm{int}}$, from Doppler accelerations caused by differential rotation in the Galactic plane and by proper motion (see § 3.4.4). A potential third source of bias, acceleration perpendicular to the plane of the Galaxy, is negligible because of PSR J0621+1002's proximity to the plane. With the bias subtracted off, we estimate $\dot{P}_{\mathrm{int}} = (4.3-4.4) \times 10^{-20}$, about 10% smaller than $\dot{P}_{\mathrm{obs}}$.

Under ordinary assumptions about the pulsar spin-down mechanism, the period and intrinsic period derivative yield a characteristic age (eqn. 1.39) of $\tau = 1.1 \times 10^{10}\,\mathrm{yr}$ and a surface magnetic field strength (eqn. 1.36) of $B_0 = 1.2 \times 10^9\,\mathrm{G}$.

4.4　Pulsar and Companion Masses

Our goal is to determine the pulsar mass, m_1, and the companion mass, m_2. The allowed values of the masses are constrained by the Keplerian orbital elements, the nature of the companion star, the apsidal motion of the binary system, and the lack of detectable Shapiro delay. In this section, we discuss each of these factors in turn and display the resulting constraints on the masses in Figure 4.2. The related restrictions on m_2 and orbital inclination angle i are shown in Figure 4.3.

4.4.1　Keplerian Orbit

The masses and the inclination angle are related through the Keplerian mass function,

$$f_1(m_1, m_2, i) \equiv \frac{(m_2 \sin i)^3}{(m_1 + m_2)^2} = x^3 \left(\frac{2\pi}{P_b}\right)^2 \left(\frac{1}{T_\odot}\right)$$
$$= 0.027026841 \pm 0.000000004\,\mathrm{M}_\odot. \tag{4.2}$$
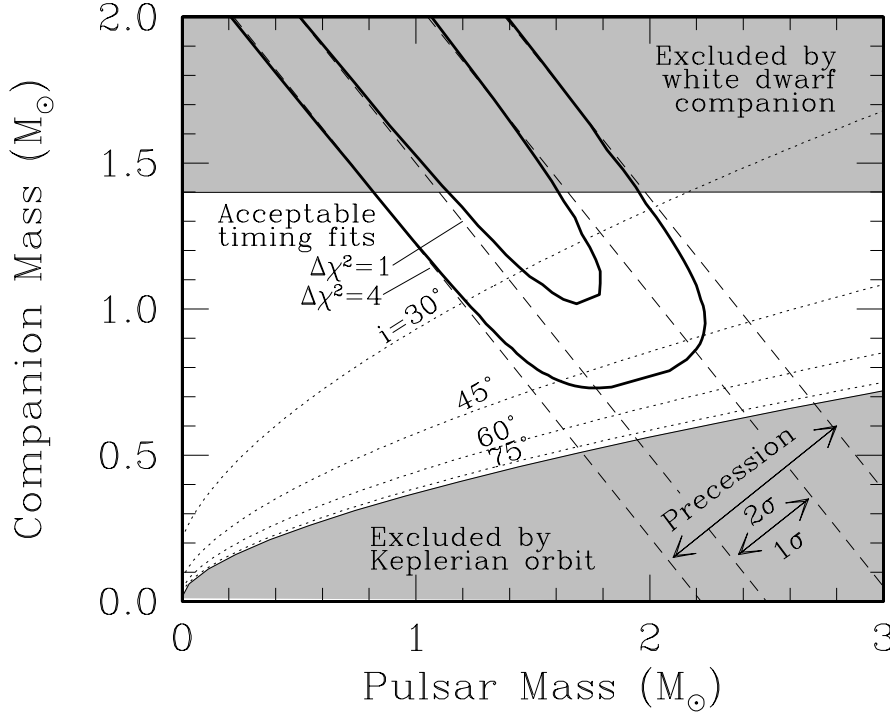
Figure 4.2: The $m_1 - m_2$ plane for the PSR J0621+1002 system. Acceptable values of the two masses lie in the white region. The lower shaded region is off-limits by the requirement that $\sin i \leq 1$, while the upper shaded region is excluded by that fact that $m2 \leq 1.4 \, M_\odot$ for a white dwarf. The solid contours of $\Delta\chi^2 = 1$ and $\Delta\chi^2 = 4$ represent confidence levels of 39% and 86%, respectively. Dashed lines give limits on total system mass M from $\dot\omega$ measurement. Dotted lines show constant values of orbital inclination angle i.

Since $\sin i \leq 1$, equation 4.2 can be rewritten to give an upper limit on m_1 in terms of m_2,

$$m_1 \leq m_2^{3/2} f_1^{-1/2} - m_2. \tag{4.3}$$

This constraint is shown as the lower shaded region in Figure 4.2.
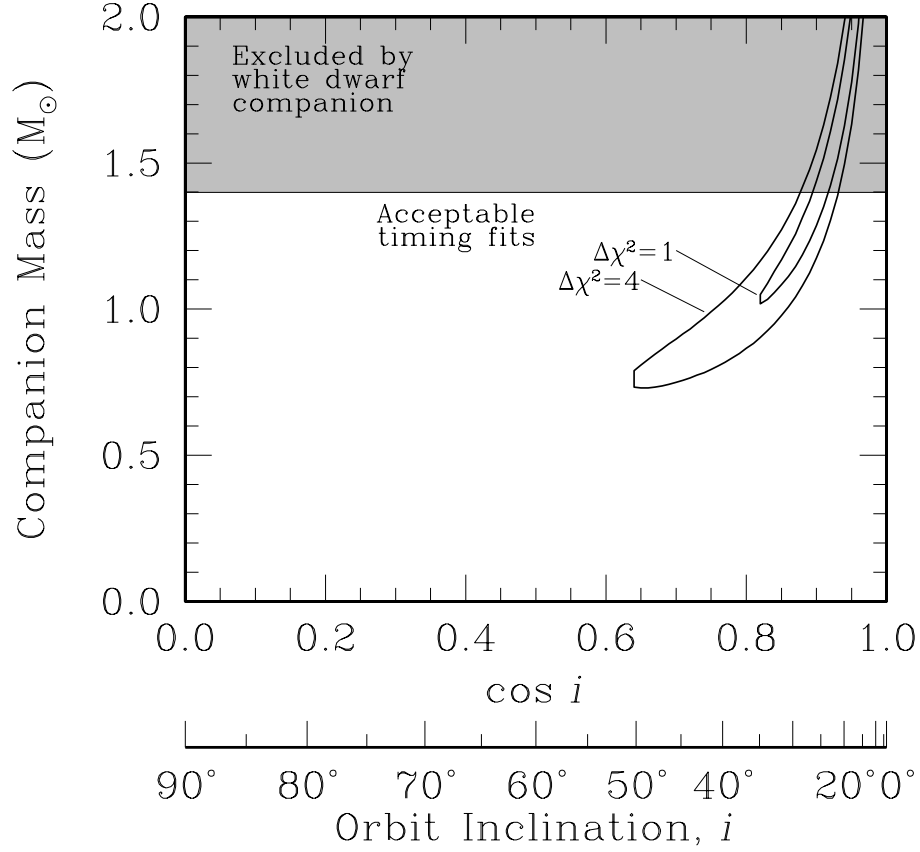
Figure 4.3: Joint PDF of m_2 and $|\cos i|$ for the PSR J0621+1002 system. Contours of $\Delta\chi^2 = 1$ and $\Delta\chi^2 = 4$ represent confidence levels of 39% and 86%, respectively.

4.4.2   Upper Limit on Companion Mass

The companion to the pulsar must be either a main sequence star, a neutron star, a black hole, or a white dwarf. The first possibility can be ruled out, as optical observations using the Hubble Space Telescope find no evidence that the secondary is a main sequence star (F. Camilo, private communication). The second possibility can also be eliminated, since it is improbable that a double neutron star binary could have survived two supernova explosions and yet retained the small eccentricity of

the PSR J0621+1002 system (Portegies Zwart and Yungelson 1998). A pulsar-black hole binary is also unlikely to have such a circular orbit (Lipunov *et al.* 1994). The companion must therefore be a white dwarf, and as such, its mass, m_2, must be lower than the Chandrasekhar limit, $1.4\,\mathrm{M_\odot}$. This constraint is illustrated as the upper shaded region in Figure 4.2.

4.4.3   Relativistic Periastron Advance

The measured rate of periastron advance, $\dot{\omega}$, provides another relation between m_1 and m_2. For the PSR J0621+1002 system, we assume that nonrelativistic contributions to apsidal motion are negligibly small (see §4.4.6). The general relativistic interpretation of $\dot{\omega}$ in equation 1.23 then yields the combined mass of the stars,

$$
\begin{aligned}
M \equiv m_1 + m_2 \;&=\; \left(\frac{P_b}{2\pi}\right)^{5/2}\left[\frac{(1-e^2)\,\dot{\omega}}{3}\right]^{3/2}\left(\frac{1}{T_\odot}\right)\\
&=\; 2.81 \pm 0.30\,\mathrm{M_\odot}.
\end{aligned}
\tag{4.4}
$$

This constrains m_1 and m_2 to lie within the strips indicated by dashed lines in Figure 4.2.

4.4.4   Shapiro Delay

Orbital Shapiro delay is not detected in the PSR J0621+1002 timing data. Yet the amplitude of the effect is expected to be around $15\,\mu$s, which would make Shapiro delay easily detectable if the inclination angle were large (see § 3.5.2). The fact that the delay is not observed therefore implies that the orbit is tilted substantially away from an edge-on orientation.

   To explore the statistical limits that both the detection of periastron advance and the non-detection of Shapiro delay place on i and m_2 (and hence on m_1), we utilized the procedure outlined in Appendix B, fitting the TOAs across a grid of m_2 and $\cos i$

values to a timing model containing $\dot{\omega}$ and the Shapiro terms and then converting the resulting values of the goodness-of-fit statistic χ^2 to probabilities. The solid contours in Figure 4.2 show the regions in which acceptable timing solutions were found. The interpretation of the contours is straightforward: within the area allowed by the precession measurement, the non-detection of Shapiro delay excludes solutions with "edge-on" orbits, and so the strip is truncated at low values of $\cos i$. Figure 4.3 shows that the inclination angle is constrained with a high degree of confidence to be less than $50°$.

Using the calculated probabilities, we also obtain the individual PDFs of m_1, m_2, and $\cos i$ shown in Figure 4.4. The PDFs yield the maximum likelihood estimates

$$
\begin{aligned}
m_1 &= 1.70^{+0.32}_{-0.29}\,\mathrm{M}_\odot\ (68\%\ \text{confidence}) \\
&= 1.70^{+0.59}_{-0.63}\,\mathrm{M}_\odot\ (95\%\ \text{confidence})
\end{aligned}
\tag{4.5}
$$

for the pulsar,

$$
\begin{aligned}
m_2 &= 0.97^{+0.27}_{-0.15}\,\mathrm{M}_\odot\ (68\%\ \text{confidence}) \\
&= 0.97^{+0.43}_{-0.24}\,\mathrm{M}_\odot\ (95\%\ \text{confidence})
\end{aligned}
\tag{4.6}
$$

for the companion, and

$$
\begin{aligned}
\cos i &= 0.87^{+0.04}_{-0.10}\ (68\%\ \text{confidence}) \\
&= 0.87^{+0.06}_{-0.24}\ (95\%\ \text{confidence}).
\end{aligned}
\tag{4.7}
$$

We note that the sum of the maximum likelihood estimates, $2.67\,\mathrm{M}_\odot$, is less than the total system mass derived in equation 4.4 from periastron advance alone, $2.81\,\mathrm{M}_\odot$. This is primarily a consequence of the upper limit on the companion mass, $m_2 \leq 1.4\,\mathrm{M}_\odot$, which preferentially excludes solutions with high total mass, as can be seen in Figure 4.2.
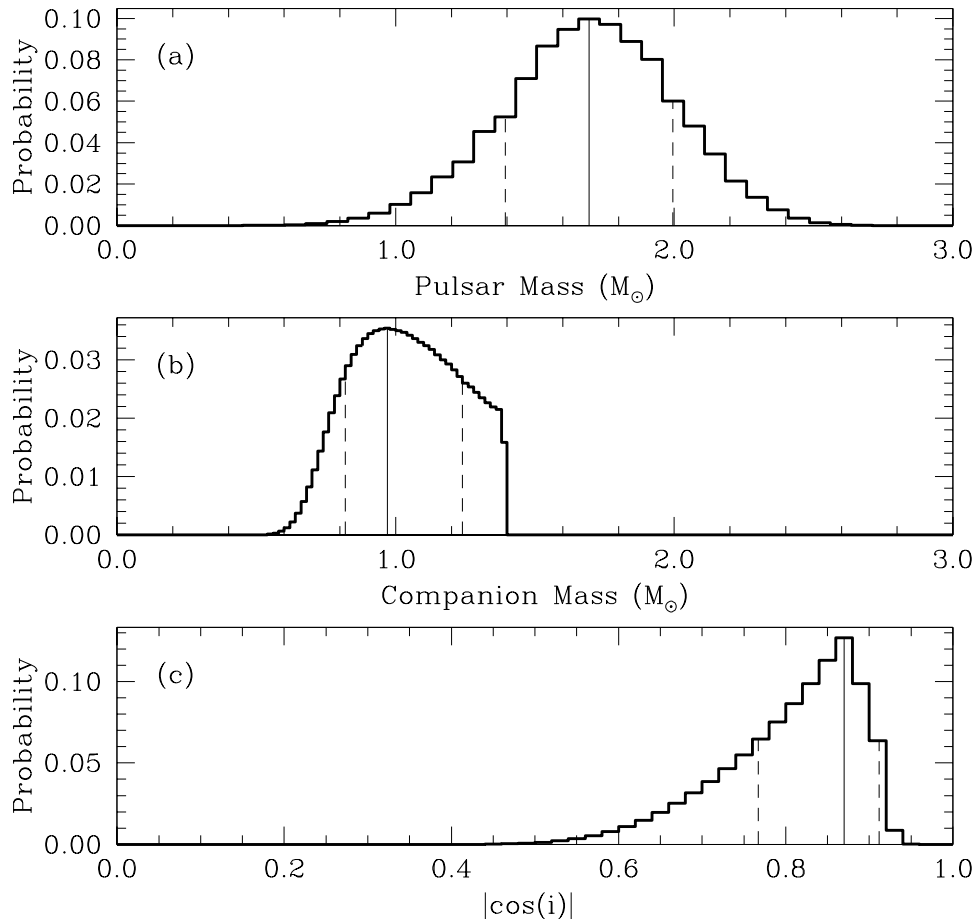
Figure 4.4: PDFs of (a) m_1, (b) m_2, and (c) $\cos i$ for the PSR J0621+1002 system. The solid vertical lines mark the maximum likelihood values of the masses. The dashed vertical lines delimit 68% confidence regions; they represent the shortest widths along the mass axes that both enclose the peaks and contain 68% of the area under the curves. For the companion mass, the sharp falloff in the histogram reflects the assumption that $m_2 \leq 1.4\,M_\odot$.

4.4.5   Interpretation of the Masses

The conventional wisdom is that neutron stars in white dwarf-pulsar systems are not much more massive than those in double neutron star binaries, even though the secondaries must lose several tenths of a solar mass as they evolve toward white dwarfs.

In particular, Thorsett & Chakrabarty (1999) find that the masses of neutron stars orbiting either white dwarfs or other neutron stars are consistent with a remarkably narrow Gaussian distribution, $m = 1.35 \pm 0.04 \, M_\odot$. While our measurement of the mass of PSR J0621+1002 is in statistical agreement with that result, the maximum likelihood value is suggestively high, allowing the possibility that a substantial amount of mass was transferred onto the neutron star.

Our estimate of the companion mass implies that the star is probably an ONeMg white dwarf and ranks it among the heaviest known white dwarfs in orbit around a pulsar. As van Kerkwijk & Kulkarni (1999) have pointed out, there are only a few known few massive white dwarfs ($m_2 > 1 \, M_\odot$) that evolved from a single massive progenitor star. They argue that the companion to PSR B2303+46, a young pulsar in an eccentric orbit, is such a object. Our timing of PSR J0621+1002 shows that its companion is similarly likely to have descended from a massive star, even though the histories of mass loss and accretion in the eccentric PSR B2303+46 binary, whose pulsar did not spin up, and the circular PSR J0621+1002 binary, whose pulsar spun up significantly, must have been very different.

Given the mass estimates, it seems likely that the PSR J0621+1002 system formed through a common envelope and spiral-in phase (Taam, King, & Ritter 2000; Tauris, van den Heuvel, & Savonije 2000). In this scenario, the companion originally had a mass of $5 - 7 \, M_\odot$, and the pulsar, initially in a wide orbit with a binary period of a few hundred days, spiraled in to its current orbit of $P_b = 8.3$ under a drag force arising from its motion through the envelope. The same formation mechanism has been put forward for PSR J1454−5846, an object quite similar to PSR J0621+1002, with a 12.4-day orbital period, a 45.2-ms spin period, an eccentricity of 0.002, and a companion mass of $\sim 1.1 \, M_\odot$ (Camilo *et al.* 2001).

4.4.6   Classical Periastron Advance

The above analysis assumed that the observed apsidal motion can be entirely attributed to relativity. In principle, however, periastron advance could also be caused by tidal interactions of the pulsar and the secondary star. Smarr & Blandford (1976) considered this possibility in the context of a potential white dwarf companion to the Hulse-Taylor binary pulsar, PSR B1913+16. Their analysis can also be applied to PSR J0621+1002. They found tidal deformation of the companion to contribute negligibly to $\dot\omega$ for PSR B1913+16. Since the apsidal advance per binary period due to tidal deformation scales as a^{-5}, where a is the major axis, this effect can also be neglected in the wider PSR J0621+1002 system.

A potentially more important effect is rotational deformation, which becomes significant if the secondary is spinning rapidly. The precession rate due to rotation is

$$\dot\omega_{\rm rot} = nQ \left(1 - \tfrac{3}{2}\sin^2\theta + \cot i \sin\theta \cos\theta \cos\Phi_0\right) \tag{4.8}$$

(Wex 1998), in which $n = 2\pi/P_b$ and

$$Q = \frac{3k_2 R_2^5 \Omega^2}{a^2 G m_2 (1-e^2)^2}, \tag{4.9}$$

where k_2, R_2, Ω_2, and m_2 are the structure constant, radius, angular velocity, and mass of the secondary; θ is the angle between the angular momentum vector of the secondary and the angular momentum vector of the orbit; and Φ_0 is the longitude of the ascending node in a reference frame defined by the total angular momentum vector (see Fig. 9 of Wex 1998). Neither θ nor Φ_0 is known, so we must allow for all possible values in the ranges $0 < \theta < \pi$ and $0 < \Phi_0 < 2\pi$. Substituting PSR J0621+1002's Keplerian orbital parameters, the formula can be written in the notation of Smarr & Blandford (1976):

$$\dot\omega_{\rm rot} = 0\!\!\overset{\circ}{.}000163\,{\rm yr}^{-1} \left(\frac{M_\odot}{m_1+m_2}\right)^{2/3} \alpha_6 \tag{4.10}$$

$$\times \left(1 - \tfrac{3}{2}\sin^2\theta + \cot i \sin\theta \cos\theta \cos\Phi_0\right), \tag{4.11}$$

where $\alpha = 2k_2 R_2^5 \Omega_2^2 / (3Gm_2)$ and $\alpha_6 = \alpha/(10^6 \, \mathrm{km}^2)$. To gauge the largest value that $\dot{\omega}_{\mathrm{rot}}$ could attain, we will use limits on the masses and the orbital inclination angle from the relativistic analysis, recognizing that they would need to be modified should $\dot{\omega}_{\mathrm{rot}}$ be found significant. Our observations constrain $20° < i < 50°$, so that $1.2 < \cot i < 2.7$ (see Fig. 4.3), for which the maximum value of the geometric factor in equation 4.11 is 1.7, attained at $\theta = 40°$ and $\Phi_0 = 0$. Analyzing models of rotating white dwarfs, Smarr & Blandford (1976) found that $\alpha_6 \lesssim 15$. Combining these restrictions with our measured value of total system mass, the precession due to rotation for PSR J0621+1002 can be as high as $\dot{\omega}_{\mathrm{rot}} \lesssim 0°\!.0021 \, \mathrm{yr}^{-1}$, about 20% of our observed value.

There is reason to believe that the classical contribution to the observed $\dot{\omega}$ is smaller than this. In most cases, a rotational deformation will induce a change in the projected semi-major axis of the orbit, $x = a_1 \sin i / c$. Wex (1998) shows the rate of change to be

$$\frac{\dot{x}}{x} = nQ \cot i \sin \theta \cos \theta \sin \Phi_0, \tag{4.12}$$

from which

$$\dot{\omega}_{\mathrm{rot}} = \frac{\dot{x}}{x} \left(\frac{1 - \frac{3}{2} \sin^2 \theta + \cot i \sin \theta \cos \theta \cos \Phi_0}{\cot i \sin \theta \cos \theta \sin \Phi_0} \right). \tag{4.13}$$

Thus, our observed upper limit of $|\dot{x}/x| < 1.2 \times 10^{-15}$ implies that $\dot{\omega}_{\mathrm{rot}}$ is no more than $1.2 \times 10^{-15} \, \mathrm{rad \, s}^{-1} = 7°\!.1 \times 10^{-6} \, \mathrm{yr}^{-1}$ times a geometric factor. Unfortunately, certain special combinations of i, θ, and Φ_0 will make the geometric factor large. For this reason, we cannot definitively exclude the possibility that rotational precession contributes to the observed value of $\dot{\omega}$. For most cases, however, the geometric factor will be of order unity, and so the upper limit on $\dot{\omega}_{\mathrm{rot}}$ will be substantially smaller than our observed value of $\dot{\omega}$. Because of this, and because there is no reason to expect the secondary to be rapidly rotating, we have chosen to ignore $\dot{\omega}_{\mathrm{rot}}$ in our analysis of the pulsar and companion masses.
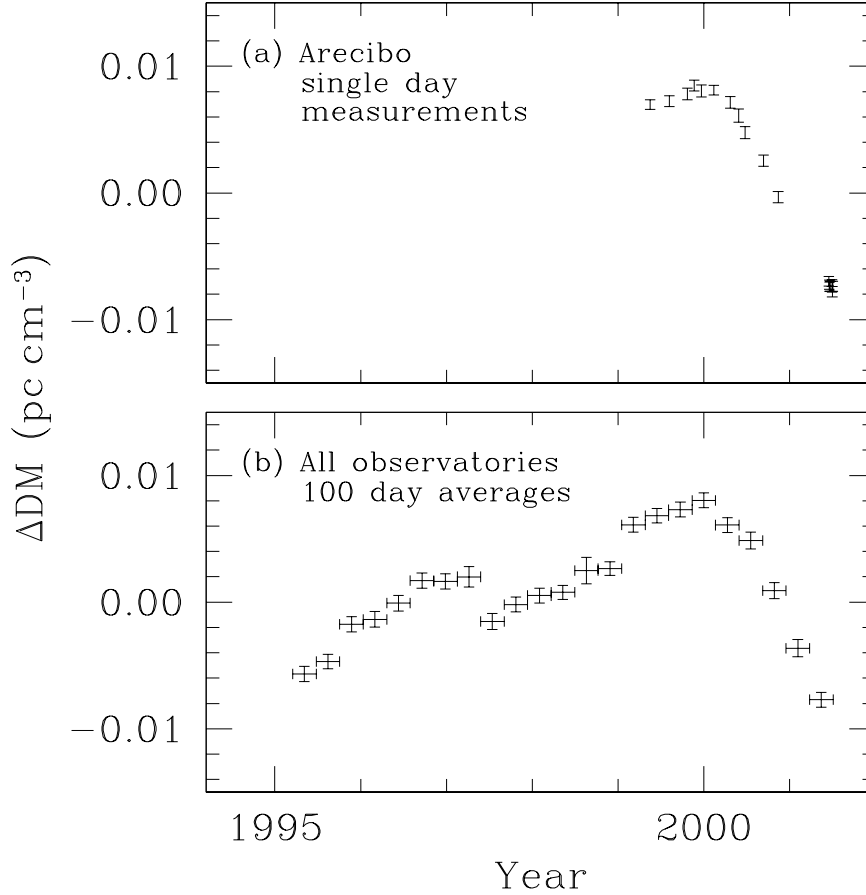
Figure 4.5: DM variations of PSR J0621+1002, with $\Delta DM = DM - 36.6010$. Vertical bars are 1σ uncertainties in the variations. Panel (a) shows measurements from single days of dual-frequency observations at Arecibo. Panel (b) shows values derived from TOAs from all observatories averaged over intervals of 100 days, as indicated by horizontal bars.

4.5   Density Irregularities in the ISM

4.5.1   Temporal DM Variations

Figure 4.5a shows the DM of PSR J0621+1002 calculated on individual days on which data were collected at Arecibo at both 430 and 1410 MHz (see also § 4.3.1). A DM

drift as steep as $0.013 \, \mathrm{pc \, cm^{-3} \, yr^{-1}}$ can be seen in the plot. If not properly modeled, such a gradient would shift the TOAs by up to $7 \, \mu\mathrm{s}$ at $430 \, \mathrm{MHz}$ over the 8-day pulsar orbit, a systematic effect significantly larger than the measurement uncertainties of the Arecibo TOAs. The DM gradient is among the largest ever detected in a pulsar outside a nebula (Backer *et al.* 1993).

Variations in the DM can be used to investigate inhomogeneities in the interstellar electron density. For this purpose, we modeled the DM as a series of step functions in time, as shown in Figure 4.5b. The width of the step intervals, 100 days, was a compromise between the goal of sampling DM as frequently as possible and the need for each segment to span enough multi-frequency data for the DM to be reliably calculated.

In Figure 4.5b, there appear to be discontinuities in the DM at 1997.4 and 1999.0. With a careful check of the data around these dates, we confirmed that the DM did indeed change by the amounts shown within the 100-day time resolution of the figure, and that the increase and decrease are not artifacts of binning the DM or of joining together data from different receivers and telescopes. However, the data do not allow us to distinguish between nearly instantaneous jumps in DM, as seen in the Crab pulsar signal (Backer, Wong, & Valanju 2000), and slower changes on a scale of 100 days. Given the rapid but apparently smooth variations in DM seen after 2000 in the Arecibo data (which is sampled more frequently than once every 100 days in Fig. 4.5a), we suspect the DM to be strongly but continuously varying at the earlier epochs as well.

4.5.2   Structure Function Analysis

The DM variations in Figure 4.5 result from the passage across the line of sight of density irregularities in the ionized ISM. The spatial structure of the irregularities
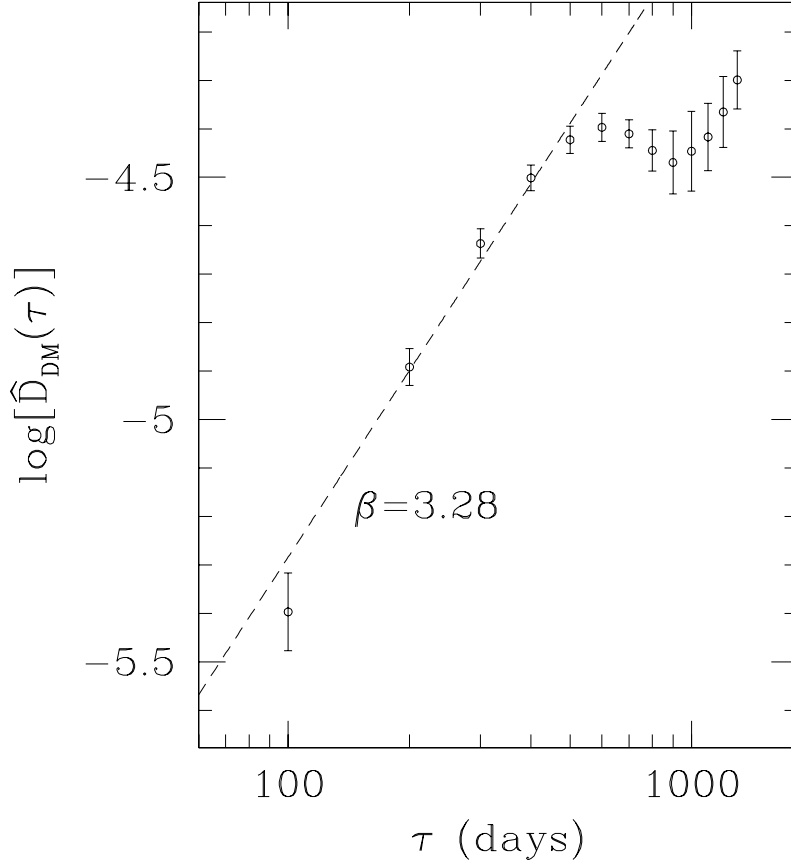
Figure 4.6: Structure function of DM variations of PSR J0621+1002 (Fig. 4.5). The points clearly do not all follow a single power law. As indicated by the dashed line, a power law was least-squares fitted to the first five points according to equation 4.15, yielding the spectral index, β.

can be discerned using the two-point structure function of the DM,

$$D_{\mathrm{DM}}(\tau) \equiv \left\langle [\mathrm{DM}(t + \tau) - \mathrm{DM}(t)]^2 \right\rangle, \tag{4.14}$$

where τ is the time lag between DM measurements and where the angular brackets denote ensemble averaging (e.g., Cordes et al. 1990). The time lag of DM variations can be related to the spatial size, l, of the density inhomogeneities through a simple

model of the ISM. In it, irregularities in the ISM are assumed to be "frozen in" a thin screen midway between Earth and the pulsar. The pulsar velocity, V, causes the Earth-pulsar line of sight to traverse the screen with velocity $V/2$. Hence, lag is related to spatial size via $l = V\tau/2$.

The structure function $D_{\mathrm{DM}}(\tau)$ can be derived from the measured DM values at times t_i through the unbiased estimator

$$\hat{D}_{\mathrm{DM}}(\tau) = \frac{1}{N(\tau)} \sum_{i=1}^{N(\tau)} [\mathrm{DM}(t_i + \tau) - \mathrm{DM}(t_i)]^2 - \sigma_{\mathrm{DM}}^2, \qquad (4.15)$$

where $N(\tau)$ is the number of DM pairs that enter into the summation at a given lag τ and where σ_{DM} is the mean uncertainty of the DM values. Figure 4.6 illustrates values of $\hat{D}_{\mathrm{DM}}(\tau)$ calculated this way for PSR J0621+1002. The uncertainties were computed by assuming Gaussian statistics for the fitted DM values and formally propagating their covariances through equation 4.15. We restrict τ to values for which $N(\tau) \geq 10$, thereby extending the lag from a minimum of 100 days to a maximum of 1300 days, about half the length of our full data span.

4.5.3   Not a Simple Power Law

The structure function in Figure 4.6 presents a puzzle because it is not the simple power law that is predicted by standard theories of the ISM and that is seen in the direction of other pulsars. In the standard picture, a power law arises from the expectation that turbulence spreads energy from longer to shorter length scales. Accordingly, the spectrum of perturbations in the electron density is modeled in terms of the spatial frequency, $q = 2\pi/l$, via

$$P(q) \propto q^{-\beta} \qquad (4.16)$$

(Rickett 1990). The relation is hypothesized to hold over some range of wave numbers, $q_i < q < q_o$; below some "inner scale" $q_i = 2\pi/l_i$ and above some "outer scale" $q_o =$

$2\pi/l_o$, various damping mechanisms are expected to cut off the turbulent energy flow. With the assumed linear relation between l and τ, the structure function becomes

$$D_{\mathrm{DM}}(\tau) = \left(\frac{\tau}{\tau_0}\right)^{\beta-2}, \tag{4.17}$$

where τ_0 is a normalization constant. The index β is usually predicted to be near the Kolmogorov value for turbulence in neutral gases, $11/3$. Studies of DM variations in other pulsars have uncovered power laws with indices close to that value (Phillips & Wolszczan 1992; Kaspi, Taylor, & Ryba 1994; Cognard & Lestrade 1997).

The phase structure function in Figure 4.6 is obviously not a simple power law. It is not clear how to interpret this. A power law, marked by the dashed line, can be fit to the first five points in the plot. The slope of the line yields a spectral index, $\beta = 3.28 \pm 0.09$, that is reasonably close to the Kolmogorov value. At lags longer than 500 days, the power law fails to hold, although there is a hint of its reemergence at the longest lags. The flattening out of the structure function at 500 days is a direct consequence of the two sharp breaks in the DM time series (see Fig. 4.5b). If we take the Sun-pulsar transverse velocity to be $V = 27\,\mathrm{km\,s^{-1}}$, then 500 days corresponds to a length of $l = V\tau/2 = 5.5 \times 10^{13}\,\mathrm{cm}$, implying structure in the electron density power spectrum at this scale.

4.6   Future Prospects

We have found substantial constraints on the masses of PSR J0621+1002 and its orbital companion. The pulsar mass is found to be $m_1 = 1.70^{+0.32}_{-0.29}\,\mathrm{M}_\odot$ (68% confidence). The lower end of this uncertainty range is near the canonical pulsar mass of $1.35\,\mathrm{M}_\odot$, but the mass may also be several tenths of a solar mass higher, allowing the possibility that a substantial amount of material accreted onto the neutron star during the evolution of the system. The mass of the secondary, $m_2 = 0.97^{+0.27}_{-0.15}\,\mathrm{M}_\odot$

(68% confidence), makes it one of the heaviest known white dwarfs orbiting a pulsar.

Can the mass measurements be improved by continued timing observations? Unfortunately, PK effects beyond those considered in this paper, such as orbital period decay, and gravitational redshift and time dilation, will not be detectable in the timing data for PSR J0621+1002 in the foreseeable future, so any improvement must come about through tighter measurements of $\dot{\omega}$ and Shapiro delay.

The uncertainty in the measurement of the total mass, $M = 2.81 \pm 0.30 \, \mathrm{M_\odot}$, scales linearly with the uncertainty of $\dot{\omega}$, which in turn is inversely proportional to the time span over which data are collected. This has a simple explanation: the longer the time span of the observations, the more ω shifts, and so the easier it is to measure $\dot{\omega}$. The highest precision data used in this work—the annual Arecibo campaigns—were collected over two years. A similar campaign carried out several years in the future would shrink the uncertainty in M by a factor of a few.

The pulsar and companion masses were further constrained by Shapiro delay. The precision of the Shapiro delay measurement (or limit) has no dependence on data span length, so its uncertainty is reduced only as $n^{-1/2}$, where n is the number of observations. At best, a modest improvement could be made with existing radio telescope resources.

Chapter 5

PSR J0751+1807: A Test of the Strong Equivalence Principle

The Strong Equivalence Principle (SEP) states that a body's response to a gravitational field does not depend on its gravitational self-energy. In general relativity (GR), the SEP holds by fiat. But it is violated in some other theories of gravitation. Examples include tensor-scalar theories such as that of Brans & Dicke (BD) (Fierz 1956; Jordan 1959; Brans and Dicke 1961). Recently, the scalar field of "quintessence" has been invoked to explain the accelerated expansion of the universe observed in high-redshift type Ia supernovae and in the cosmic microwave background (CMB) (Tonry *et al.* 2003; Torres 2002; Caldwell, Dave, and Steinhardt 1998).

If the SEP is false, then two bodies with unequal self-energies will undergo different accelerations in the same gravitational field. The effect has been searched for unsuccessfully in the solar system (for a review, see Will 2001). A binary pulsar is a better place to look. A neutron star has a higher gravitational binding energy than any planet or non-compact star. It is easy to see why. The fraction of its rest energy that a star derives from its gravitational self energy is $E_{\mathrm{grav}}/mc^2 \simeq Gm/c^2R$, where m is the mass and R is the radius. For a typical pulsar, the fraction is 0.2. For the

Sun, it is 2×10^{-6}.

The binary PSR J0751+1807 is an especially promising place to test the SEP. For one thing, its tight orbit ($P_b = 0.3\,\mathrm{d}$), with its corresponding strong accelerations, gives rises to predictions of copious emission of gravitational radiation. Secondly, unlike most other well-studied tight binaries, its companion is a white dwarf instead of another neutron star. In SEP-violating theories, orbital evolution is typically a function of the difference in the gravitational self-energies of the two stars. The fractional binding energy of a light white dwarf is about four order of magnitude smaller than that of the neutron star.

Lundgren, Zepka, and Cordes (1995) (hereafter LZC95) discovered the MSP at Arecibo while following up a search for young pulsars in the direction of gamma-ray sources. Ironically, the γ-ray source that led them to that part of the sky turned out not to be associated with the pulsar. Subsequently, however, the MSP was detected in soft X-rays (Becker *et al.* 1996). Also, the white dwarf was detected optically (Lundgren *et al.* 1996).

We add an additional seven years of timing data to the TOAs taken by LZC95. The highlight of our results is a detection of orbital decay due to back reaction from gravitational radiation. In the first half of our analysis, we assume GR to be the correct theory of gravity and use the measured PK parameters to estimate the system masses and the orbital inclination angle. In the second half, we consider a broader range of gravitational theories and use the PK parameters to put limits on SEP violation.

5.1   Observations

Figure 5.1 summarizes the data. Because of the short binary period, we did not average TOAs over observing epochs (except at Jodrell Bank) as we did for the other

Table 5.1: Summary of Observations of PSR J0751+1807

Observatory	Dates	Frequency (MHz)	Bandwidth (MHz)	Number of TOAs	Typical Integration (min)	RMS Residual (μs)
Arecibo[a]	1993.8–1994.4	430	8	1189	2.0	25
Jodrell Bank	1994.4–1999.8	606	8	55	30	21[c]
	1994.0–2001.2	1410	32	181	30	17[c]
Effelsberg	1997.0–2001.7	1409	40	325	5.0	7.9
Arecibo[b]	1998.9–2001.5	430	5	662	3.2	5.3
	1997.9–2001.5	1410	10	109	3.2	6.9

[a]Data taken with the Mark III system.

[b]Data taken with the Mark IV system.

[c]Values incorporate the effect of averaging TOAs from shorter integration times.

MSPs in this thesis. Pulse arrival times were measured at three radio observatories. At Arecibo, the first points (already analyzed by LZC95) were taken using the Mark III system (§ 3.2). To those points we add post-upgrade TOAs taken by Mark IV (§ 2.3.1). At Jodrell Bank, data were acquired by the Lovell telescope (§ 4.2). At the 100-m dish at the Max Planck Institute für Radioastronomie in Effelsberg, Germany, TOAs were gathered by the Effelsberg-Berkeley Pulsar Processor (EBPP), a coherent-dedisperser nearly identical in design to the ABPP (§ 3.2).

5.2   Results

5.2.1   Proximity to the Plane of the Solar System

Table 5.2 lists the astrometric and spin parameters of PSR J0751+1807. The celestial coordinates are given not only in right ascension and declination, α and δ, but also in ecliptic longitude and latitude, λ and β. With an ecliptic latitude of $\beta = -2°8$,

Table 5.2: Astrometric and spin parameters of PSR J0751+1807[a].

Right ascension, α (J2000)	$07^\mathrm{h}51^\mathrm{m}09^\mathrm{s}.15680(7)$
Declination, δ (J2000)	$+18°07'38''.618(5)$
Proper motion in R.A., $\mu_\alpha = \dot{\alpha}\cos\delta$ (mas yr^{-1})	$-1.8(4)$
Proper motion in Dec., $\mu_\delta = \dot{\delta}$ (mas yr^{-1})	$-6.7(17)$
Ecliptic longitude, λ (J2000) (deg)	*116.33361856(4)*
Ecliptic latitude, β (J2000) (deg)	*-2.8075442(13)*
Proper motion in λ, $\mu_\lambda = \dot{\lambda}\cos\beta$ (mas yr^{-1})	*-0.56(6)*
Proper motion in β, $\mu_\beta = \dot{\beta}$ (mas yr^{-1})	*-6.9(18)*
Composite proper motion, μ (mas yr^{-1})	*6.9(17)*
Galactic longitude, l (deg)	*202.7296*
Galactic latitude, b (deg)	*21.0859*
Position angle of μ in equatorial coordinates, ϕ (deg)...	*195(5)*
Position angle of μ in Galactic coordinates, ϕ (deg)	*128(5)*
Pulse period, P (ms)	3.47877078245810(4)
Period derivative (observed), $\dot{P}_\mathrm{obs}$ (10^{-21})	7.7848(7)
Period derivative (intrinsic), $\dot{P}_\mathrm{int}$ (10^{-21})	*7.3(3)*
Frequency, ν (Hz)	287.457858690362(3)
First derivative of ν, $\dot{\nu}$ (10^{-16} s^{-2})......................	$-6.4328(6)$
Epoch (MJD [TDB]).................................	50714.0
Dispersion measure, DM (pc cm^{-3})	$30.24585(5)^b$
First derivative of DM, dDM$/dt$ (10^{-4} pc cm^{-3} yr^{-1})....	$-1.2(2)$
Distance, d (kpc)	*1.2(3)^c*
Characteristic age, τ (Gyr)	*7.5(3)*
Surface magnetic field strength, B_0 (G)	*1.66(3) × 10^8*

[a]Figures in parentheses are uncertainties in the last digit quoted, and italicized numbers represent quantities derived from fitted parameters.

[b]The quoted uncertainty is a formal estimate from the parameter fit and probably understates the true uncertainty.

[c]Distance is derived from DM using the NE2001 model of Cordes & Lazio (2002).
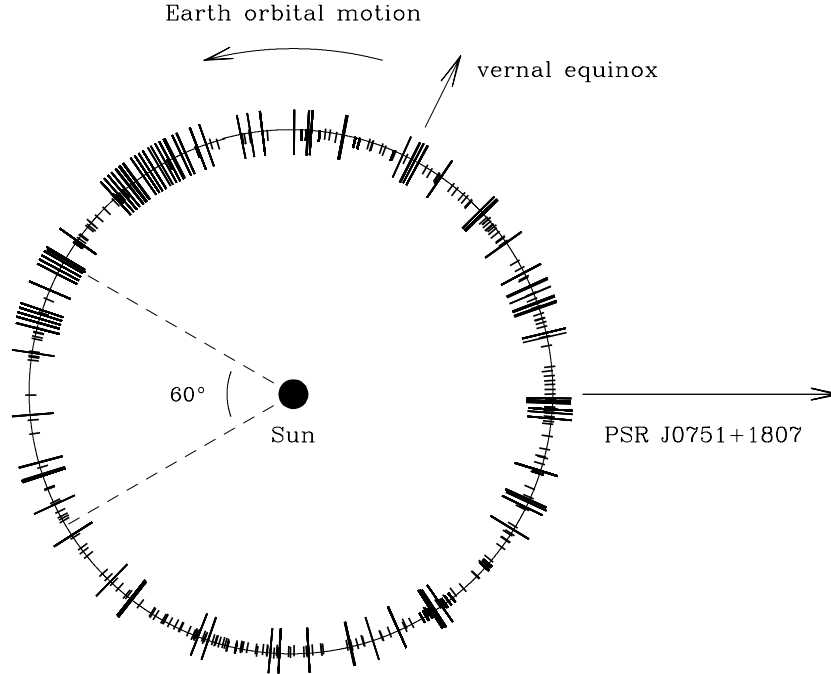
Figure 5.1: Location of PSR J0751+1807 observations with respect to the Sun. The big circle is Earth's orbit. The dashes along it stand for for the position of Earth at the different observations. Arecibo and Effelsberg, which contributed the highest-quality data, have elongated dashes. A 60-degree angle about superior conjunction shows where the solar DM would have produced the biggest delays in the TOAs.

the pulsar sits close to the plane of the solar system. At this latitude, α and δ are strongly covariant, whereas λ and β are nearly independent. A location in the plane of the solar system has observational drawbacks. One is that, at Arecibo, the source passes over the center of the dish at azimuth. The telescope must then stop tracking for about 15 minutes so that the azimuth arm can rotate by 180°. A second

disadvantage is that the pulses have to travel within the plane of the solar system to reach Earth. As they do, they pick up a substantial delay from the solar DM (§ 1.5.2). Figure 5.1 shows the configurations of Earth, the pulsar, and the Sun at each observation. The pulses cross the longest stretch of solar system at superior conjunction. There, an assumed solar electron density of $n_0 = 10\,\text{cm}^{-3}$ (the default value in TEMPO) in equation 1.10 implies a delay of $\Delta t_{\text{max}} \simeq 70\,\mu\text{s}$—significantly bigger than the TOA uncertainties. Ideally, the solar delay could be modeled out of the arrival times so that it did not influence the fit of the astrometric parameters. But the difficulty in modeling the delay is that n_0 is not known a priori, and that it varies with the solar cycle. Moreover, measuring DM variations requires high-precision TOAs in two widely spaced bands, which are expensive in telescope time and in any case difficult to obtain with existing data-acquisition equipment. Our stopgap remedy is to fit n_0 as a free parameter in the rudimentary solar electron density model $n_e(r) = n_0(1\,\text{AU}/r)^2$. We find $n_0 = 5.8 \pm 0.6\,\text{cm}^{-3}$.

5.2.2   The Laplace-Lagrange Parameters

Table 5.3 lists the orbital parameters of PSR J0751+1807. The DD timing model that we apply to other binaries (§ 1.5.3) is less satisfactory for orbits as circular as this one. When the eccentricity approaches zero, the epoch of periastron, T_0, and the longitude of periastron, ω, become highly covariant. Intuitively, this can be understood by recognizing that in a circular orbit there is no unique point of closest approach between pulsar and companion. To sidestep the covariance between T_0 and ω, we employed an extension of the DD model, called the ELL model and developed by Norbert Wex (Lange *et al.* 2001). The ELL model replaces T_0, e, and ω with

$$T_{\text{asc}} \;=\; T_0 - P_b\frac{\omega}{2\pi} \tag{5.1}$$

$$\eta \;=\; e\sin\omega \tag{5.2}$$

Table 5.3: Orbital parameters of PSR J0751+1807.[a]

Orbital period, P_b (days)	0.263144266785(10)
Projected semi-major axis, x_{obs} (observed) (lt-s)	0.396611(2)
Projected semi-major axis, x_{int} (intrinsic) (lt-s)	0.396609(4)
First Lagrange-Laplace parameter, η_{obs} (10^{-6}) (observed) . . .	$-2(3)$
First Lagrange-Laplace parameter, η_{int} (10^{-6}) (intrinsic)	$-7(7)$
Second Lagrange-Laplace parameter, κ (10^{-6})	7(9)
Eccentricity, e_{obs} (10^{-6}) (observed)	*2(3)*
Eccentricity, e_{int} (10^{-6}) (intrinsic)	*7(7)*
Time of ascending node, TASC (MJD [TDB])	50713.69305676(4)
Epoch of periastron, T_0 (MJD [TDB])	*50713.90(2)*
Longitude of periastron, ω (deg)	*288(34)*
Sine of orbital inclination angle, $\sin i$	0.96(8)
Companion mass, m_2 (M$_\odot$)	*$0.20^{+0.03}_{-0.03}$*
Pulsar mass, m_1 (M$_\odot$)	*$2.34^{+0.44}_{-0.51}$*
Total mass, M (M$_\odot$)	*$2.54^{+0.44}_{-0.51}$*
Mass function, f_1 (M$_\odot$)	*0.000967364(16)*
Orbital period derivative, $\dot{P}_b^{\mathrm{obs}}$ (10^{-14}) (observed)	$-8.1(1.8)$
Orbital period derivative, $\dot{P}_b^{\mathrm{int}}$ (10^{-14}) (intrinsic)	*$-8.4(1.8)$*

[a]Figures in parentheses are uncertainties in the last digit quoted, and italicized numbers represent quantities derived from fitted parameters.

[b]These parameters were set equal to zero when fitting the others. The listed values were obtained by allowing these extra terms to vary one at a time.

$$\kappa \;=\; e\cos\omega, \tag{5.3}$$

where T_{asc} is the epoch of the ascending node, and η and κ are the first and second Laplace-Lagrange parameters, respectively. The benefit of the transformation is that it diagonalizes the $\eta-\kappa-T_{\mathrm{asc}}$ sector of the covariance matrix. In terms of the Laplace-Lagrange parameters, the Keplerian elements are

$$e \;=\; \sqrt{\eta^2 + \kappa^2}, \tag{5.4}$$

$$\omega \;=\; \arctan\left(\frac{\eta}{\kappa}\right), \tag{5.5}$$

$$T_0 \quad = \quad T_{\text{asc}} + \frac{P_b}{2\pi} \arctan\left(\frac{\eta}{\kappa}\right). \tag{5.6}$$

Lange *et al.* (2001) point out that because the Roemer delay is indistinguishable from the Shapiro delay in a highly circular orbit, the observed values of the η (and hence e) and x differ slightly from their intrinsic values:

$$\eta_{\text{int}} \quad = \quad \eta_{\text{obs}} - 4\frac{r}{x_{\text{int}}}a_2, \tag{5.7}$$

$$x_{\text{int}} \quad = \quad x_{\text{obs}} - 2rb_1, \tag{5.8}$$

where

$$a_2 \quad = \quad 2\frac{\left(1 - \sqrt{1 - \sin^2 i}\right)}{\sin^2 i} - 1, \tag{5.9}$$

$$b_1 \quad = \quad 2\frac{\left(1 - \sqrt{1 - \sin^2 i}\right)}{\sin i}. \tag{5.10}$$

As a consequence, there is also a small discrepancy between the observed and intrinsic values of the eccentricity, e_{obs} and e_{int}. The observed and intrinsic η and x are stated in Table 5.3. LZC95 found an upper limit for the eccentricity: $e < 10^{-4}$. Even with seven more years of TOAs, we are still unable to secure a definitive measurement, although we do reduce the limit by an order of magnitude:

$$e_{\text{int}} < 1 \times 10^{-5} \, (1\sigma). \tag{5.11}$$

Pulsars with small orbital periods are expected to have very low eccentricities (Phinney and Kulkarni 1994). Future observations will determine if this pulsar has the least eccentric orbit known. The title currently belongs to PSR J1012+5307 with $e < 0.8 \times 10^{-6} \, (1\sigma)$ (Lange *et al.* 2001), followed by PSR J2317+1439 with $e < 1.2 \times 10^{-6}$ (1σ) (Camilo, Nice, and Taylor 1996).

5.2.3   Orbital Decay

Acceleration biases have only a minor effect on the observed value of $\dot{P}_b$. After subtracting them off, we find

$$\dot{P}_b^{\text{int}} = -(8.4 \pm 1.8) \times 10^{-14}\,(1\sigma). \tag{5.12}$$

This is only the second NS-WD system with a reported non-zero $\dot{P}_b$. The first was PSR J1141-6545 (Bailes *et al.* 2003). Unlike PSR J0751+1807, that system is highly eccentric (signifying that the pulsar was formed after the white dwarf) and the white dwarf is relatively massive ($m_2 \sim 1\,\mathrm{M}_\odot$). Below (§ 5.3) we examine the possibility that the observed secular change in the orbital period of PSR J0751+1807 is due to back reaction not only from quadrupolar gravitational radiation, as expected under GR, but also from monopolar and dipolar, as allowed by theories that violate the SEP. Continued observation should reduce the uncertainty of this important measurement. Damour & Taylor (1992) show that the statistical error on $\dot{P}_b$ shrinks with the timing baseline as $T^{-5/2}$. With another decade of observation, the uncertainty on $\dot{P}_b$ should go down by a factor of ten.

5.2.4   System Masses and Inclination Angle

We found m_1, m_2, and $\cos i$ following the procedure described in Appendix B. The variation of χ^2 across the grid is due not only to the orbital period derivative but also to Shapiro delay. The resulting PDFs are in Figures 5.2 a-b. They imply the maximum-likelihood estimates

$$
\begin{aligned}
m_1 &= 2.34^{+0.44}_{-0.51}\,\mathrm{M}_\odot \; (68\%\ \text{confidence}) \\
&= 2.34^{+0.88}_{-1.05}\,\mathrm{M}_\odot \; (95\%\ \text{confidence})
\end{aligned}
\tag{5.13}
$$

for the pulsar mass,

$$m_2 = 0.20^{+0.03}_{-0.03}\,\mathrm{M}_\odot \; (68\%\ \text{confidence})$$

$$= \ 0.20^{+0.05}_{-0.07} \, M_\odot \ (95\% \text{ confidence}) \tag{5.14}$$

for the companion mass, and

$$|\cos i| \ = \ 0.28^{+0.10}_{-0.08} \ (68\% \text{ confidence})$$

$$= \ 0.28^{+0.25}_{-0.15} \ (95\% \text{ confidence}) \tag{5.15}$$

for the inclination angle. The joint PDF of the two masses is in Figure 5.3, and the joint PDF of m_2 and $|\cos i|$ is in Figure 5.4.

5.2.5   Interpretation of the Masses

Our estimate of m_1 in is on the high side of known pulsar masses. Nevertheless, at 95% confidence it is consistent with the population mean of $m_1 = 1.35 \pm 0.04 \, M_\odot$ found by Thorsett & Chakrabarty (1999). Future observations of should be able to tighten the measurements of m_1 and m_2 by hammering away at the Shapiro delay. In this regard, the short binary period will prove helpful; a single observation at Arecibo sees up to 40% of the orbit during the 160-minute transit time.

We point out that it is not possible to use the $P_b - m_2$ relation to obtain an independent estimate of the companion mass as we did with PSR J1713+0747 (§ 3.5.3). The relation does not apply to binaries with $P_b \lesssim 1 \, \text{d}$, since such a small binary period would imply an impossibly small white dwarf mass. Specifically, it would imply a mass less than $m_2 \simeq 0.13 \, M_\odot$, which is the core mass of a $1 \, M_\odot$ star when its inner hydrogen is first exhausted.

Apart from the high m_1 estimate, PSR J0751+1807 fits the typical profile of a low-mass binary pulsar (LMBP) in its circular and tightly bound orbit. Ergma, Lundgren, & Cordes (1997) piece together the history of the binary and speculate about its future. Briefly, the system had a period of ~ 1 d when the giant first overflowed its Roche lobe. In the subsequent low-mass X-ray binary (LMXB) phase,
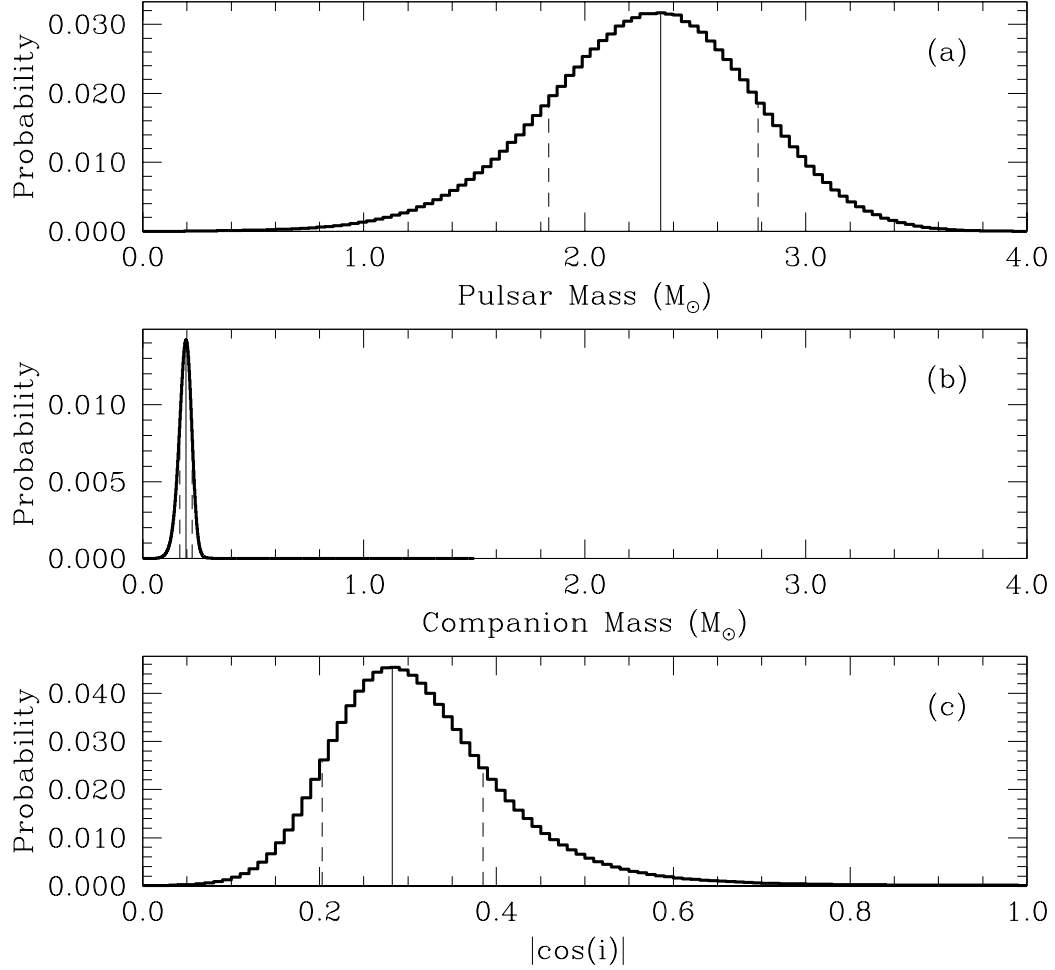
Figure 5.2: PDFs of (a) m_1, (b) m_2, and (c) $\cos i$ for the PSR J0751+1807 system. Solid vertical lines mark the maximum likelihood values. Dashed vertical lines delimit 68% confidence regions; they represent the shortest widths along the horizontal axes that both enclose the peaks and contain 68% of the area under the curves.

the pulsar was recycled into an MSP and tidal dissipation circularized the orbit. When accretion ceased and the core of the secondary remained as an He white dwarf, the binary period was about 0.35 d. It shrank to its current period of 0.26 d through emission of gravitational radiation. The orbital decay will continue for several billion
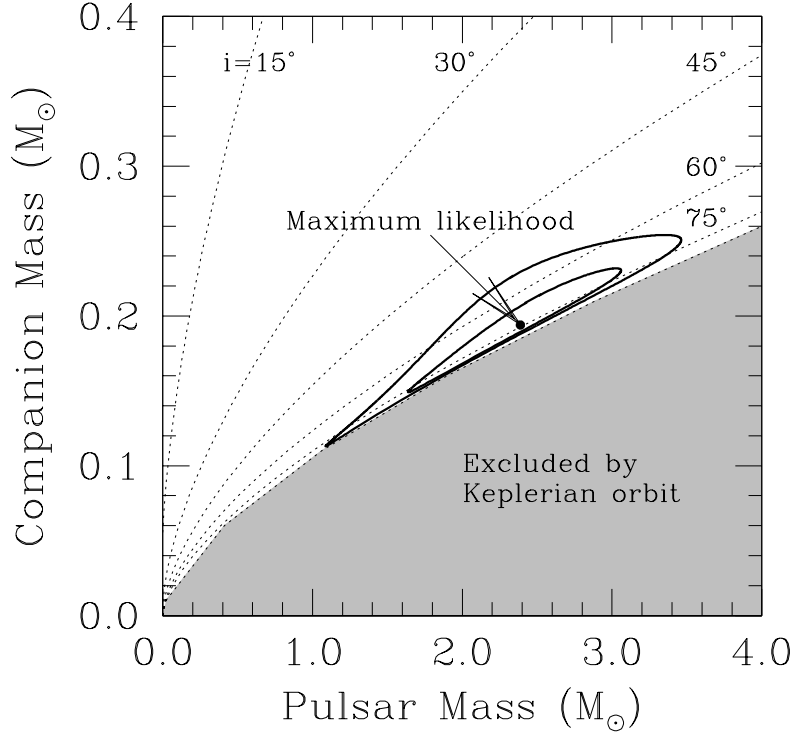
Figure 5.3: The $m_1 - m_2$ plane for the PSR J0751+1807 system. Acceptable values of the masses lie outside the shaded region, which is off-limits by the requirement that $i \leq 90°$. The inner contour is a 68% confidence region. The outer contour is a 95% confidence region. Dotted lines show constant values of orbital inclination angle i.

years more until $P_b \approx 5\,\mathrm{minutes}$, at which point the white dwarf will overflow its Roche lobe and a second LMXB phase will ensue. What happens next depends on whether the subsequent mass transfer is stable. If so, the system could linger like the ultracompact LMXB 1820-303 (Stella, Priedhorsky, and White 1987) and eventually become an isolated MSP. If not, the pulsar could plunge to the middle of the disrupted white dwarf to create a star akin to a Thorne-Żytkow object.
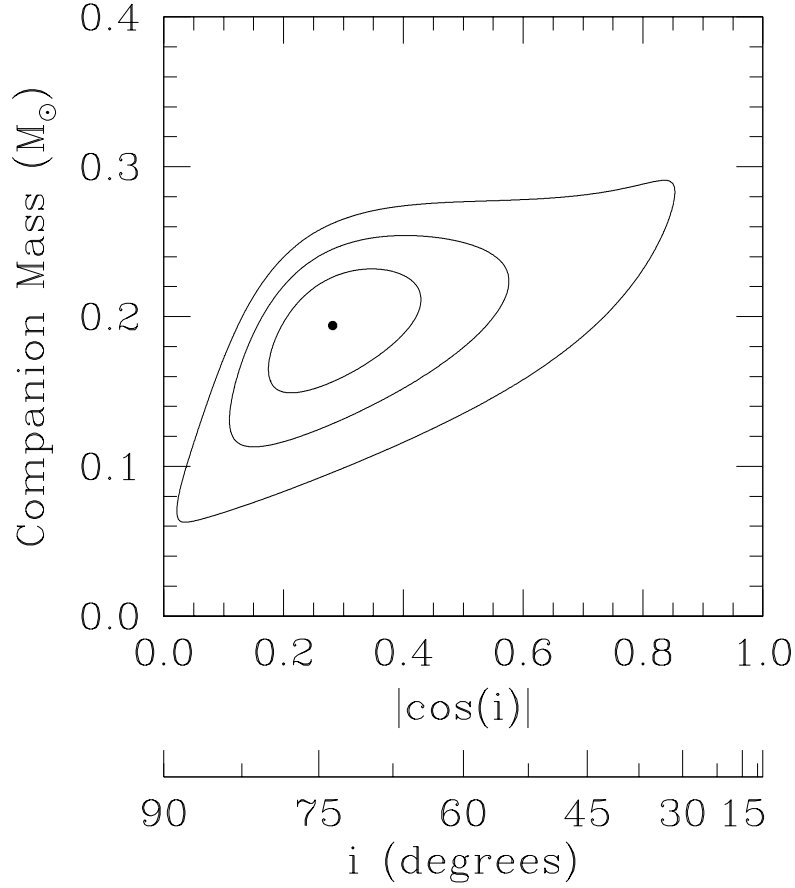
Figure 5.4: Joint PDF of m_2 and $|\cos i|$ for the PSR J0751+1807 system. The dot is the maximum-likelihood point. Contours around it represent confidence levels of 68%, 95%, and 99%.

In terms of its orbital parameters, PSR J0751+1807 resembles the eclipsing LMBPs PSR B1957+21 ($P_b = 0.38$ d) and PSR B1744-24A ($P_b = 0.075$ d). Pulsar irradiation and Roche lobe overflow are apparently evaporating the white dwarf companions of these two MSPs, raising clouds of material inside the systems that obscure the radio pulses during portions of each orbit. Both pulsars show secular changes in orbital period. For PSR B1957+20, P_b increases and decreases (Arzoumanian, Fruchter,

and Taylor 1994), while for PSR B1744-24A, P_b decreases at a rate faster than expected from quadrupolar gravitational radiation (Nice and Thorsett 1992; Nice and Thorsett 1996). The question arises: why is PSR J0751+1807 not eclipsed? Ergma, Sarna & Gerškevitš-Antipova (2001) suggest that the He white dwarf companion lost most of its outer hydrogen during an earlier phase of rapid mass loss. Consequently, present-day pulsar irradiation does not produce an extended envelope as it does for the companions of PSR B1957+21 and PSR B1744-24A.

5.3   Tests of the Strong Equivalence Principle

The measured orbital decay of system PSR B1913+16 (and of PSR B1534+12 to a lesser extent) matches the prediction of GR with famous accuracy (Stairs *et al.* 2002; Taylor and Weisberg 1989). In doing so, it confirms the existence of quadrupolar gravity waves. But this does not necessarily complete the characterization of gravitational radiation. In GR, the SEP guarantees that the lowest order of gravitational radiation is quadrupolar. But theories that violate the SEP also call for monopolar and dipolar radiation. If they exist, these two radiative channels should produce their own contributions to orbital damping. Below we review the theory and the experimental constraints on monopolar and dipolar gravitational radiation. (Our discussion draws significantly from the work of Arzoumanian 1995, 2003 on PSR B0655+64.) Then we investigate the limits that PSR J0751+1807 puts on them.

5.3.1   Monopolar Radiation

In the BD framework, monopolar radiation arises from a hypothesized time evolution of the gravitational "constant". Briefly, the theory posits a scalar field, ϕ, and replaces

the coupling constant G in the Einstein equations with the variable term $1/\phi$:

$$R^{\mu\nu} - \frac{1}{2}g^{\mu\nu}R = -\frac{8\pi}{\phi}\left(T_\phi^{\mu\nu} + T_E^{\mu\nu}\right) \tag{5.16}$$

where $T_\phi^{\mu\nu}$ and $T_E^{\mu\nu}$ are the the stress-energy tensors for the extra field and for everything else, respectively (Weinberg 1972). The strength of ϕ is governed by a dimensionless parameter, ω_{BD}. BD theory becomes indistinguishable from GR as ω_{BD} goes to infinity. It can be shown that in a universe where the mass-energy density, Ω_{total}, is unity,

$$\left(\frac{\dot{G}}{G}\right) = -\frac{1}{\omega_{BD}+2}H_0, \tag{5.17}$$

where H_0 is the Hubble constant (Weinberg 1972). ($\Omega_{\text{total}} = 1.02 \pm 0.02$ according to WMAP observations by Spergel *et al.* 2003.)

How does a time-varying G affect binary motion? Damour, Gibbons & Taylor (1988) showed that for a pair of pointlike objects with negligible self-energies,

$$\left(\frac{\dot{G}}{G}\right) = -\frac{1}{2P_b}\left(\dot{P}_b^{\text{obs}} - \dot{P}_b^{\text{pred}}\right), \tag{5.18}$$

where $\dot{P}_b^{\text{pred}}$ stands for the predicted orbital evolution due to back reaction from quadrupolar (and potentially also dipolar) radiation. Recognizing that a variation in G would cause changes in binding energies (and hence masses) that in turn would act as additional forces on the two stars, Nordtvedt (1990) revised equation 5.18 for compact objects:

$$\left(\frac{\dot{P}_b}{P_b}\right)_{\dot{G}} = -2\frac{\dot{G}}{G}\left[1 - s_1\left(1 + \frac{m_2}{2M}\right) - s_2\left(1 + \frac{m_1}{2M}\right)\right]. \tag{5.19}$$

Here, $M = m_1 + m_2$, and the dimensionless "sensitivities", s_1 and s_2, measure how a change in the gravitational constant alters the binding energies of the stars,

$$s = -\left(\frac{\partial \ln m}{\partial \ln G}\right). \tag{5.20}$$

For white dwarfs, s is negligible. For neutron stars, $0.15 < s < 0.40$ (Will and Zaglauer 1989), with bigger values occurring for "softer" equations of state. Recent

observational evidence suggests that stiff equations of state are needed (Arzoumanian 2003).

The constancy of G has been tested in a number of ways. To date, the best experimental results have come from radar ranging to the Viking lander on Mars,

$$\left(\frac{\dot{G}}{G}\right) = -(2 \pm 4) \times 10^{-12} \, \mathrm{yr}^{-1} \tag{5.21}$$

(Hellings *et al.* 1983; Reasenberg 1983). Lunar laser ranging has found $(\dot{G}/G) = (1 \pm 8) \times 10^{-12} \, \mathrm{yr}^{-1}$ (Williams, Newhall, and Dickey 1996). Thorsett (1996) derived the $(\dot{G}/G) = (-0.6 \pm 2.0) \times 10^{-12} \, \mathrm{yr}^{-1}$ by looking for time evolution of the Chandrasekhar limit in the statistical distribution of NS masses. Application of equation 5.18 yields $(\dot{G}/G) = (-9 \pm 18) \times 10^{-12} \, \mathrm{yr}^{-1}$ for PSR B1855+09 (Kaspi, Taylor, and Ryba 1994). Arzoumanian (1995) amended this to $(\dot{G}/G) = (-1.3 \pm 2.7) \times 10^{-11} \, \mathrm{yr}^{-1}$ using equation 5.19. A secular change in G should affect the moment of inertia of a pulsar and hence the time derivative of the spin period. Goldman (1990) used this fact to obtain $|\dot{G}/G| = (2.2 - 5.5) \times 10^{-11} \, \mathrm{yr}^{-1}$ from PSR B0655+64, where the variation depends on the NS equation of state.

5.3.2   Dipolar Radiation

In many SEP-violating theories, the intensity of dipolar radiation is a function of the difference in gravitational binding energies between the two orbiting bodies. As a result, dipolar radiation—even if it exists—will be hard to see in the same NS-NS systems that display quadrupolar radiation. Instead, the best place to look for it is a NS-WD system like PSR J0751+1807. In fact, we can enumerate the qualities that the perfect testing ground of dipolar radiation—the PSR B1913+16 of the NS-WD family—would have. It would be recycled, so that it had the good timing afforded by a millisecond period and low timing noise. It would be astrophysically "clean" (i.e. no eclipses). It would have a short orbital period (i.e. $P_b \lesssim 1 \, \mathrm{d}$) and an observable

$\dot{P}_b$. So that $\dot{P}_b$ was not biased by proper motion (as is the case for PSR B1534+12), the system would be located sufficiently far from Earth. It would also exist outside a globular cluster—even though they are a breeding ground for binary pulsars—to keep $\dot{P}_b$ from being contaminated by acceleration within the structure. Finally, it would have at least two measurable non-radiative PK effects (like the Shapiro terms r and s) so that the masses could be determined and used to isolate the GR contribution to $\dot{P}_b$. Unfortunately, no known NS-WD system meets all these requirements. But a few come close enough that useful limits can be placed on dipolar radiation. We review these results below.

For a circular orbit, the expected orbital decay due to emission of dipolar radiation is

$$\left(\frac{\dot{P}_b}{P_b}\right)_D = -\frac{4\pi^2 T_*}{P_b^2} \frac{m_1 m_2}{m_1 + m_2} (\alpha_1 - \alpha_2)^2 , \qquad (5.22)$$

where $T_* \equiv G_* M_\odot / c^3$, G_* is the bare gravitational constant, and α_1 and α_2 represent the coupling strengths of the pulsar and the white dwarf, respectively, to a scalar field (Damour and Esposito-Farèse 1996). (In GR, $G_* = G$, and both α_1 and α_2 are identically zero.) Arzoumanian (2003) finds that $|\dot{P}_b/P_b|_{\rm obs} < 1.0 \times 10^{-10}\,{\rm yr}^{-1}$ (2σ) for PSR B0655+64 ($P_b = 1.0\,{\rm d}$), which gives $(\alpha_1 - \alpha_2)^2 < 2.7 \times 10^{-4}\,(2\sigma)$. Likewise, Lange *et al.* (2001) detects $|\dot{P}_b/P_b|_{\rm obs} < 6.0 \times 10^{-11}\,{\rm yr}^{-1}$ for PSR J1012+5307 ($P_b = 0.6\,{\rm d}$), which leads to $(\alpha_1 - \alpha_2)^2 < 4 \times 10^{-4}\,(2\sigma)$. One candidate for future testing is the recently discovered PSR J1757-5322 ($P_b = 0.5\,{\rm d}$) (Edwards and Bailes 2001a). Another is the previously mentioned PSR J1141-6545 ($P_b = 0.2$), which is also expected to produce plentiful quadrupolar radiation owing to its large eccentricity (Gérard and Wiaux 2002; Bailes *et al.* 2003).

5.3.3   Limits on Dipolar Radiation

The intrinsic orbital decay is the sum of of contributions from quadrupolar and—if they exist—monopolar and dipolar radiation:

$$\left(\frac{\dot{P}_b}{P_b}\right)_{\text{int}} = \left(\frac{\dot{P}_b}{P_b}\right)_{\text{mono}} + \left(\frac{\dot{P}_b}{P_b}\right)_{\text{di}} + \left(\frac{\dot{P}_b}{P_b}\right)_{\text{quad}}. \tag{5.23}$$

For PSR J0751+1807, we have

$$\left(\frac{\dot{P}_b}{P_b}\right)_{\text{int}} = -(1.2 \pm 0.3) \times 10^{-10}\,\text{yr}^{-1}\,(2\sigma). \tag{5.24}$$

Knowing this, equation 5.23 can be used to get a handle on the contributions of the SEP-violating terms.

For example, it should be possible to estimate the dipolar coupling-strength term $(\alpha_1 - \alpha_2)^2$ by solving for $(\dot{P}_b/P_b)_{\text{di}}$. This would require four pieces of information. First, we would need $(\dot{G}/G)$ to calculate the monopolar term. This we could obtain from the earlier measurement in equation 5.21. Second, we would need the NS sensitivity s_1. (The white dwarf sensitivity, s_2, can be neglected.) This we could simply pick to be some reasonable figure based on nuclear theory. Finally, we would need m_1 and m_2 to be able to plug them into equation 5.19 for the monopolar contribution, equation 5.22 for the dipolar contribution (here we would assume $G_* = G$), and equation 1.25 for the quadrupolar contribution. But here is the problem. Our mass estimates in equations 5.13 and 5.14 cannot be used for this because they were derived assuming that the SEP holds; at each point in the $m2 - \cos i$ grid, a timing solution was found by ascribing all of $\dot{P}_b$ to its GR-predicted value. What we need, but lack, are masses derived independently of a specific theory of gravity. Other authors have used pulsar timing to constrain SEP violation. Where did they get their mass estimates? For PSR J1012+5307, Lange *et al.* (2001) used optical observations of the WD to determine m_2 (Lorimer *et al.* 1995) and the measured Doppler shift of the WD's H spectrum to find the mass ratio m_1/m_2 (Callanan, Garnavich, and Koester

1998). For PSR B0655+64, Arzoumanian (2003) simply assumed $m_1 = 1.4\,\mathrm{M}_\odot$ and $m_2 = 0.8\,\mathrm{M}_\odot$.

Even without theory-independent mass estimates, it is still possible to put an upper limit on the coupling-strength term of PSR J0751+1807. This is done by recognizing that if m_1, m_2, and s_1 all lie within some specified ranges, then $(\alpha_1 - \alpha_2)^2$, as a mathematical function (implicitly through eq. 5.23), is maximized by some set of values for m_1, m_2, and s_1. There are two constraints on the solution. First, the masses must agree with $m_1 \leq m_2^{3/2} f_1^{-1/2} - m_2$, which comes from setting $\sin i \leq 1$ in the Keplerian mass function (§ 1.12). Second, the lower and upper bounds of the three parameters must be astrophysically plausible in case the solution lies on an "edge" of the parameter space. If these constraints are satisfied, then the solution represents the biggest value that the coupling-strength term could be. For the ranges, we take $1.00\,\mathrm{M}_\odot < m_1 < 3.50\,\mathrm{M}_\odot$, $0.05\,\mathrm{M}_\odot < m_2 < 1.40\,\mathrm{M}_\odot$, and $0.15 < s_1 < 0.40$. We find

$$(\alpha_1 - \alpha_2)^2 < 1 \times 10^{-4}\,(2\sigma). \tag{5.25}$$

The result is within an order of magnitude of those obtained for PSR B0655+64 and PSR J1012+5307, but note that the new result employs a much more conservative approach. (The values that maximize the coupling-strength term are physically meaningless, but we provide them for completeness. They are $m_1 = 1.00\,\mathrm{M}_\odot$, $m_2 = 0.11\,\mathrm{M}_\odot$, and $s_1 = 0.39$.)

5.3.4 Constraints on the Brans-Dicke Coupling Parameter

Following Arzoumanian (2003), we also investigate the constraints that orbital decay puts on ω_{BD}. In BD theory, the monopolar, dipolar, and quadrupolar contributions to $\dot{P}_b$ are all parameterized by ω_{BD}. The formulas for a circular orbit are:

$$\left(\frac{\dot{P}_b}{P_b}\right)_{\mathrm{mono}} = 2\,\xi\,H_0\left[1 - s_1\left(1 + \frac{m_2}{2M}\right) - s_2\left(1 + \frac{m_1}{2M}\right)\right], \tag{5.26}$$

$$\left(\frac{\dot{P}_b}{P_b}\right)_{\mathrm{di}} = -\kappa_{\mathrm{D}}\mathcal{G}^{-2}\left(s_1 - s_2\right)^2 \frac{m_1 m_2}{M} \left(\frac{2\pi}{P_b}\right)^2 T_\odot, \tag{5.27}$$

$$\left(\frac{\dot{P}_b}{P_b}\right)_{\mathrm{quad}} = -\frac{96}{5}\mathcal{G}^{-4/3}\left(\frac{\kappa_1}{12}\right) m_1 m_2 M^{-1/3} \left(\frac{2\pi}{P_b}\right)^{8/3} T_\odot^{5/3}, \tag{5.28}$$

where

$$\kappa_1 = 12 - 5\,\xi, \tag{5.29}$$

$$\kappa_D = 2\mathcal{G}^2\xi, \tag{5.30}$$

$$\mathcal{G} = 1 - \xi\left(s_1 + s_2 - 2s_1 s_2\right), \tag{5.31}$$

$$\xi = \frac{1}{\omega_{BD} + 2} \tag{5.32}$$

are dimensionless parameters (Arzoumanian 1995; Will 1993; Goldman 1992). There are a few things to point out here. First, the monopolar term differs in sign from the dipolar and quadrupolar terms. In BD theory, the expected decrease in G actually elongates the orbital period while emission of dipolar and quadrupolar radiation shortens it. Second, the dipolar expression is an instance of the more general equation 5.22 for the particular tensor-scalar theory of BD. Lastly, the BD scalar field makes it own contribution to quadrupolar decay, which is why equation 5.28 differs from the GR expression (with $e = 0$) in equation 1.25. The three BD expressions reduce to GR as $\xi = 0$, $\kappa_D = 0$, $\kappa_1 = 12$, and $\mathcal{G} = 1$. In that case, the monopolar and dipolar terms vanish.

Figure 5.5 illustrates the constraints on ω_{BD} from PSR J0751+1807. The horizontal lines show the intrinsic measurement of $(\dot{P}_b/P_b)$. The upward sloping curves describe the expected contribution of gravitational radiation through quadrupolar order as a function of ω_{BD} (eqns. 5.26-5.28). The dashed and dotted lines stand for "soft" and "stiff" NS equations of state, respectively. For each value of s_1, a trio of lines signifies the assumed (m_1, m_2) pairs $(2.00\,\mathrm{M}_\odot, 0.17\,\mathrm{M}_\odot)$, $(2.30\,\mathrm{M}_\odot, 0.20\,\mathrm{M}_\odot)$, and $(2.60\,\mathrm{M}_\odot, 0.23\,\mathrm{M}_\odot)$, with the total system mass increasing to the upper left. The
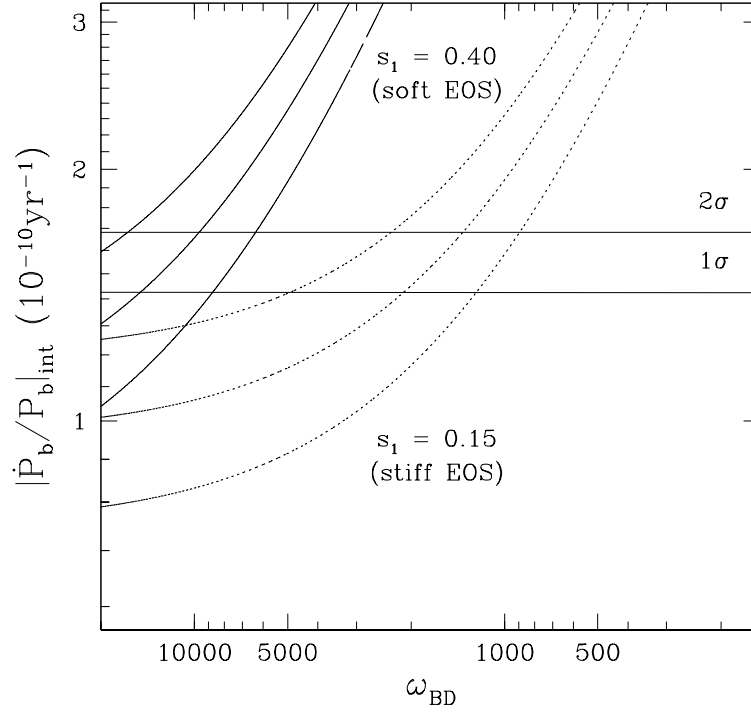
Figure 5.5: Constraints on the Brans-Dicke coupling parameter ω_{BD} from PSR J0751+1807 (cf. Will & Zaglauer 1989, Arzoumanian 2003). See text, § 5.3.4.

lower limits on ω_{BD} lie at the intersections of the curved and straight lines for a given set of assumed m_1, m_2, and s_1.

The most conservative bound from PSR J0751+1807, $\omega_{BD} \gtrsim 900$, comes from the case of $s_1 = 0.15$ and the smallest of the three system masses. This is comparable to the limit of $\omega_{BD} \gtrsim 570$ obtained by assuming $s_1 = 0.15$ for PSR B0655+64 (Arzoumanian 2003). In other experiments, Viking radar ranging to Mars found

$\omega_{BD} \gtrsim 500$ (Reasenberg *et al.* 1979), and lunar laser ranging set the bound $\omega_{BD} \gtrsim$ 1000 (see Will 2001 for a review). By far the best limit comes from radio ranging of the Cassini space probe (Bertotti, Iess, and Tortora 2003). In that experiment, the item that was actually measured was the parameterized post-Newtonian (PPN) term $\gamma - 1$, whose divergence from zero quantifies how much gravity is affected by fields other than the metric tensor (in GR, $\gamma - 1 = 0$). The term is connected to the BD parameter via

$$\gamma = \frac{1 + \omega_{BD}}{2 + \omega_{BD}}. \tag{5.33}$$

The measurement of $\gamma - 1 = (2.1 \pm 2.3) \times 10^{-5}$ gives a limit of $\omega_{BD} > 40000$.

Chapter 6

Three MSPs: B1855+09, J2033+1734, and J2322+2057

These last three MSPs are grouped together in a single chapter because there is less that is new about them. PSR B1855+09 has been investigated in earlier papers. The TOAs we add to its already sizeable data set do not uncover new timing parameters or significantly alter those already published. The same is true of PSR J2322+2025. While the timing solution we obtain for PSR J2033+1734 marks a dramatic improvement over the rudimentary parameters released upon its discovery (Ray *et al.* 1996), we do not detect any PK orbital effects in what is still a comparatively limited set of TOAs. For now, the object remains a generic low-mass binary pulsar (LMBP), one of roughly 40 currently known.

6.1   PSR B1855+09

PSR B1855+09 is one of the most thoroughly studied of the MSPs, and not just because it was the third one discovered (after PSRs B1937+21 and B1953+29). The system has a nearly edge-on orbital inclination ($i = 87°$), which allows the masses to

be determined through a Shapiro delay that increases sharply near superior conjunction. Moreover, a detectable parallax makes the pulsar one of the few whose distance can be established through timing. Finally, the exceptional stability of its signal gives the pulsar a role in timing-array experiments.

The object was found by Segelstein *et al.* (1986) during an MSP survey at Arecibo. Shortly afterward, Rawley, Taylor & Davis (1988) produced tight estimates of its celestial coordinates, spin, and Keplerian orbital parameters. Ryba & Taylor (1990) measured its proper motion and Shapiro delay. Stinebring *et al.* (1990) used the postfit timing residuals to obtain a significant limit on the density of cosmic gravitational background radiation. Kaspi, Taylor, & Ryba (1994, hereafter KTR94) refined the timing model further, detecting parallax. They also improved the limits on the gravity-wave background. Thorsett & Dewey (1996) re-analyzed the statistics of the background limits. Most recently, Lommen & Backer (2001) searched the residuals for the periodic signal of gravitational radiation from a theorized massive black hole binary in Sagittarius A*.

6.1.1   Observations

The Princeton Pulsar Group has observed PSR B1855+09 at Arecibo continually since 1986, except during the 1994–1998 upgrade. The 408 average TOAs are summarized in Table 6.1. A succession of instruments took the data. Briefly, the first system was Mark II, a dual-polarization 32×0.25 MHz filterbank spectrometer. Centered at an observing frequency of 1408 MHz, the system measured pulse arrival times biweekly between 1986 January and 1990 January (Rawley 1986; Rawley, Taylor, and Davis 1988). Its successor, Mark III, used the same filterbank and, simultaneously, a second one with a wider bandwidth of 32×1.25 MHz. The TOAs that Mark III collected between 1989 January and 1992 December at 1408 MHz have already been

Table 6.1: Summary of Arecibo Observations of PSR B1855+09

System	Dates	Frequency (MHz)	Bandwidth (MHz)	Number of TOAs	Typical Integration (min)	RMS Residual[a] (μs)
Mark II	1986.0–1990.0	1408	32×0.25	75	50	1.6
Mark III	1989.0–1994.1	1408	32×0.25	115	50	1.2
	1989.0–1994.1	1408	32×1.25	119	50	0.88
	1998.5–1998.6	1408	32×0.25	9	90	1.0
	1998.6–1998.6	1408	32×1.25	10	90	0.88
Mark IV	1999.4–2003.0	430	5	22	29	2.6
	1998.5–2003.0	1410	10	53	58	1.6
	1997.7–2002.2	2380	10	5	29	1.7

[a]Values incorporate the effect of averaging TOAs from shorter integration times.

analyzed by KTR94. Added here are Mark III TOAs taken between 1993 January and 1994 January in the continuation of the same biweekly timing project, as well as a set of post-upgrade points acquired in 1998 July. The fourth-generation Princeton backend, Mark IV, observed the pulsar once a month between 1998 September and 2002 December for up to an hour at 1410 MHz. On the same days, a further half hour was spent at 2380 MHz (between 1999 September and 2000 March) or at 430 MHz (between 2000 November and 2002 December). For 13 days in 1998 July, the observations were extended to 1.5 hrs at 1410 MHz to heighten sensitivity to relativistic orbital effects. In all cases, Mark IV scans were subdivided into 190-second integrations out of which profiles were constructed with 4096 bins at 1410 MHz (see Fig. 1.2) and 1024 bins at 430 and 2380 MHz.

The 32×0.25 MHz Mark II and Mark III filterbanks were able to boost the received strength of the pulsar signal by taking advantage of diffractive scintillation, which focuses radio flux into narrow frequency bands of characteristic width and timescale. The effect is analogous to that of "shower-door glass," through which light appears

brighter at some angles than others. In the ISM, diffractive scintillation results from motion relative to an interference pattern created by multi-path scattering through inhomogeneities in electron density. For PSR B1855+09 at 1410 MHz, scintillation has a mean bandwidth of $\Delta\nu_s = 4.8 \pm 0.5$ MHz and a mean duration of $\Delta\tau_s = 33 \pm 4$ min (Ryba 1991). By tuning each day to the central observing frequency in the range 1380–1425 MHz at which the pulsar signal was strongest, Mark II and Mark III were able to raise the signal-to-noise ratio of their integrated pulse profiles and hence raise the quality of their TOAs. For Mark IV, on the other hand, observing in conjunction with other universities made "scintle hunting" impractical, and so the observing frequency was held at 1410 MHz almost every month. Only by chance, then, did Mark IV hit upon a scintillation maximum. On many days it faced a weak signal.

The consequences of the two observing styles—roving and stationary observing frequencies—are apparent in the RMS timing residuals in Table 6.1. The 32 × 0.25 MHz Mark II and Mark III filterbanks have drawbacks in comparison with Mark IV. They have slightly narrower bandwidths than Mark IV. The time constants in the analog detector circuits of each channel can drift from their advertised values. The combination of residual dispersion smearing in the channels and scintillation (which makes the signal stronger at one end or the other of the bandpass) can bias timing. Yet despite these disadvantages, these filterbanks have RMS residuals equal to or smaller than Mark IV at 1410 MHz. (The Mark III 32 × 1.25 MHz filterbank did not shift center frequency; its superior RMS residual is a consequence of its bigger bandwidth.)
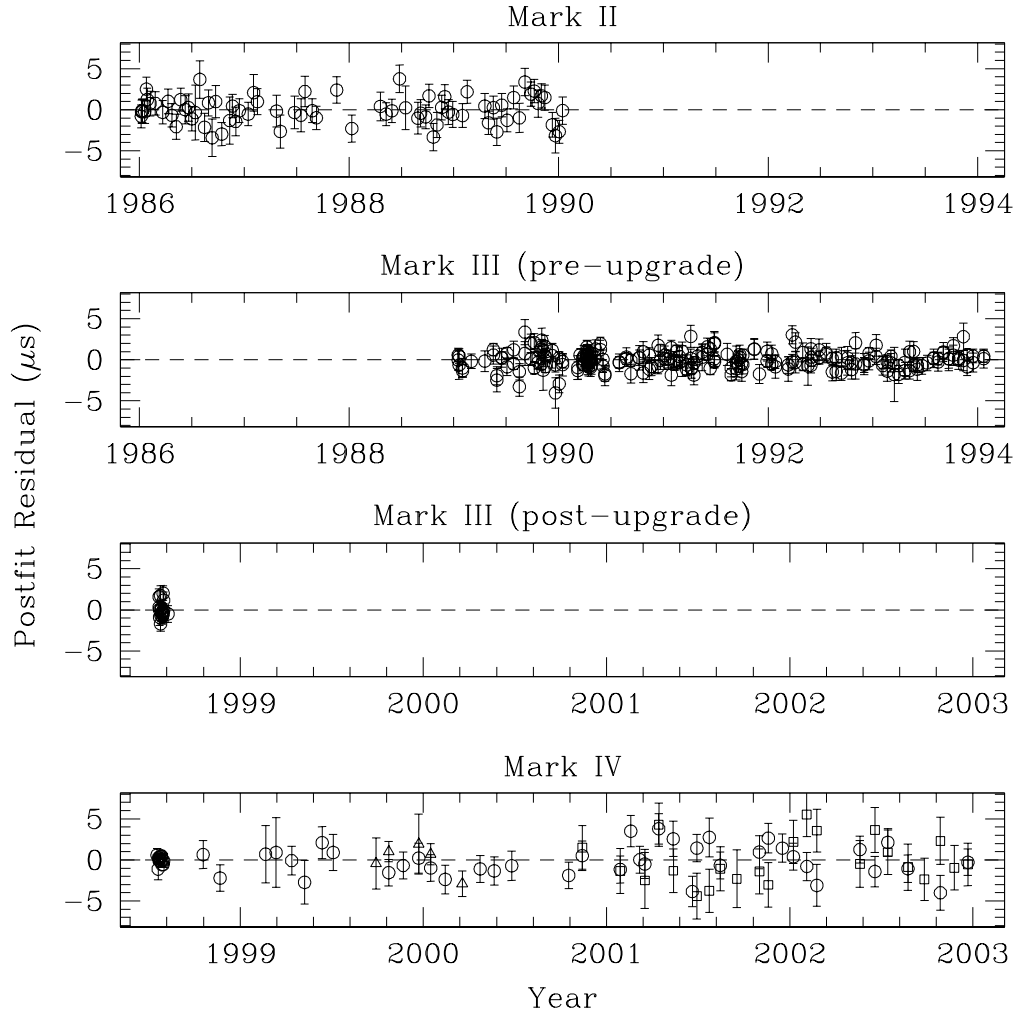
Figure 6.1: Postfit residuals of PSR B1855+09, divided by data-acquisition system. The four-year gap between the top two and bottom two panels is due to a shutdown of the Arecibo observatory. Vertical bars are uncertainties in the TOAs. Squares, circles, and triangles indicate observing frequencies of 430, 1410, and 2380 MHz, respectively.

6.1.2   Timing Results

The postfit residuals, illustrating both the quality of the fit and the epochs spanned by the different observing systems, appear in Figure 6.1. Before we added different amounts of error in quadrature to the statistical uncertainties of the TOA sets in

Table 6.1, the goodness-of-fit statistic of the original fit was $\chi^2/\nu = 7.9$, where $\nu = 380$ is the number of degrees of freedom. The listed parameters agree with the most recently published set, that of KTR94, whose data, ending in 1992, comprise a large portion of ours. Our uncertainties are generally 20-40% smaller than theirs, even if we multiply ours by a conservative factor of 1.3, as they do. The one difference is that, by introducing multi-frequency TOAs, we detect a moderately significant rate of change in DM.

Table 6.2 lists astrometric and spin parameters of PSR B1855+09, and Table 6.3 lists orbital parameters. Even though standard electromagnetic theory predicts that all but the first derivative of spin frequency should be negligibly small, derivatives through fourth order were needed fully to whiten the postfit residuals. Each extra derivative brings about a significant reduction in χ^2. We retained the extra derivatives in the fit with all the other parameters. In doing so, we broke with the practice of KTR94. To avoid biasing measurements of the basic rotational parameters ν and $\dot{\nu}$, they fit for spin derivatives higher than the first, but then reset them to zero and held the orbital and astrometric parameters constant in a second fit for ν and $\dot{\nu}$ alone. Finally, they measured $\ddot{\nu}$ by allowing it to vary in a third fit. In practice, the difference in the way we and KTR94 handle the higher spin derivatives amounts to discrepancies in ν and $\dot{\nu}$ of no more than a few times the measurement uncertainties.

As with PSR J1713+0747 (§ 3.3), the parallax measured of PSR B1855+09 is sensitive to how the solar system electron density is parametrized. Using the model in equation 1.10 and treating n_0 as a free parameter as before, we find the best-fit value $n_0 = 15 \pm 5\,\mathrm{cm}^{-3}$. The parallax then becomes $\pi = 1.4 \pm 0.3\,\mathrm{mas}$, leading to a distance estimate of $d = 1/\pi = 0.72^{+0.17}_{-0.11}\,\mathrm{kpc}$.

By subtracting off biases induced by differential Galactic accelerations, we compute the intrinsic value of the spin period derivative (§ 3.4.4). Because PSR B1855+09

Table 6.2: Astrometric and spin parameters of PSR B1855+09^a.

Right ascension, α (J2000).............................	$18^h57^m36\overset{s}{.}392433(4)$
Declination, δ (J2000)	$+09°43'17\overset{''}{.}29381(9)$
Proper motion in R.A., $\mu_\alpha = \dot\alpha\cos\delta$ (mas yr^{-1})........	$-2.899(13)$
Proper motion in Dec., $\mu_\delta = \dot\delta$ (mas yr^{-1})..............	$-5.45(2)$
Parallax, π (mas).....................................	$1.4(3)$
Distance, d (kpc)......................................	$0.73^{+0.17}_{-0.11}$
Composite proper motion, μ (mas yr^{-1})...............	$6.173(19)$
Galactic longitude, l (deg)	42.2903
Galactic latitude, b (deg)	3.0604
Position angle of μ in equatorial coordinates, ϕ (deg)...	$208.01(14)$
Position angle of μ in Galactic coordinates, ϕ (deg)	$270.65(14)$
Pulse period, P (ms)	$5.36210045713471(4)$
Period derivative (observed), $\dot P_{\mathrm{obs}}$ (10^{-20})	$1.78354(4)$
Period derivative (intrinsic), $\dot P_{\mathrm{int}}$ (10^{-20})	$1.747(8)$
Frequency, ν (Hz)	$186.4940815626493(12)$
First derivative of ν, $\dot\nu$ ($10^{-16}\,\mathrm{s}^{-2}$).....................	$-6.20318(13)$
Second derivative of ν, $\ddot\nu$ ($10^{-28}\,\mathrm{s}^{-3}$)	$8(2)$
Third derivative of ν, $\dddot\nu$ ($10^{-35}\,\mathrm{s}^{-4}$)	$-1.2(2)$
Fourth derivative of ν, $\nu^{(4)}$ ($10^{-43}\,\mathrm{s}^{-5}$)	$-3.0(5)$
Epoch (MJD [TDB])...................................	49533.0
Dispersion measure, DM (pc cm^{-3})	$13.2957(4)^b$
First derivative of DM, $d\mathrm{DM}/dt$ (10^{-4} pc cm^{-3} yr^{-1})....	$-2.2(5)$
Characteristic age, τ (Gyr)	$4.876(2)$
Surface magnetic field strength, B_0 (G)	$3.194(8)\times10^8$

^{a}Figures in parentheses are uncertainties in the last digit quoted, and italicized numbers represent quantities derived from fitted parameters.

^{b}The quoted uncertainty is a formal estimate from the parameter fit and probably understates the true uncertainty.

Table 6.3: Orbital parameters of PSR B1855+09.[a]

Orbital period, P_b (days)	12.32717119077(14)
Projected semi-major axis, x (lt-s)	9.2307799(2)
Eccentricity, e	0.00002170(3)
Epoch of periastron, T_0 (MJD [TDB])	49539.2255(14)
Longitude of periastron, ω (deg)	276.39(4)
Sine of orbital inclination angle, $\sin i$	0.9989(3)
Companion mass, m_2 (M$_\odot$)	$0.267^{+0.010}_{-0.014}$
Pulsar mass, m_1 (M$_\odot$)	$1.580^{+0.102}_{-0.125}$
Total mass, M (M$_\odot$)	$1.847^{+0.102}_{-0.126}$
Mass function, f_1 (M$_\odot$)	*0.0055573923(4)*
Rate of change of periastron, $\dot{\omega}$ (10^{-3} deg yr^{-1}) . . .	-7 ± 11[b]
Orbital period derivative, $\dot{P}_b$ (10^{-13})	3 ± 2[b]
Eccentricity derivative, $\dot{e}$ (10^{-16} s^{-1})	1.6 ± 1.4[b]
Projected periastron derivative, $\dot{x}$ (10^{-16})	8 ± 6[b]

[a]Figures in parentheses are uncertainties in the last digit quoted, and italicized numbers represent quantities derived from fitted parameters.

[b]These parameters were set equal to zero when fitting the others. The listed values were obtained by allowing these extra terms to vary one at a time.

is located at a moderate distance from Earth and at a small Galactic scale height ($z = d \sin b = 0.04$ kpc), its accelerations are minor, and $\dot{P}_{\text{int}}$ differs from $\dot{P}_{\text{obs}}$ by just 2%. We calculate the characteristic age of the pulsar to be $\tau = P/2\dot{P}_{\text{int}} = 4.874 \pm 0.018$ Gyr. For comparison, van Kerkwijk *et al.* (2000) made optical measurements of the pulsar's white dwarf companion to obtain its cooling age. The cooling age should equal the pulsar age if the white dwarf formed at the same time that the pulsar was spun up to an MSP. The derivation of the cooling age from optical data depends on the unknown size of the hydrogen layer surrounding the helium core of the dwarf; the thicker the layer, the longer the element burns, and therefore the older the star is for an observed temperature. If a thin layer (10^{-6} M$_\odot$) is assumed, the cooling age is ~ 3 Gyr, while if a thick layer (10^{-3} M$_\odot$) is assumed, the cooling age becomes ~ 10 Gyr.

Under GR, the Shapiro delay measurement yields m_2 and $\cos i$, and hence m_1. To
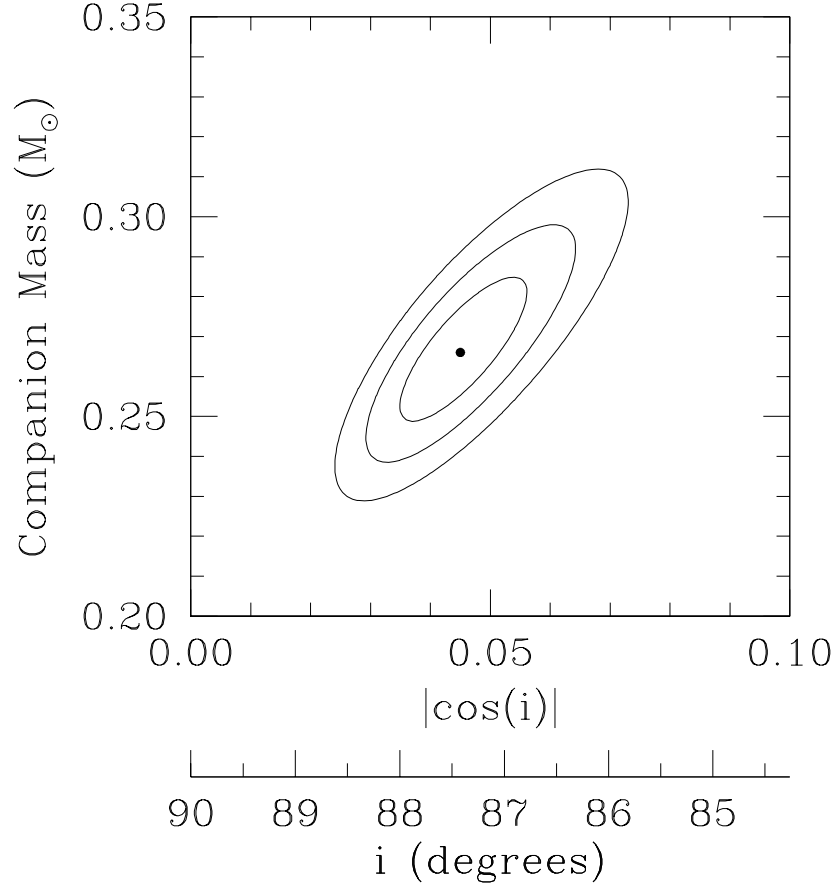
Figure 6.2: Joint PDF of m_2 and $|\cos i|$ for the PSR B1855+09 system. The dot is the maximum-likelihood point. Contours around it represent confidence levels of 68%, 95%, and 99%.

examine covariances among the three terms, we followed the statistical procedure in Appendix B and obtained the joint PDF of $\cos i$ and m_2 in Figure 6.2 and the joint PDF of m_1 and m_2 in Figure 6.3. We also constructed the individual PDFs of the three parameters in Figure 6.4. These lead to the maximum-likelihood estimates

$$
\begin{aligned}
m_1 &= 1.58^{+0.10}_{-0.13} \, \mathrm{M_\odot} \; (68\% \text{ confidence}) \\
&= 1.58^{+0.23}_{-0.22} \, \mathrm{M_\odot} \; (95\% \text{ confidence})
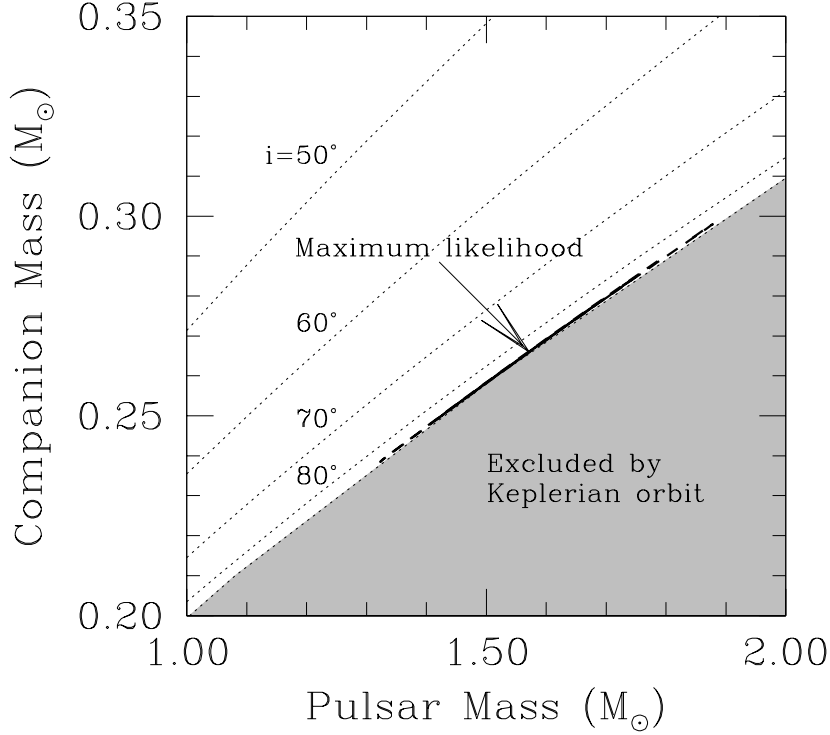\end{aligned}
\tag{6.1}
$$

Figure 6.3: The $m_1 - m_2$ plane for the PSR B1855+09 system. Acceptable values of the masses lie outside the shaded region, which is off-limits by the requirement that $i \leq 90°$. The heavy contour is a 68% confidence elliptical contour. Its dashed extension is a 95% confidence region. (Because of their extreme narrowness, the ellipsed appear to they eye as lines.) Dotted lines show constant values of orbital inclination angle i.

for the pulsar mass,

$$m_2 = 0.267^{+0.010}_{-0.014} \, M_\odot \; (68\% \text{ confidence})$$

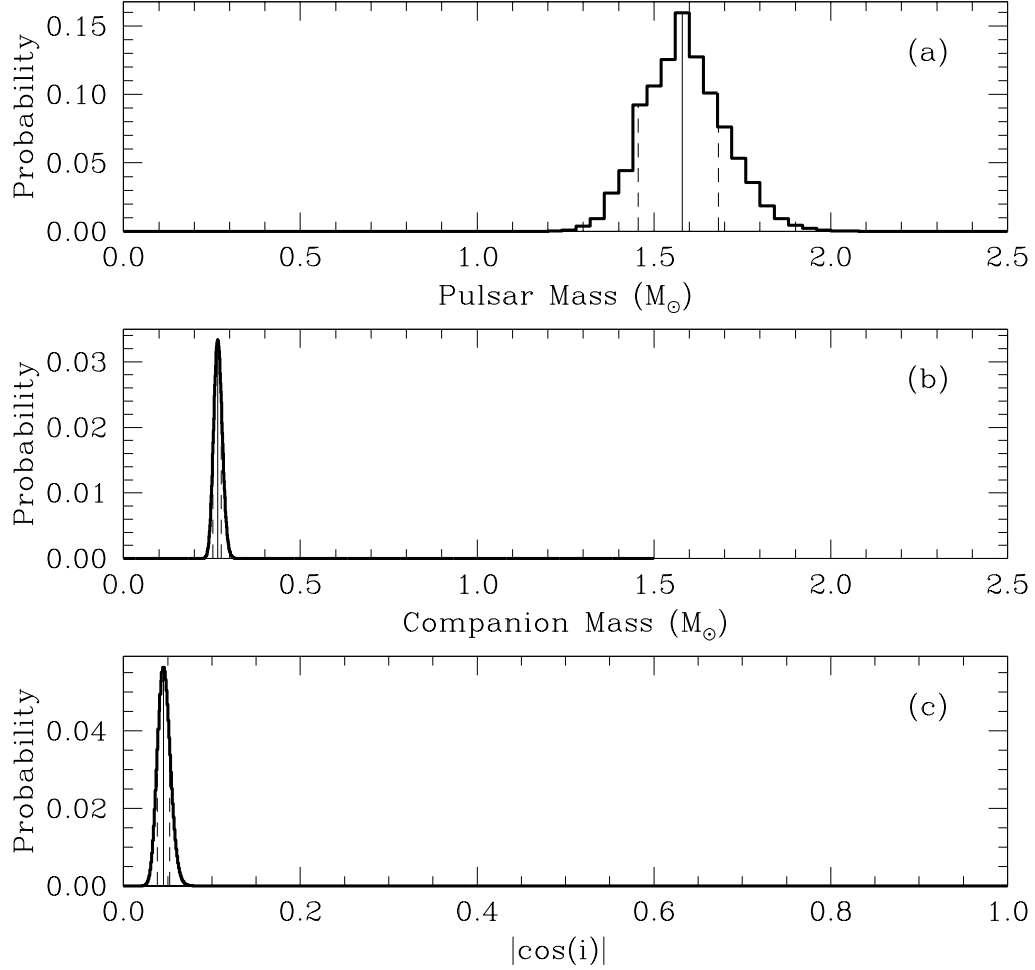$$= 0.267^{+0.022}_{-0.025} \, M_\odot \; (95\% \text{ confidence}) \tag{6.2}$$

Figure 6.4: PDFs of (a) m_1, (b) m_2, and (c) $\cos i$ for the PSR B1855+09 system. Solid vertical lines mark the maximum likelihood values. Dashed vertical lines delimit 68% confidence regions; they represent the shortest widths along the horizontal axes that both enclose the peaks and contain 68% of the area under the curves.

for the companion mass, and

$$|\cos i| = 0.0450^{+0.0072}_{-0.0070} \text{ (68\% confidence)}$$

$$= 0.0450^{+0.0154}_{-0.0130} \text{ (95\% confidence)} \qquad (6.3)$$

for the orbital inclination angle. The mass of the He white dwarf agrees well with the

Table 6.4: Summary of Observations of PSR J2033+1734

Observatory	Dates	Frequency (MHz)	Bandwidth (MHz)	Number of TOAs	Typical Integration (min)	RMS Residual[a] (μs)
Green Bank	1995.5–1999.0	370	40	60	50	12
	1995.7–1999.5	575	40	29	40	17
	1995.7–1999.5	800	40	22	40	18
Arecibo	1997.9–2003.0	430	5	34	29	1.7

[a]Values incorporate the effect of averaging TOAs from shorter integration times.

$P_b - m_2$ relation of Tauris & Savonije (1999), as indicated by Figure 3.8.

6.2   PSR J2033+1734

The timing parameters of PSR J2033+1734 have not been updated in the literature since Ray *et al.* (1996) discovered the object during a drift search at Arecibo. With 7.5 years of data, we dramatically improve the parameters. We determining the spin period and proper motion for the first time, and we obtain precise numbers for all five Keplerian orbital elements. Unlike the other binaries investigated in this thesis, PSR J2033+1734 reveals no relativistic effects in its TOAs. Without them, our estimates of the system masses must necessarily be broad and statistical in nature.

6.2.1   Observations

Table 6.4 summarized the 145 average TOAs that the Green Bank and Arecibo radio observatories acquired of PSR J2033+1734. At Green Bank, the 140 Foot (43 m) telescope observed the pulsar for 30–60 minutes a day at 370, 575, or 800 MHz (for a description of the signal-processing system used, see § 4.2). The Green Bank TOAs
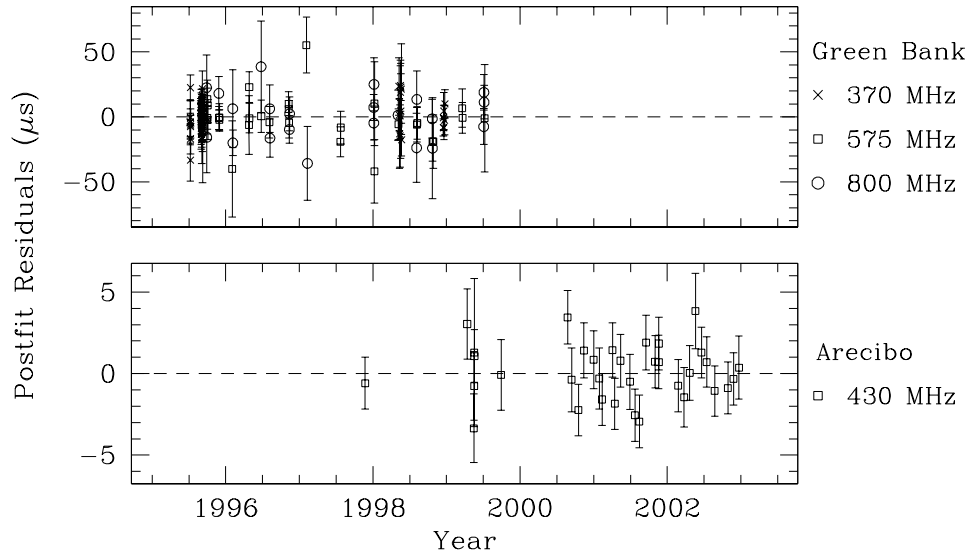
Figure 6.5: Postfit residuals of PSR J2033+1734, divided by observatory. Note the different vertical scales, emphasizing the higher precision of the Arecibo data. Vertical bars are uncertainties in the TOAs.

were taken in observations of 2–4 days spaced irregularly (typically every two months from 1995 May to 1999 July) and in three weeklong campaigns in 1995 September, 1998 May, and 1998 December. At Arecibo, the Mark IV system, operating at 430 MHz, sporadically took TOAs in 1997 and 1999 and carried out monthly observations between 2000 August and 2002 December.

6.2.2 Timing Results

Table 6.5 lists astrometric and spin parameters of PSR J2033+1734, and Table 6.6 lists orbital parameters. Before we re-weighted the statistical uncertainties in each of the data sets in Table 6.4, the goodness-of-fit statistic in the original fit was $\chi^2/\nu = 3.1$, where $\nu = 132$ is the number of degrees of freedom. Derivatives of spin frequency through fourth order were also needed to optimize the fit. The postfit residuals are shown in Figure 6.5.

Table 6.5: Astrometric and spin parameters of PSR J2033+1734[a].

Right ascension, α (J2000)	$20^{\mathrm{h}}33^{\mathrm{m}}27{.}^{\mathrm{s}}51720(3)$
Declination, δ (J2000)	$+17°34'58{.}''6380(8)$
Proper motion in R.A., $\mu_\alpha = \dot{\alpha}\cos\delta$ (mas yr^{-1})	$-5.94(17)$
Proper motion in Dec., $\mu_\delta = \dot{\delta}$ (mas yr^{-1})	$-11.0(3)$
Composite proper motion, μ (mas yr^{-1})	*12.5(3)*
Galactic longitude, l (deg)	*60.8567*
Galactic latitude, b (deg)	*−13.1542*
Position angle of μ in equatorial coordinates, ϕ (deg)	*208.3(10)*
Position angle of μ in Galactic coordinates, ϕ (deg)	*263.4(10)*
Pulse period, P (ms)	$5.9489575348501(5)$
Period derivative (observed), $\dot{P}_{\mathrm{obs}}$ (10^{-20})	$1.1112(8)$
Period derivative (intrinsic), $\dot{P}_{\mathrm{int}}$ (10^{-20})	*0.75(7)*
Frequency, ν (Hz)	$168.096678139288(15)$
First derivative of ν, $\dot{\nu}$ ($10^{-16}\,\mathrm{s}^{-2}$)	$-3.140(2)$
Second derivative of ν, $\ddot{\nu}$ ($10^{-26}\,\mathrm{s}^{-3}$)	$-5.1(10)$
Third derivative of ν, $\dddot{\nu}$ ($10^{-34}\,\mathrm{s}^{-4}$)	$-6(2)$
Fourth derivative of ν, $\nu^{(4)}$ ($10^{-41}\,\mathrm{s}^{-5}$)	$4.9(13)$
Epoch (MJD [TDB])	51268.0
Dispersion measure, DM (pc cm^{-3})	$25.0791(3)$[b]
First derivative of DM, $d\mathrm{DM}/dt$ (pc cm^{-3} yr^{-1})	$0.00067(11)$
Distance, d (kpc)	*2.0(3)*[c]
Characteristic age, τ (Gyr)	*12.6(11)*
Surface magnetic field strength, B_0 (G)	*2.20(10)* $\times\,10^8$

[a]Figures in parentheses are uncertainties in the last digit quoted, and italicized numbers represent quantities derived from fitted parameters.

[b]The quoted uncertainty is a formal estimate from the parameter fit and probably understates the true uncertainty.

[c]Distance is derived from DM using the NE2001 model of Cordes & Lazio (2002).

Table 6.6: Orbital parameters of PSR J2033+1734.[a]

Orbital period, P_b (days)	56.30779527(3)
Projected semi-major axis, x (lt-s)	20.1631191(4)
Eccentricity, e	0.00012876(6)
Epoch of periastron, T_0 (MJD [TDB]). . .	51285.842(4)
Longitude of periastron, ω (deg)	78.23(3)
Mass function, f_1 (M$_\odot$)	*0.0027759959(2)*

[a]Figures in parenthesis are uncertainties in the last digit quoted, and
italicized numbers represent quantities derived from fitted parameters.
[b]Companion mass estimated from $P_b - m_2$ relation of Tauris & Savonije (1999).

Given the DM, the NE2001 model of Galactic electron density (Cordes & Lazio 2002; see § 3.4.2) predicts the distance to the pulsar to be 2.0 ± 0.3 kpc. The distance, in turn, combines with the magnitude of proper motion, $\mu = (\mu_\alpha^2 + \mu_\delta^2)^{1/2} = 12.6 \pm 0.3$ mas yr^{-1}, to give the transverse speed of the pulsar, $V = \mu d = 120 \pm 20$ km s^{-1}, which is moderately fast for an MSP (§ 3.4.3). Besides calculating velocity, we also use the distance to correct the observed spin period derivative for biases caused by differential accelerations (§ 3.4.4). As Table 6.5 shows, the intrinsic value, $\dot{P}_{\rm int}$, is a factor of ~ 0.7 smaller than the observed value, $\dot{P}_{\rm obs}$, a difference attributable mainly to proper motion bias.

The wide orbit ($P_b = 56.3$ d) and small eccentricity ($e = 1.3 \times 10^{-4}$) of the PSR J2033+1734 system imply that the neutron star and its companion underwent an episode of stable mass transfer that circularized the orbit and left a low-mass white dwarf to orbit the spun-up MSP. The $P_b - m_2$ relation applies to such a system (§ 3.5.3). Using the formula of Tauris & Savonije (1999) (eqn. 3.29 for Pop. I+II stars), the companion mass is predicted to fall within the range $0.302\,{\rm M}_\odot \leq m_2 \leq 0.334\,{\rm M}_\odot$, with a median value of $m_2 = 0.318\,{\rm M}_\odot$. The upper limit on m_2, together with the Keplerian mass function (eqn. 1.12), then leads to an upper limit on the
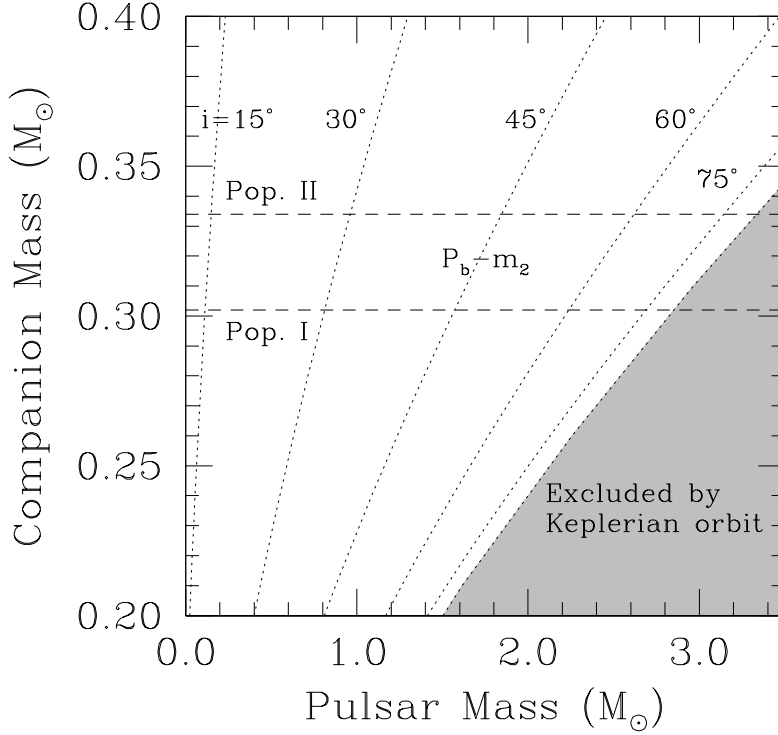
Figure 6.6: The $m_1 - m_2$ plane for the PSR J2033+1734 system. Acceptable values of the masses lie outside the shaded region, which is off-limits by the requirement $i \leq 90°$. The dashed region contains values of m_2 permitted by the $P_b - m_2$ relation of Tauris & Savonije (1999). Dotted lines show constant values of orbital inclination angle i.

pulsar mass,

$$m_1 = f_1^{-1/2}(m_2 \sin i)^{3/2} - m_2 \leq f_1^{-1/2} m_2^{3/2} - m_2 = 3.3 \, M_\odot. \tag{6.4}$$

We can estimate the pulsar mass if we assume that the angular momentum of the orbit has no preferred direction in space. In that case, $\cos i$ takes on a uniform PDF over $0 \leq \cos i \leq 1$ and consequently the sine of the inclination angle has a probabilistic

median of $\sin i = \sqrt{3}/2$. Inserting that value of $\sin i$ into the mass function along with the median value of m_2 from the $P_b - m_2$ relation gives $m_1 = 2.4 \, \mathrm{M}_\odot$. For comparison, Thorsett & Chakrabarty use the $P_b - m_2$ relation of Rappaport et al. (1995) and orbital parameters from the PSR J2033+1734 discovery paper (Ray *et al.* 1996), together with somewhat different statistics, to deduce the 68% confidence region $0.772 \, \mathrm{M}_\odot \leq m_1 \leq 2.489 \, \mathrm{M}_\odot$ and the median-likelihood value $m_1 = 1.720 \, \mathrm{M}_\odot$. Figure 6.6 shows the values of the pulsar and white dwarf masses allowed by the mass function and the $P_b - m_2$ relation.

6.3   PSR J2322+2057

PSR J2322+2057 is the only MSP examined in this thesis that lacks a companion star. It was discovered at Arecibo (Nice, Taylor, and Fruchter 1993). Nice & Taylor (1995) made the first measurement of its proper motion.

While isolated pulsars predominate in the population of slow pulsars, they comprise a minority of the known MSPs. To give an idea, 1186 (98%) of the 1220 unrecycled pulsars in the $P - \dot{P}$ diagram of Figure 1.1 are solitary, and all of these exist outside of globular clusters. By contrast, only 35 (41%) of the 85 MSPs in the plot are solitary, and of these just 14 exist, like PSR J2322+2027, outside clusters. The high fraction of isolated MSPs within clusters presumably stems from disruptive collisions between binaries and nearby stars (Verbunt *et al.* 1987). It may also result from selection bias, as accelerations within a cluster's gravitational field complicate the detection of the short-period binaries that are expected to form via dynamical interactions (Rasio, Pfahl, and Rappaport 2000; Camilo *et al.* 2000).

MSPs attain their short periods through interactions with binary companions. How does an MSP become isolated? The most popular scenario posits that its high-energy radiation evaporates the secondary (Bhattacharya and van den Heuvel 1991).

This hypothesis was bolstered by the discovery of two eclipsing MSPs, PSR B1957+20 (Fruchter, Stinebring, and Taylor 1988) and PSR B1744-24A (Lyne *et al.* 1990), both apparently in the process of ablating their low-mass secondaries. Other models suggest that isolated MSPs are created through accretion-induced collapse of a white dwarf (Bailyn and Grindlay 1990); through the merger of two white dwarfs (Michel 1987); through a Thorne-Żytkow object, the hypothesized product of the merger of a neutron star and a red giant (Podsiadlowski, Pringle, and Rees 1991); or through tidal dissipation in a binary that strips mass from the pulsar's companion (Radhakrishnan and Shukre 1986). However they are formed, isolated MSPs seem not to differ appreciably from binary MSPs in the distribution of their spin periods or in their pulse morphology. Whether they differ in characteristic age, magnetic field strength, or transverse velocity is harder to ascertain, as these quantities depend on the typically unknown distances to the objects. Bailes *et al.* (1997) find that solitary MSPs have lower radio luminosities than binary MSPs. This could indicate an intrinsic difference in emission properties. Or it could be that isolated MSPs as a class having lower space velocities, so that they keep them nearer to the Galactic plane (i.e., closer to us), making the dim ones easier to detect.

6.3.1   Observations

PSR J2322+2057 has been observed for over 10 years at Arecibo. Table 6.7 summarizes the 102 average TOAs. The Mark III points, gathered at 430 MHz between 1991 December and 1994 July, have already been analyzed by Nice & Taylor (1995). The new Mark IV data was acquired monthly at 430 MHz between 1998 October and 2002 September and at 1410 MHz on the same days between 2000 March and 2002 September.

Table 6.7: Summary of Arecibo Observations of PSR J2322+2057

System	Dates	Frequency (MHz)	Bandwidth (MHz)	Number of TOAs	Typical Integration (min)	RMS Residual[a] (μs)
Mark III	1992.0–1994.6	430	32×0.25	51	45	3.7
Mark IV	1998.8–2002.7	430	5	35	45	2.7
	2000.2–2002.7	1410	10	16	29	4.7

[a]Values incorporate the effect of averaging TOAs from shorter integration times.

6.3.2 Timing Results

Table 6.8 presents the fitted astrometric and spin parameters of PSR J2322+2027. Before we re-weighted the statistical uncertainties in the TOA sets, the goodness-of-fit statistic in the original fit was $\chi^2/\nu = 4.8$, where $\nu = 89$ is the number of degrees of freedom. Derivatives of spin frequency through fourth order were also needed to improve the fit. Figure 6.7 shows the postfit timing residuals.

Our results are in statistical agreement with those of Nice & Taylor (1995). In particular, our measurements of the proper-motion coordinates are 20–40 times more precise then theirs, an improvement to be expected for a sinusoidal delay whose amplitude grows linearly in time. Those authors assumed a range values for the unknown line-of-sight component of the velocity to derive spreads in the radial and tangential components within the Galactic plane and in the component perpendicular to the plane (see their Fig. 2). Our updated proper-motion measurements do not alter that analysis. Unlike those authors, we are able to use our dual-frequency TOAs to measure the time derivative of the DM.

Table 6.8 also lists quantities derived from the fitted parameters. Applying the NE2001 model of Galactic electron density to the DM (Cordes & Lazio 2002; see § 3.4.2), we estimate the distance to the pulsar to be $d = 0.80 \pm 0.10$ kpc. We use

Table 6.8: Astrometric and spin parameters of PSR J2322+2057[a].

Right ascension, α (J2000)	$23^{\mathrm{h}}22^{\mathrm{m}}22\overset{\mathrm{s}}{.}350070(18)$
Declination, δ (J2000)	$+20°57'02\overset{''}{.}8721(5)$
Proper motion in R.A., $\mu_\alpha = \dot{\alpha}\cos\delta$ (mas yr^{-1})	$-18.45(6)$
Proper motion in Dec., $\mu_\delta = \dot{\delta}$ (mas yr^{-1})	$-15.00(12)$
Composite proper motion, μ (mas yr^{-1})	*23.78(9)*
Galactic longitude, l (deg)	*96.5147*
Galactic latitude, b (deg)	*-37.3100*
Position angle of μ in equatorial coordinates, ϕ (deg)	*230.9(2)*
Position angle of μ in Galactic coordinates, ϕ (deg)	*255.2(2)*
Pulse period, P (ms)	$4.8084282112023(7)$
Period derivative (observed), $\dot{P}_{\mathrm{obs}}$ (10^{-21})	$9.650(4)$
Period derivative (intrinsic), $\dot{P}_{\mathrm{int}}$ (10^{-21})	*5.0(7)*
Frequency, ν (Hz)	$207.96816674320(3)$
First derivative of ν, $\dot{\nu}$ ($10^{-16}\,\mathrm{s}^{-2}$)	$-4.1739(15)$
Second derivative of ν, $\ddot{\nu}$ ($10^{-26}\,\mathrm{s}^{-3}$)	$-2.1(7)$
Third derivative of ν, $\dddot{\nu}$ ($10^{-35}\,\mathrm{s}^{-4}$)	$-6(5)$
Fourth derivative of ν, $\nu^{(4)}$ ($10^{-41}\,\mathrm{s}^{-5}$)	$1.0(3)$
Epoch (MJD [TDB])	50574.0
Dispersion measure, DM (pc cm^{-3})	$13.3817(3)^b$
First derivative of DM, $d\mathrm{DM}/dt$ (pc cm^{-3} yr^{-1})	$0.00054(7)$
Distance, d (kpc)	*0.80(10)^c*
Characteristic age, τ (Gyr)	*15(2)*
Surface magnetic field strength, B_0 (G)	*1.62(11) $\times 10^8$*

[a]Figures in parentheses are uncertainties in the last digit quoted, and italicized numbers represent quantities derived from fitted parameters.

[b]The quoted uncertainty is a formal estimate from the parameter fit and probably understates the true uncertainty.

[c]Distance is derived from DM using the NE2001 model of Cordes & Lazio (2002).
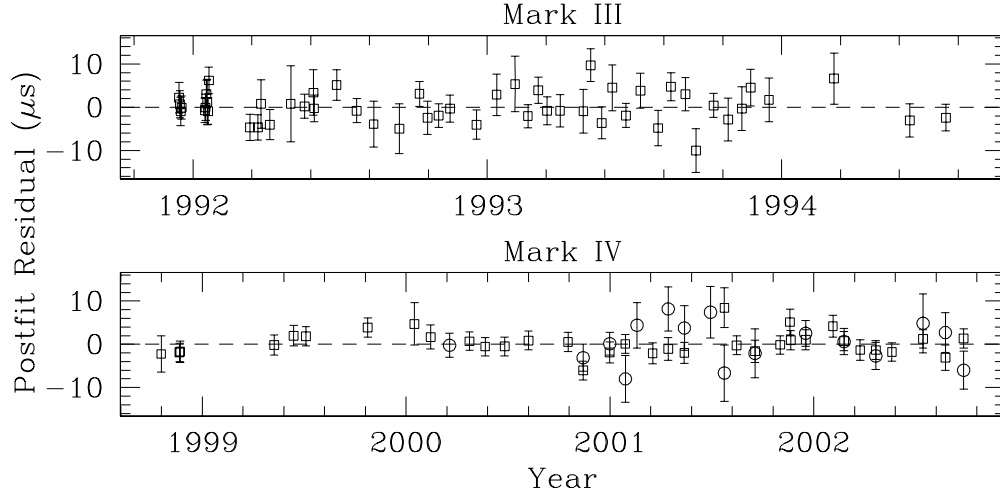
Figure 6.7: Postfit residuals of PSR J2322+2057, divided by data-acquisition system. The four-year gap between data sets is due to a shutdown of the Arecibo observatory. Vertical bars are uncertainties in the TOAs. Squares and circles indicate observing frequencies of 430 and 1410 MHz, respectively.

that value, in turn, to subtract from the observed spin period derivative the biases induced by differential accelerations. We find $\dot{P}_{\text{int}}$ to be a factor of ~ 0.5 smaller than $\dot{P}_{\text{obs}}$, mainly due to proper-motion bias.

Appendix A

Average TOAs

We use the following algorithm to create an average arrival time out of n consecutive TOAs taken at a single observing frequency and using the same receiving system.

1. Run `TEMPO` on the full data set and use the output to calculate the weighted average residual,

$$\bar{r} = \sum_{i=1}^{n} w_i r_i, \tag{A.1}$$

and the standard deviation of the residuals,

$$\sigma_r = \left[\left(\sum_{i=1}^{n} r_i^2 w_i \right) - \bar{r}^2 \right]^{1/2}, \tag{A.2}$$

where the residual $r_i = t_i^{\mathrm{obs}} - t_i^{\mathrm{model}}$ is the difference between the observed and predicted TOA, and its weight, w_i, is given by

$$w_i = \frac{1/\sigma_i^2}{\sum_{j=1}^{n} 1/\sigma_j^2}, \tag{A.3}$$

with σ_i the measurement uncertainty in the arrival time t_i^{obs}.

2. After sorting the arrival times chronologically, find the median TOA, $t_{\mathrm{m}}^{\mathrm{obs}}$, and its residual, $t_{\mathrm{m}}^{\mathrm{obs}}$, by taking $m = \mathrm{int}[(n+1)/2]$. Define the average arrival time, $\bar{t}$, to be

$$\bar{t} = t_{\mathrm{m}}^{\mathrm{obs}} - r_{\mathrm{m}} + \bar{r}. \tag{A.4}$$

3. Assign to $\bar{t}$ an uncertainty of

$$\sigma_{\bar{t}} = \frac{\sigma_r}{\sqrt{n-1}}. \tag{A.5}$$

Consolidating n arrival times into a single TOA with a smaller error bar reduces clutter in a residual plot, giving a clearer picture of underlying trends. A caveat: average TOAs are unsuitable for short-period binaries ($P_b \lesssim 1\,\mathrm{d}$) because they filter out signals with timescales less than the typically hour-long averaging time, losing information about the orbit. To put it another way, the parameter fit of a fast-orbiting pulsar benefits more from a sequence of moderate-uncertainty data points spaced evenly around the orbit than from a single low-uncertainty point that samples only one location on the ellipse.

Appendix B

Statistical Analysis of Binary Masses and Inclination Angle

The PDFs of m_1, m_2, and $\cos i$ can be calculated by least-squares fitting the TOAs to a timing model across a grid of m_2 and $\cos i$ values and analyzing variations in the goodness-of-fit statistic χ^2. The method proceeds as follows.

In the fit at each gridpoint, the PK parameters of the DD model are held fixed at values predicted by GR (eqns. 1.23-1.31) while all other parameters are permitted to vary. To specify the PK terms requires knowing m_1, which is extracted from the Keplerian mass function (eqn. 1.12), given m_2 and $\cos i$. Technically, the mass function changes across the grid, since x and P_b are fit at each point. But these variations are extremely small, and so the mass function can safely be treated as constant. We set it to the value from a fit with all PK parameters held at zero. At each gridpoint we record the value of χ^2.

To find PDFs, we look at how χ^2 differs from its global minimum on the grid, χ_0^2. The global minimum is the point of maximum likelihood; it represents the most probable values of m_2 and $\cos i$. Smaller departures from the minimum signify more

probable configurations of m_2 and $\cos i$ than larger ones. Each value of

$$\Delta\chi^2(m_2, \cos i) = \chi^2(m_2, \cos i) - \chi_0^2 \tag{B.1}$$

has a χ^2 distribution with two degrees of freedom. It therefore maps to a Bayesian likelihood function,

$$p(\{t_j\} \,|\, m_2, \cos i) = \left(\frac{1}{2}\right) e^{-\Delta\chi^2/2}, \tag{B.2}$$

where $\{t_j\}$ stands for the timing data. Accordingly, the joint posterior probability density of m_2 and $\cos i$ is

$$p(m_2, \cos i \,|\, \{t_j\}) = \frac{p(\{t_j\}\,|\, m_2, \cos i)}{p(\{t_j\})} \, p(m_2, \cos i). \tag{B.3}$$

The so-called Bayesian "evidence", $p(\{t_j\})$, is determined by normalizing the integral of $p(m_2, \cos i \,|\{t_j\})$ over all grid points consistent with $m_1 > 0$, given the relationship among m_1, m_2 and $\cos i$ in the mass function. As in all Bayesian investigations, a choice must be made for the prior, $p(m_2, \cos i)$. We select the product of a uniform distribution on $0 \leq m_2 \leq m_{2,\,\mathrm{max}}$ and a uniform distribution on $0 \leq \cos i \leq 1$. For the companion mass, the choice embodies our ignorance about the star. In the binaries examined in this thesis, all that is known for certain is that the companion is a white dwarf, for which reason we set $m_{2,\,\mathrm{max}} = 1.4\,\mathrm{M_\odot}$, the Chandrasekhar limit. For the inclination angle, a flat distribution in $\cos i$ follows from the assumption that the orbital angular momentum vector has no preferred direction in space.

The PDF of m_2 is obtained by marginalizing equation B.3 with respect to $\cos i$:

$$p(m_2|\{t_j\}) = \int_0^1 d(\cos i) \, p(m_2, \cos i \,|\{t_j\}). \tag{B.4}$$

Likewise, marginalization with respect to m_2 gives the PDF of $\cos i$. The PDF of m_1 can be expressed as a double integral,

$$p(m_1 \,|\{t_j\}) = \int_0^{m_{2,\,\mathrm{max}}} dm_2 \int_0^1 d(\cos i) \, p(m_1 \,|m_2, \cos i) \, p(m_2, \cos i \,|\{t_j\}). \tag{B.5}$$

The pulsar mass is guaranteed to agree with the mass function by setting

$$p(m_1|m_2, \cos i) = \delta \left[m_1 - \left(\frac{(m_2 \sin i)^{3/2}}{f_1^{1/2}} - m_2 \right) \right] H(m_1), \qquad \text{(B.6)}$$

where δ is the Dirac function and where the Heaviside function, H, picks out positive values of m_1. Finally, the joint PDF of m_1 and m_2 is obtained by a transformation of variables in equation B.3 from $\cos i$ to m_1,

$$\begin{aligned} p(m_1, m_2|\{t_j\}) &=& p(m_2, \cos i \,|\{t_j\}) \left| \frac{\partial \cos i}{\partial m_1} \right| \\ &\times& \delta \left(\cos i - \left[1 - \frac{f_1^{2/3}(m_1 + m_2)^{4/3}}{m_2^2} \right]^{1/2} \right), \qquad \text{(B.7)} \end{aligned}$$

where the delta function again forces m_1, m_2, and $\cos i$ to comply with the mass function.

Confidence limits can be established by finding a range of parameter space around the maximum-likelihood point that encompasses a specified percentage of the total area under the PDF. For a one-dimensional distribution, the convention we adopt is that the limits of the range span the shortest possible distance. For example, if $\bar{m}_1$ is the maximum likelihood value of the pulsar mass, then we take the upper and lower confidence limits to be the values m_1^{upper} and m_1^{lower} such that $|m_1^{\text{upper}} - m_1^{\text{lower}}|$ is minimized under the constraint that (for 68% confidence)

$$\int_{\bar{m}_1 - m_1^{\text{lower}}}^{\bar{m}_1 + m_1^{\text{upper}}} p(m_1 \,|\{t_j\}) dm_1 = 0.68. \qquad \text{(B.8)}$$

For a two-dimensional PDF, a 68% confidence limit is a closed contour around the maximum-likelihood point with the property that all points along the curve and within it have a probability of 0.68 or higher.

References

Abramovici, A. *et al.* 1992, *Science*, **256**, 325.

Allen, B. 1997, in *Relativistic Gravitation and Gravitational Radiation: Proceedings of the Les Houches School of Physics 26 Sept-6 Oct*, ed. J. A. March and J. P. Lasota, (San Francisco: Cambridge University Press), 373.

Alpar, M. A., Cheng, A. F., Ruderman, M. A., and Shaham, J. 1982, *Nature*, **300**, 728.

Arzoumanian, Z. 1995. PhD thesis, Princeton University.

Arzoumanian, Z. 2003, in *Radio Pulsars, ASP Conf. Ser. 302*, ed. M. Bailes, D. J. Nice, and S. E. Thorsett, (San Francisco: Astronomical Society of the Pacific), 69.

Arzoumanian, Z., Fruchter, A. S., and Taylor, J. H. 1994, *ApJ*, **426**, L85.

Arzoumanian, Z., Nice, D. J., Taylor, J. H., and Thorsett, S. E. 1994, *ApJ*, **422**, 671.

Baade, W. and Zwicky, F. 1934, *Proc. Nat. Acad. Sci.*, **20**, 254.

Backer, D. C. 1989, in *Timing Neutron Stars, (NATO ASI Series)*, ed. H. Ögelman and E. P. J. van den Heuvel, (Dordrecht: Kluwer), 3.

Backer, D. C., Hama, S., Van Hook, S., and Foster, R. S. 1993, *ApJ*, **404**, 636.

Backer, D. C., Kulkarni, S. R., Heiles, C., Davis, M. M., and Goss, W. M. 1982, *Nature*, **300**, 615.

Backer, D. C. and Sallmen, S. 1997, *Astron. J.*, **114**, 1539.

Backer, D. C., Wong, T., and Valanju, J. 2000, *ApJ*, **543**, 740.

Bailes, M. *et al.* 1997, *ApJ*, **481**, 386.

Bailes, M., Ord, S. M., Knight, H. S., and Hotan, A. W. 2003, *ApJ*, **595**, L49.

Bailyn, C. D. and Grindlay, J. E. 1990, *ApJ*, **353**, 159.

Becker, W., Trumper, P., Lundgren, S., Cordes, J., and Zepka, A. 1996, *MNRAS*, **282**, L36.

Bertotti, B., Iess, L., and Tortora, P. 2003, *Nature*, **425**, 374.

Bhattacharya, D. and van den Heuvel, E. P. J. 1991, *Phys. Rep.*, **203**, 1.

Blandford, R. D., Narayan, R., and Romani, R. W. 1984, *J. Astrophys. Astr.*, **5**, 369.

Brans, C. and Dicke, R. H. 1961, *Phys. Rev.*, **124**, 925.

Brisken, W. F., Benson, J. M., Goss, W. M., and Thorsett, S. E. 2002, *ApJ*, **571**, 906.

Caldwell, R. R., Dave, R., and Steinhardt, P. J. 1998, *Ap&SS*, **261**, 303 .

Callanan, P. J., Garnavich, P. M., and Koester, D. 1998, *MNRAS*, **298**, 207.

Camilo, F., Foster, R. S., and Wolszczan, A. 1994, *ApJ*, **437**, L39.

Camilo, F., Lorimer, D. R., Freire, P., Lyne, A. G., and Manchester, R. N. 2000, *ApJ*, **535**, 975.

Camilo, F. *et al.* 2001, *ApJ*, **548**, L187.

Camilo, F., Nice, D. J., Shrauner, J. A., and Taylor, J. H. 1996, *ApJ*, **469**, 819.

Camilo, F., Nice, D. J., and Taylor, J. H. 1996, *ApJ*, **461**, 812.

Camilo, F., Thorsett, S. E., and Kulkarni, S. R. 1994, *ApJ*, **421**, L15.

Cognard, I. and Lestrade, J. F. 2000, *A&A*, **323**, 211.

Cordes, J. M. and Chernoff, D. F. 1997, *ApJ*, **482**, 971.

Cordes, J. M. and Downs, G. S. 1985, *ApJS*, **59**, 343.

Cordes, J. M. and Greenstein, G. 1981, *ApJ*, **245**, 1060.

Cordes, J. M. and Lazio, T. J. W. 2002, http://xxx.lanl.gov/abs/astro-ph/0207310.

Cordes, J. M., Wolszczan, A., Dewey, R. J., Blaskiewicz, M., and Stinebring, D. R. 1990, *ApJ*, **349**, 245.

Damour, T. and Deruelle, N. 1986, *Ann. Inst. H. Poincaré (Physique Théorique)*, **44**, 263.

Damour, T. and Esposito-Farèse, G. 1996, *Phys. Rev. D*, **54**, 1474.

Damour, T., Gibbons, G. W., and Taylor, J. H. 1988, *Phys. Rev. Lett.*, **61**, 1151.

Damour, T. and Taylor, J. H. 1991, *ApJ*, **366**, 501.

Damour, T. and Taylor, J. H. 1992, *Phys. Rev. D*, **45**, 1840.

Detweiler, S. 1979, *ApJ*, **234**, 1100.

Dewey, R. J. and Cordes, J. M. 1987, *ApJ*, **321**, 780.

Dodson, P. M., McCulloch, P. M., and Lewis, D. R. 2002, *ApJ*, **564**, L85.

Edwards, R. T. and Bailes, M. 2001a, *ApJ*, **547**, L37.

Edwards, R. T. and Bailes, M. 2001b, *ApJ*, **553**, 801.

Ergma, E., Lundgren, S. C., and Cordes, J. M. 1977, *ApJ*, **475**, L29.

Ergma, E., Sarna, M. J., and Gerskevits-Antipova, J. 2001, *MNRAS*, **321**, 71.

Fierz, M. 1956, *Helv. Phys. Acta*, **29**, 128.

Foster, R. S. and Backer, D. C. 1990, *ApJ*, **361**, 300.

Foster, R. S. and Cordes, J. M. 1990, *ApJ*, **364**, 123.

Foster, R. S., Wolszczan, A., and Camilo, F. 1993, *ApJ*, **410**, L91.

Fruchter, A. S. *et al.* 1990, *ApJ*, **351**, 642.

Fruchter, A. S., Stinebring, D. R., and Taylor, J. H. 1988, *Nature*, **333**, 237.

Gérard, J.-M. and Wiaux, Y. 2002, *Phys. Rev. D*, **66**, 4040.

Gold, T. 1969, *Nature*, **221**, 25.

Goldman, I. 1990, *MNRAS*, **244**, 184.

Goldman, I. 1992, *ApJ*, **390**, 494.

Goldreich, P. and Julian, W. H. 1969, *ApJ*, **157**, 869.

Gott, J. R., Gunn, J. E., and Ostriker, J. P. 1970, *ApJ*, **160**, L91.

Groth, E. J. 1975, *ApJS*, **29**, 443.

Hankins, T. H. and Rickett, B. J. 1975, in *Methods in Computational Physics Volume 14 — Radio Astronomy*, (New York: Academic Press), 55.

Hansen, B. and Phinney, E. S. 1997, *MNRAS*, **291**, 569.

Hansen, B. M. S. and Phinney, E. S. 1998, *MNRAS*, **294**, 569.

Hellings, R. W., Adams, P. J., Anderson, J. D., Keesey, M. S., Lau, E. L., Standish, E. M., Canuto, V. M., and Goldman, I. 1983, *Phys. Rev. Lett.*, **51**, 1609.

Hellings, R. W. and Downs, G. S. 1983, *ApJ*, **265**, L39.

Hewish, A., Bell, S. J., Pilkington, J. D. H., Scott, P. F., and Collins, R. A. 1968, *Nature*, **217**, 709.

Hulse, R. A. and Taylor, J. H. 1975, *ApJ*, **195**, L51.

Issautier, K., Hoang, S., Moncuquet, M., and Meyer-Vernet, N. 2001, *Space Sci. Rev.*, **97**, 105.

ed. S. Johnston, M. A. Walker, and M. Bailes 1996. *Pulsars: Problems and Progress, IAU Colloquium 160*, San Francisco. Astronomical Society of the Pacific.

Jordan, P. 1959, *Z. Phys.*, **157**, 112.

Kaspi, V. M., Taylor, J. H., and Ryba, M. 1994, *ApJ*, **428**, 713.

Kerr, F. J. and Lynden-Bell, D. 1986, *MNRAS*, **221**, 1023.

Kopeikin, S. M. 1995, *ApJ*, **439**, L5.

Kopeikin, S. M. 1996, *ApJ*, **467**, L93.

Kramer, M., Lange, C., Lorimer, D. R., Backer, D. C., Xilouris, K. M., Jessner, A., and Wielebinski, R. 1999a, *ApJ*, **526**, 957.

Kramer, M., Xilouris, K. M., Camilo, F., Nice, D., Lange, C., Backer, D. C., and Doroshenko, O. 1999b, *ApJ*, **520**, 324.

Kramer, M., Xilouris, K. M., Lorimer, D. R., Doroshenko, O., Jessner, A., Wielebinski, R., Wolszczan, A., and Camilo, F. 1998, *ApJ*, **501**, 270.

Kuijken, K. and Gilmore, G. 1989, *MNRAS*, **239**, 571.

Lange, C., Camilo, F., Wex, N., Kramer, M., Backer, D., Lyne, A., and Doroshenko, O. 2001, *MNRAS*, **326**, 274.

Lipunov, V. M., Postnov, K. A., Prokhorov, M. E., and Osminkin, E. Y. 1994, *ApJ*, **423**, L121.

Lommen, A. N. and Backer, D. C. 2001, *ApJ*, **562**, 297.

Lorimer, D. R., Festin, L., Lyne, A. G., and Nicastro, L. 1995, *Nature*, **376**, 393.

Lundgren, S. C., Cordes, J. M., Foster, R. S., Wolszczan, A., and Camilo, F. 1996, *ApJ*, **458**, L33.

Lundgren, S. C., Foster, R. S., and Camilo, F. 1996, in *IAU Colloq. 160, Pulsars: Problems and Progress*, ed. S. Johnston, M. A. Walker, and M. Bailes, (San Francisco: Astronomical Society of the Pacific), 497.

Lundgren, S. C., Foster, R. S., and Camilo, F. 1996, In Johnston *et al.* (Johnston, Walker, and Bailes 1996), 497.

Lundgren, S. C., Zepka, A. F., and Cordes, J. M. 1995, *ApJ*, **453**, 419.

Lyne, A. G. and Lorimer, D. R. 1994, *Nature*, **369**, 127.

Lyne, A. G. *et al.* 1990, *Nature*, **347**, 650.

Lyne, A. G. *et al.* 1998, *MNRAS*, **295**, 743.

Manchester, R. N. and Taylor, J. H. 1977, *Pulsars*, (San Francisco: Freeman).

Matsakis, D. N. and Foster, R. S. 1996, in *Amazing Light: A Volume Dedicated to Charles Hard Townes on His 80th Birthday*, ed. R. Y. Chiao, (New York: Springer), 445.

Matsakis, D. N., Taylor, J. H., and Eubanks, T. M. 1997, *A&A*, **326**, 924.

Michel, F. C. 1987, *Nature*, **329**, 310.

Nice, D. J., Splaver, E. M., and Stairs, I. H. 2001, *ApJ*, **549**, 516.

Nice, D. J. and Taylor, J. H. 1995, *ApJ*, **441**, 429.

Nice, D. J., Taylor, J. H., and Fruchter, A. S. 1993, *ApJ*, **402**, L49.

Nice, D. J. and Thorsett, S. E. 1992, *ApJ*, **397**, 249.

Nice, D. J. and Thorsett, S. E. 1996, In Johnston *et al.* (Johnston, Walker, and Bailes 1996), 523.

Nordtvedt, K. 1990, *Phys. Rev. Lett.*, **65**, 953.

Peters, P. C. 1964, *Phys. Rev.*, **136**, 1224.

Phillips, J. A. and Wolszczan, A. 1992, *ApJ*, **385**, 273.

Phinney, E. S. and Kulkarni, S. R. 1994, *ARAA*, **32**, 591.

Podsiadlowski, P., Pringle, J. E., and Rees, M. J. 1991, *Nature*, **352**, 783.

Portegies Zwart, S. F. and Yungelson, L. R. 1998, *A&A*, **332**, 173.

Radhakrishnan, V. and Shukre, C. S. 1986, *Ap&SS*, **118**, 329.

Rappaport, S., Podsiadlowski, P., Joss, P. C., DiStefano, R., and Han, Z. 1995, *MNRAS*, **273**, 731.

Rasio, F. A., Pfahl, E. D., and Rappaport, S. 2000, *ApJ*, **532**, L47.

Rawley, L. A. 1986. PhD thesis, Princeton University.

Rawley, L. A., Taylor, J. H., and Davis, M. M. 1988, *ApJ*, **326**, 947.

Ray, P. S., Thorsett, S. E., Jenet, F. A., van Kerkwijk, M. H., Kulkarni, S. R., Prince, T. A., Sandhu, J. S., and Nice, D. J. 1996, *ApJ*, **470**, 1103.

Reasenberg, R. D. 1983, *Philos. Trans. Roy. Soc. London A*, **310**, 227.

Reasenberg, R. D. *et al.* 1979, *ApJ*, **234**, L219.

Reid, M. J. 1989, in *The Center of the Galaxy, IAU Symposium 136*, ed. M. Morris, (Dordrecht: Kluwer), 37.

Rickett, B. J. 1990, *ARAA*, **28**, 561.

Romani, R. W. 1989, in *Timing Neutron Stars*, ed. H. Ögelman and E. P. J. van den Heuvel, (Dordrecht: Kluwer), 113.

Ryba, M. F. 1991. PhD thesis, Princeton University.

Ryba, M. F. and Taylor, J. H. 1991, *ApJ*, **371**, 739.

Sazhin, M. V. 1978, *Sov. Astron.*, **22**, 36.

Scarrott, S. M., Rolph, C. D., and Tadhunter, C. N. 1990, *MNRAS*, **243**, 5P.

Schoenberner, B., Driebe, T., and Blocker, T. 2000, *A&A*, **356**, 929.

Seidelmann, P. K., Guinot, B., and Doggett, L. E. 1992, in *Explanatory Supplement to the Astronomical Almanac*, ed. P. K. Seidelmann, (Mill Valley, California: University Science Books), 39.

Shklovskii, I. S. 1970, *Sov. Astron.*, **13**, 562.

Smarr, L. L. and Blandford, R. 1976, *ApJ*, **207**, 574.

Spergel, D. N. *et al.* 2003, *ApJ*, **148**, 175.

Splaver, E. M., Nice, D. J., Arzoumanian, Z., Camilo, F., Lyne, A. G., and Stairs, I. H. 2002, *ApJ*, **581**, 509.

Stairs, I. H., Splaver, E. M., Thorsett, S. E., Nice, D. J., and Taylor, J. H. 2000,

MNRAS, **314**, 459. (astro-ph/9912272).

Stairs, I. H., Thorsett, S. E., Taylor, J. H., and Wolszczan, A. 2002, *ApJ*, **581**, 501.

Standish, E. M. 1990, *A&A*, **233**, 252.

Stella, L., Priedhorsky, W., and White, N. E. 1987, *ApJ*, **312**, L17.

Stinebring, D. R., Kaspi, V. M., Nice, D. J., Ryba, M. F., Taylor, J. H., Thorsett, S. E., and Hankins, T. H. 1992, *Rev. Sci. Instrum.*, **63**, 3551.

Sturrock, P. A. 1971, *ApJ*, **164**, 529.

Taam, R. E., King, A. R., and Ritter, H. 2000, *ApJ*, **541**, 329.

Taam, R. E. and van den Heuvel, E. P. J. 1986, *ApJ*, **305**, 235.

Tauris, T. M. and Bailes, M. 1996, *A&A*, **315**.

Tauris, T. M. and Savonije, G. J. 1999, *A&A*, **350**, 928.

Tauris, T. M., van den Heuvel, E. P. J., and Savonije, G. J. 2000, *ApJ*, **530**, L93.

Taylor, J. H. 1991, *Proc. I. E. E. E.*, **79**, 1054.

Taylor, J. H. 1992, *Philos. Trans. Roy. Soc. London A*, **341**, 117.

Taylor, J. H. and Cordes, J. M. 1993, *ApJ*, **411**, 674.

Taylor, J. H. and Weisberg, J. M. 1989, *ApJ*, **345**, 434.

Thorsett, S. E. 1996, *Phys. Rev. Lett.*, **77**, 1432.

Thorsett, S. E. and Chakrabarty, D. 1999, *ApJ*, **512**, 288.

Thorsett, S. E. and Dewey, R. J. 1996, *Phys. Rev. D*, **53**, 3468.

Tonry, J. L. *et al.* 2003, *ApJ*, **594**, 1.

Torres, D. F. 2002, *Phys. Rev. D*, **66**, 3522.

Toscano, M., Britton, M. C., Manchester, R. N., Bailes, M., Sandhu, J. S., Kulkarni, S. R., and Anderson, S. B. 1999a, *ApJ*, **523**, L171.

Toscano, M., Sandhu, J. S., Bailes, M., Manchester, R. N., Britton, M. C., Kulkarni, S. R., Anderson, S. B., and Stappers, B. W. 1999b, *MNRAS*, **307**, 925.

van den Heuvel, E. P. J. 1994, *A&A*, **291**, L39.

van den Heuvel, E. P. J. and Bitzaraki, O. 1995, *A&A*, **297**, L41.

van Kerkwijk, M. and Kulkarni, S. R. 1999, *ApJ*, **516**, L25.

van Kerkwijk, M. H., Bell, J. F., Kaspi, V. M., and Kulkarni, S. R. 2000, *ApJ*, **530**, L37.

van Straten, W., Bailes, M., Britton, M., Kulkarni, S. R., Anderson, S. B., Manchester, R. N., and Sarkissian, J. 2001, *Nature*, **412**, 158.

Verbunt, F., van den Heuvel, E. P. J., van Paradijs, J., and Rappaport, S. A. 1987, *Nature*, **329**, 312.

Weinberg, S. 1972, *Gravitation and Cosmology: Principles and Applications of the General Theory of Relativity*, (New York: Wiley).

Weisberg, J. M. and Taylor, J. H. 2002, *ApJ*, **576**, 942.

Wex, N. 1998, *MNRAS*, **298**, 997.

Will, C. M. 1993, *Theory and Experiment in Gravitational Physics*, (Cambridge: Cambridge University Press).

Will, C. M. 2001, *Living Reviews in Relativity*. http://www.livingreviews.org/Articles/lrr-2001-4/.

Will, C. M. and Zaglauer, H. W. 1989, *ApJ*, **346**, 366.

Williams, J. G., Newhall, X. X., and Dickey, J. O. 1996, *Phys. Rev. D*, **53**, 6730.